Modelling of Solar Mesogranulation

Dissertation
zur Erlangung des Doktorgrades
der Mathematisch-Naturwissenschaftlichen Fakultäten
der Georg-August-Universität zu Göttingen

vorgelegt von
Łukasz Maciej Matloch
aus Olsztyn/Poland

Göttingen 2008

D7

Referent: Prof. Dr. Franz Kneer

Korreferent: Prof. Dr. Manfred Schüssler

Tag der mündlichen Prüfung:

Contents

Summary

Mesogranulation is a cellular pattern of horizontal flow on the solar surface, intermediate in scale between granulation, the dominant convective flow pattern (typical size ~ 1 Mm), and supergranulation (typical size ~ 30 Mm). The physical origin of mesogranulation is not well understood. This thesis presents the investigation of the origin of mesogranulation as a self-arrangement of granules. We show that granulation can be described as a cellular automaton and present one- and two-dimensional models of the granulation pattern. The models do not aim at a perfect reproduction of the granulation structure, but rather focus on capturing the local interaction between the granules that leads to the self-arrangement phenomenon.

- In the one-dimensional model (Chapter 2) the granules are defined as the spaces between interface points representing the intergranular downflow lanes. Those points move in space (along a line) according to a size-pressure relation (large granules tend to spread, small to shrink), motivated by the observed properties of solar granulation. The results are compared with a random-motion scheme for the intergranular lanes. This is done to study which granule interaction rules lead to a better approximation of the phenomenon. When two interface points get close enough to each other, they merge, marking the disappearance of a granule. New granules appear by the splitting of a parent granule i.e., new intergranular lane appears within the granule.

- In the two-dimensional model (Chapter 3), the granules are represented by triangular areas. The time evolution is spawned by the motion of the triangles' vertices. Like in the one-dimensional case, two motion schemes are applied: the size-pressure relation and the random walk. Additionally, four different rules for the granule splitting are applied to check the robustness of the result.

- We find that our simple cell models are able to simulate the granulation quite well, producing granule size and lifetime distributions similar to those obtained from observations and hydrodynamical simulations. The local interaction rules produce granules that appear, disappear and translate on the surface much like the real granules do.

- Mesogranules are observationally defined as areas of horizontal velocity divergence. In the two-dimensional model, we apply a Local Correlation Tracking (LCT) algorithm to determine the horizontal translation velocities of the granules in the same way as done in simulations and observations. The velocity divergence areas can also be detected through patterns formed by "corks", passive pseudo-particles

advected by the flow, which tend to outline the boundaries of mesogranules. Hence, another definition of mesogranulation in the models is based on the age of the intergranular lanes: intergranular lanes that live longer than a given threshold time are stipulated to accumulate enough corks to outline mesogranules. We find mesogranular structures present in both the one- and two-dimensional models, regardless of the granule interaction and splitting rules, which shows that mesogranulation is a very robust feature of such cell-systems. The mesogranular scale in the models is not forced externally, it evolves from the granular interaction. This scale is not intrinsic however, it depends on the definition and analysis parameters. A given definition and parameters select mesogranular size and lifetime scale from a continuum of scales.

- We compare the two-dimensional LCT results with those obtained in the same way from a realistic three-dimensional hydrodynamical simulation (Chapter 4 and 5) and find a very good agreement. This strongly reinforces the assumption that mesogranulation is not an intrinsic property of the system in the sense that it represents a persistent flow pattern with a fixed scale, but rather is a self-arrangement effect of the locally interacting granules, with its scale depending in the analysis parameters.

1 Introduction

1.1 Solar surface patterns

Of all the celestial bodies in our solar system, the Sun has always been the most fascinating one for humanity, and as the source of virtually all energy accessible on Earth, it is by far the most important one. Initially an object of religious worship, the Sun's evolutions on the sky were watched and variously interpreted, according to the custom of the times. With time and development of modern science we have come to know our star a little better; both ground and space based observations providing a multitude of data for stimulating and testing of theories and ideas. With increasing resolution and quality of observations it has been possible to distinguish between many different features and phenomena that can be seen on the Sun, with different wavelengths allowing insight into different depths of the solar atmosphere and helioseismology providing information about the structure of the solar interior. The complexity of the global interaction of plasma, radiation and the magnetic field still eludes our understanding, leaving many questions open. The key examples are the details of the internal structure of the Sun, operation of the solar dynamo, that is the generation and evolution of the solar magnetic field, the exact abundance of various elements, and the coronal heating processes. Nevertheless, many aspects of solar physics have been understood.

Various physical processes manifest themselves in the surface patterns they create, which can be recognized in the intensity images, the plasma velocity field, or the magnetic field distribution. There exists a multitude of length- and timescales on which these processes take place. The first surface structures detected were the sunspots, the largest of which can be seen with the naked eye as dark patches on the Sun. The sunspots are of magnetic origin and are the largest of the magnetic features on the solar surface; they are up to tens of megameters in size and persist for days to months. Smaller magnetic patterns include pores and faculae. The magnetic features usually appear in the active regions, which are surface areas of enhanced magnetic activity resulting from magnetic flux emergence.

The best known non-magnetic feature on the solar surface is the granulation (Fig. 1.1). It can be recognized both in the continuum intensity images and in the plasma velocity field. The granulation is the most prominent and best understood of the non-magnetic patterns, it has been very well reproduced in the hydrodynamical numerical simulations (Spruit et al. 1990, Stein & Nordlund 1998). The granular flow is driven by surface radiative cooling of the plasma, which maintains a superadiabatic temperature gradient at the top of the convective zone and causes the vertical overturn of material, hence transporting the energy towards the surface. In the convection zone, the plasma is optically thick,

meaning that the mean photon free path is much smaller than the local pressure scale height. This changes upon reaching the surface, where the plasma density decreases and
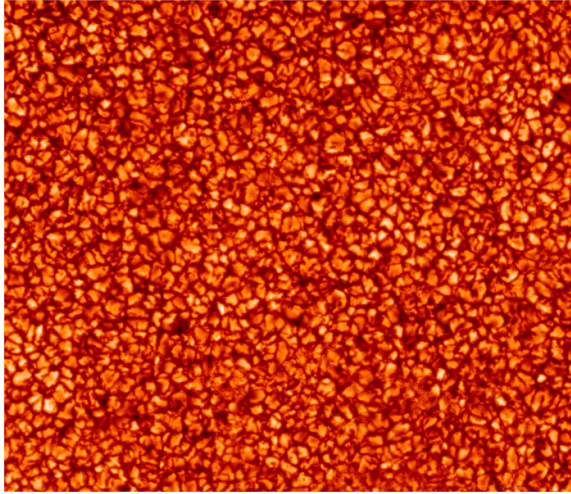

Figure 1.1: The granulation pattern on the solar surface. The dark colder downflows surround hotter bright upflow regions. Image taken with the Swedish Vacuum Solar Telescope, La Palma.

the photons are free to escape through the solar atmosphere into space, effectively cooling the surface. The cold material is denser than the hot plasma underneath and begins to sink back into the interior, forming downflow plumes. These downflows outline the cells and surround the upflow areas. When the upflowing plasma in the cell center reaches the surface, it outflows horizontally while cooling down, eventually reaching and feeding the downflow plumes. Owing to the compressibility of the plasma, the ascending material expands while the descending plasma is compressed. For such system to be stationary the mass flux must be conserved, hence the narrow downflows are characterized by larger plasma velocities (roughly twice the upflow velocities). Therefore, the faster and more compact downflow plumes are able to penetrate down through the upflowing material and rearrange the existing cell pattern, effectively driving the granulation (Stein & Nordlund 1998).

A prominent example of the leading role of downflow plumes are the so-called exploding granules. These granules expand during their lifetime and eventually develop a new downflow in the center, which breaks up the cell and rearranges the local flow configuration (Rösch 1960, Hirzberger et al. 1999). The mechanism for this is the following: there exists a critical granule cell size of ~1 Mm (Hirzberger et al. 1997, 1999), and when the cell exceeds that size, the upflow in the cell center diminishes. This is caused by a pressure buildup at the top of the cell, which is proportional to the granule size and

which deflects the upflowing plasma horizontally. Such pressure also works to inhibit the upward plasma motion, and when the granule exceeds the critical size, the accompanying pressure buildup is large enough to locally stop the plasma upflow. Without the upflow from below, the plasma at the top of the cell cools radiatively until it is dense enough to sink back into the interior, forming a new downflow plume and breaking up the granule. This process is called "buoyancy braking" (Hurlburt & Toomre 1982). It is quite common that the offspring granules created by the fragmentation also grow to the critical diameter of ~1 Mm and become fragmenters themselves, forming the so-called Trees of Fragmenting Granules (TFGs). Such TFG structures can have lifetime of many hours (Roudier et al. 2003, Roudier & Muller 2004). A somewhat different interpretation of the granulation cell pattern evolution in terms of the downflow plumes have been suggested by Rast (2003): numerical simulations suggest that a downflowing plume initiates time-limited upflows confined to the plume's near surroundings, the amplitude and range of the response flow depending mainly on the dimensionality of the plumes (2D lanes and 3D vertices) and less on their detailed internal structure. A spatial arrangement of these downflows on the solar surface leads to the formation of the granulation cell pattern, with the upflow in the cell center being the sum of all the contributions from the response flows initiated by the dowflows surrounding the granule. The critical granule cell size can then be explained as the maximum cell size that given downflows can sustain. When the granule expands, the downflows are pushed apart and hence the response upflow in the cell center diminishes below that needed to sustain the circulation.

Another distinctive granule type are the so-called dissolvers, that is the cells whose size does not exceed the critical one or vary much over the cell's lifetime. The dissolvers do not undergo the fragmentation process and disappear by being squeezed out of existence by the neighboring cells when the upflow in their center diminishes. There exist other granule types distinguished by the way they appear or disappear, like merging granules or granules that grow out of a point in an intergranular lane, but the fragmenters and dissolvers constitute the majority of cells, and the granule fragmentation mechanism is the primary source of new granules (Müller et al. 2001, Hirzberger et al. 1999). The average granulation cell diameter is ~1 Mm, the average granule lifetime is ~10 minutes (with the fragmenters being statistically larger and longer-lived than dissolvers) and the typical granular upflow velocities are of the order of 1 km/s (Title et al. 1989, Hirzberger et al. 1997, 1999, Müller et al. 2001). Even though it is possible to describe granulation in terms of different granule types and their mutual interactions, one should keep in mind that due to the low viscosity the plasma flow is in general quite turbulent, making granulation a very dynamical phenomenon.

The largest of the cell patterns on the Sun (if one neglects the giant cells, whose existence is controversial) is the supergranulation, known since the 1960s (Fig. 1.2). The supergranular cell size is ~30 Mm, with lifetimes of the order of one day. The first indication of the existence of the supergranular flow scale came from Hart (1956), who found a velocity pattern fluctuating across the solar surface while measuring the solar rotation. Later Leighton et al. (1962) were able to show that the supergranular flow is predominantly horizontal using Doppler effect measurements. The horizontal flow velocities range from 300 m/s to 500 m/s, exceeding the vertical velocities of about 100 m/s. The cell-like structure of the supergranular flow is quite similar to granulation, with upflows in the cell center surrounded by downflow regions. The pattern is conveniently seen in
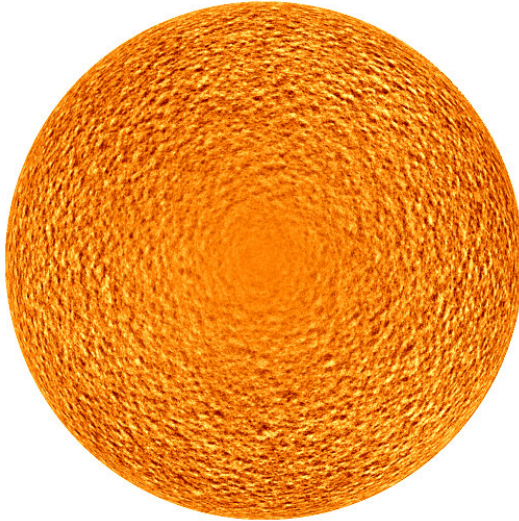
Figure 1.2: A Doppler-image of the supergranulation pattern on the solar disc. The flow is predominantly horizontal, hence at the disc center the signal is very weak. Image credit: SOHO/MDI

the chromospheric emission lines (so-called "chromospheric network") due to magnetic field concentration at the supergranule boundaries. Numerical simulations indicate that deeper in the convection zone the downflows aggregate into separated plumes, which can extend several megameters into the solar interior. Such large downflows are distributed along supergranular cell boundaries (Deubner 1971, Skumanich et al. 1975, Hathaway et al. 2002) and often coincide with "vertices", i.e. places where a few supergranules meet (Frazier 1970). In general, supergranulation is interpreted as convective flow (Simon & Weiss 1968, Vickers 1971, Bogart et al. 1980, Gierasch 1985), with the second ionization of He at depth around 20 Mm proposed as the driving agent. Nevertheless, the complex structure and properties of supergranules have invited many alternative interpretations. For example, significant horizontal flow structures exist within the supergranule cell interiors (mesogranules), the thermal signature of the flow is very weak, and the pattern seems to be "super-rotating" i.e., rotating faster than the surface plasma and the magnetic network (Duvall 1980, Snodgrass & Ulrich 1990, Gizon et al. 2003). Hence, supergranulation was suggested to result from gravity wave modulation of a convective flow (Lindzen & Tung 1976), a transition with depth of the magnetic field filling factor (Foukal 1977), granular pumping of the solar rip-tide (Cloutman 1979), r-mode-convection coupling (Wolff 1995), spatial correlation between exploding granules (Rieutord et al. 2000), the superposition of travelling waves (Gizon et al. 2003), and advection and merger of downflow plumes resulting in a statistical spatial distribution of large downflows (Rast

2003). Recently, Stein et al. (2006) presented results from the numerical simulations of supergranulation, which indicate that the size of the upflows increases continuously with depth as a result of mass conservation. These deep large upflows expand with height, influencing and rearranging the downflowing plumes coming from above, and resulting in a weak supergranular scale flow at the surface. The authors conclude that the morphology from granules to supergranules and giant cells is self-similar, and that granules are the only distinct scale of motion, although there is a small increase in the velocity spectral amplitude at supergranular scales.

Mesogranulation is another cell pattern on the solar surface indicated by observations (Fig. 1.3). The reported cell sizes of mesogranulation vary from 2 to 10 Mm, with lifetime estimates from 30 minutes to a few hours. The inferred horizontal velocities are of the order of 500 m/s, reaching up to 1 km/s, thus exceeding the vertical velocities of about 150 m/s. Detection methods of mesogranules are based on analyzing the plasma velocity field, and, since granular velocities are an order of magnitude larger than the meso- and supergranular ones, it is necessary to average over granulation in order to detect larger-scale patterns. In the first report of the mesogranulation by November et al. (1981), the temporal averaging window was 60 minutes and the measured quantity was the vertical plasma velocity field. The authors found a cell-like pattern of upflow and downflow areas and estimated the cell size to be approximately 7 Mm. The similarities to granulation led to the suggestion that mesocells are also convective in origin, and the first ionization of He at around 7 Mm depth was proposed as the driving force (November et al. 1981). Nevertheless, the weak buoyancy enhancement caused by the He I ionization casts doubt upon this explanation (Rast 1991, Rast & Toomre 1993). Furthermore, in contrast to granulation, the reported mesogranular characteristics vary strongly with the averaging time and other details of the analysis methods applied (Rieutord et al. 2000). Additionally, the existence of a distinctive mesogranular peak in the power spectrum of the horizontal velocity field remains controversial: while some researchers report such a peak (Deubner 1988, Ginet et al. 1992, Lawrence et al. 2001), others report a monotonic spectrum of granular sizes which extends into the reported meso-domain (Wang 1989, Chou et al. 1991, Strauss et al. 1992, Strauss & Bonaccini 1997, Rieutord et al. 2000, Georgobiani et al. 2007).

A convenient quantity for mesogranulation detection and analysis is the horizontal velocity divergence, namely

$$\overrightarrow{\nabla} \cdot \overrightarrow{V_h} \equiv \frac{\partial V_x}{\partial x} + \frac{\partial V_y}{\partial y} \tag{1.1}$$

where $\overrightarrow{V_h}$ is the horizontal velocity field at the solar surface. $\overrightarrow{\nabla} \cdot \overrightarrow{V_h}$ is a scalar field, and the mesogranules are defined as patches of positive divergence, that is horizontal plasma outflow. Figure 1.4 shows an example of the divergence of a 60-minute average of the horizontal velocity field and the corresponding mesogranular patches (horizontal outflows, bright areas), obtained from a three-dimensional hydrodynamic simulation (MU-RaM code, Vögler et al. 2005). A way to visualize larger-scale velocity patterns without explicit time-averaging the data is to track positions of test particles advected horizontally with the flow (so-called "corks"). Cork positions, after evolving for some time τ from their initial configuration, outline areas of velocity divergence averaged over time τ. In the solar convection zone the magnetic Reynolds number is large, ranging from 10^{11} at
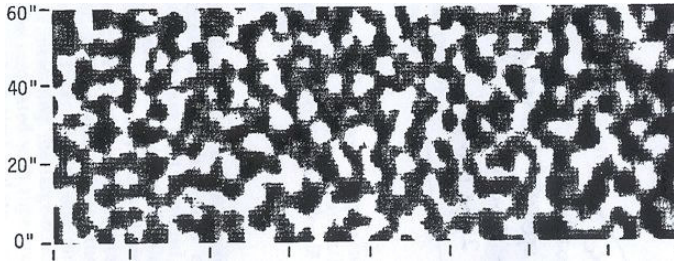
Figure 1.3: The original mesogranulation detection result of November (1981). Black and white areas correspond to upflows and downflows, respectively. The scale on the x and y axes is the same.
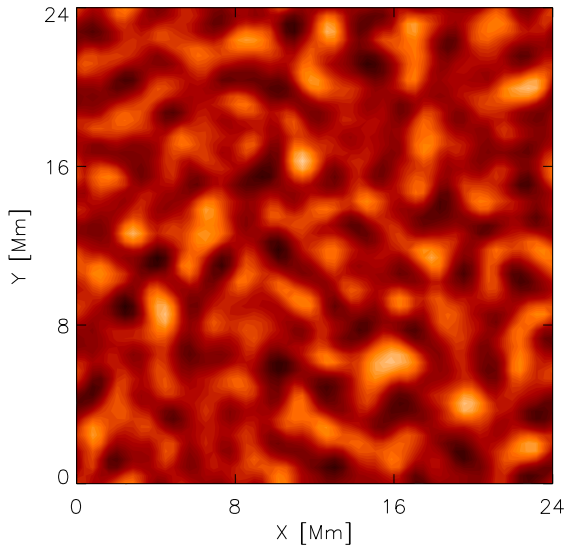

Figure 1.4: Divergence of the 60-minute average of the horizontal velocity obtained from a hydrodynamical simulation (MURaM code). Bright areas correspond to positive divergence (mesogranules).

the bottom to 10^5 near the surface. This means that the timescale of the Ohmic dissipation of the magnetic field is much longer than the advective processes timescale and the mag-

netic field lines are effectively "frozen" into the plasma. The small-scale magnetic flux of both polarities, vertical at the surface due to magnetic buoyancy, is therefore advected into the velocity convergence regions and can serve as corks. Indeed, magnetic flux concentrations can be found in the intergranular network (Lin & Rimmele 1999, Khomenko et al. 2003) and they are known to outline supergranules (Simon & Leighton 1964). More recently, magnetic flux concentrations have also been reported to outline mesogranules (Domínguez Cerdeña 2003, de Wijn et al. 2005). Figure. 1.5 shows an example of the divergence of a 60-minute-averaged horizontal velocity field (hydrodynamic simulation, MURaM code) with corks marked in white after evolving for 60 minutes from an uniform dense distribution. The corks tend to gather in the convergence areas (dark) and outline the patches of positive velocity divergence (bright).
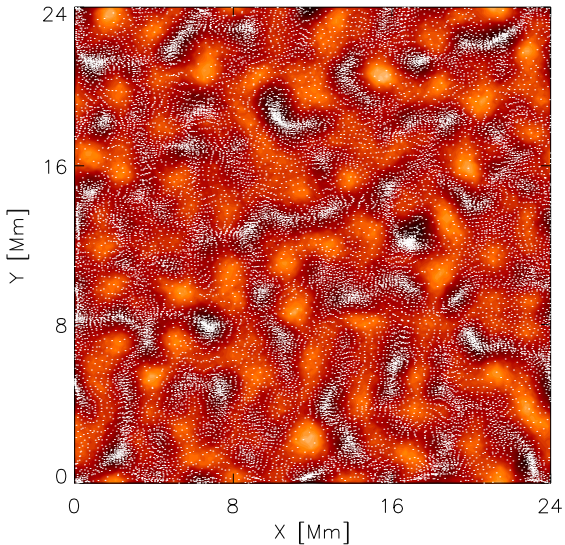

Figure 1.5: Divergence of the 60-minute average of the horizontal velocity obtained from a hydrodynamical simulation (MURaM code). Bright areas correspond to positive divergence (mesogranules). White points are corks positions after evolution time of 60 min from an uniform dense distribution.

Even though the evidence for a distinct convective flow on the mesoscale is weak, the existence of mesoscale patterns, supported by both observations and hydrodynamical simulations, seems undisputed. Additionally, the realistic three-dimensional hydrodynamical granulation simulations reach only a few megameters into the simulated solar surface, and the existence of the mesopatterns in these "shallow" models seems to rule

13

out He ionization as a necessary ingredient for mesogranulation (Ploner et al. 2000). The idea that mesoscale patterns may arise naturally from the granulation is not new, and over the years various effects have been proposed as possible mesogranulation causes. Among these, the exploding granules deserve special attention. An exploding granule leads to a positive velocity divergence at the granule position i.e., a horizontal outflow. The average granule lifetime is about ten minutes and the diameter of an exploder rarely exceeds 2 Mm, hence individual exploding granules cannot sustain the mesogranular pattern. Nevertheless, a sequence of neighboring exploder events could last long enough to produce a larger coherent velocity structure. Oda (1984) studied the surface distribution of fragmenting granules during a 4-minute time interval, and interpreted them to outline a meso-size pattern, while Hirzberger et al. (1997) found that fragmenters exist predominantly in the mesogranule centers. Simon et al. (1991) showed that a simple kinematic model of exploder events can reproduce cork patterns equivalent to those associated with mesogranulation. They modelled exploding granules as horizontal outflows with a Gaussian velocity profile, advecting initially uniform cork distribution. They concluded that a sequence of exploder events, normally distributed around a mesogranule center, can produce a cork pattern equivalent to the mesogranular one. On the other hand, a random distribution of exploders on the surface does not produce any coherent patterns in the kinematic model. The question whether exploders are organized on the solar surface was further explored by Roudier and coworkers (Rieutord et al. 2000, Roudier et al. 2003, Roudier et al. 2004). They analyzed recurrently fragmenting granules ("Trees of Fragmenting Granules", TFGs) and found that such TFGs are constantly present on the Sun. Moreover, they found that over 60% of the area covered by granules belonged to TFGs and that the lifetime of such granule families can reach many hours. From the power law behavior of the TFG's lifetime histograms they deduce that no characteristic timescale is present. The velocity field produced by a TFG, when averaged over the TFG's lifetime, yields a divergence area, with most of the TFGs covering an area of a diameter of ~6 Mm. Additionally, when performing the cork advection analysis, the authors found that the corks tend to accumulate in the areas of low granule splitting rates. All these features of the TFGs bear close resemblance to mesogranules and most probably each velocity divergence area (i.e. mesogranule) can be associated with a TFG. Nevertheless, that alone does not explain the mesogranulation phenomenon, but rather reformulates the question to what is the nature and origin of the TFGs. Summarizing, our perception of mesogranulation has evolved from a typical convective flow to a self-organization phenomenon of the granular field, with the recurrently fragmenting granules (TFGs) possibly playing a key role in the production of the mesoscale velocity patterns.

1.2 Cellular automata

The phenomenon of self-organization is exhibited by a wide family of systems, known as "cellular automata". In this work we show that granulation can be seen as a cellular automaton, hence we present a brief introduction to these systems.

The concept of cellular automata was originally introduced by von Neumann and Ulam as a possible idealization of biological systems (Ulam 1952, von Neumann 1963, 1966), aiming at modelling biological self-reproduction. Cellular automata are mathemat-

ical idealizations of physical systems in which space and time are discrete, and physical quantities, in the simplest cases, take on a finite set of discrete values. A cellular automaton consists of a lattice, usually infinite in extent, with a discrete variable at each lattice site ("cell"). It evolves in discrete timesteps according to given local interaction rules, with the value of the variable at one site being affected only by the values of variables at sites in its neighborhood at the previous timestep. The neighborhood of a site is usually taken to be the site itself and all immediately adjacent sites, and the variables at each site are updated simultaneously. As a consequence of their locality, cellular automata define no intrinsic length scale other than the cell size and no intrinsic time scale other than the duration of a single timestep. Even the simplest one-dimensional cases of cellular automata exhibit an intriguing property of "self-organization", where larger scale patterns evolve from the local interaction of many simple units ("cells"). The second law of thermodynamics yields that isolated microscopically reversible physical systems tend with time to states of maximal entropy, or "disorder". However, dissipative systems involving microscopic irreversibility (like cellular automata), or those open to interaction with their environment, may evolve from "disordered" to more "ordered" states, which can exhibit quite complicated structure (snowflakes, for example). Most cellular automata mappings are irreversible (many initial states may evolve to the same final state) and not surjective (not all possible configurations occur), so that the set of generated configurations contracts with time, which is reflected in decrease in its entropy (Packard & Wolfram 1985, Martin et al. 1984). The nature of cellular automata makes them ideal for numerical computing due to the necessity of solving simultaneously a large number of relatively simple equations. Moreover, numerical simulations of physical phenomena lead to discretization of all the involved variables, thus entering the natural domain of cellular automata. Physical systems which contain a large number of similar components with local interactions can be directly modelled as cellular automata, but, in general, any physical system satisfying differential equations may be approximated as a cellular automaton (Wolfram 1983). Nontrivial cellular automata are obtained when the interaction rules are nonlinear, as when the system exhibits some form of "growth inhibition". In the simplest cases, the cellular automaton is a lattice in space. For example, the sites may represent points in a crystal lattice, with values given by some quantized observable, or corresponding to types of atoms, etc. At a more macroscopic level, the sites may correspond to a region containing many molecules, and the value at each site may label one of several possible phases or compositions. In this way, cellular automata can be used as discrete models for nonlinear chemical systems involving a network of reactions coupled with spatial diffusion (Greenberg et al. 1978), or provide models for kinetic aspects of phase transitions (Harvey et al. 1982). Many biological systems have been modelled by cellular automata (Lindanmayer 1968, Kitagawa 1974, Ulam 1972, Rosen 1981). The development of structure and patterns in the growth of organisms often appears to be governed by very simple local rules (Thompson 1961) and therefore may be described with the cellular automata approach, an example being the leaf and branch arrangement (Stevens 1974). Furthermore, cellular automata approach has been applied to a wide variety of phenomena, like thundercloud electrification (Selvam 1998), spread of epidemic diseases (Quan-Xing et al. 2006), neuron interaction (Furtado & Copelli 2006), the influence of electoral surveys on the voting process (Alves et al. 2002) and social models of opinion formation (Bordogna & Albano 2006), to name just a few.
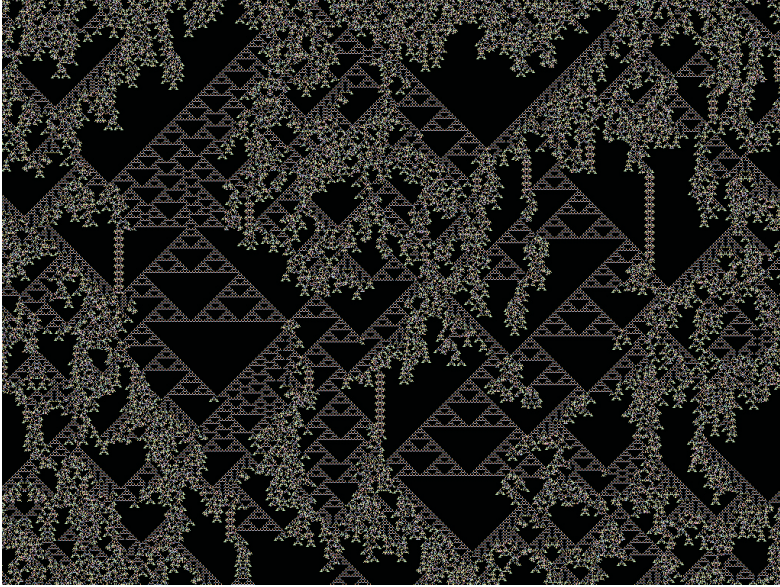
Figure 1.6: Example of patterns produced by a one dimensional cellular automaton. Time is on the inverted y-axis (top is time beginning). Courtesy of David J. Eck.

One-dimensional cellular automata may be divided into four classes, with the automata within one class exhibiting qualitatively similar behavior (Wolfram 1984). Such a small number of classes implies considerable universality in the behavior of cellular systems, rendering many construction details of cellular automata irrelevant in determining their behavior. In almost all cases, cellular automaton evolution is irreversible. Trajectories in the configuration space for the cellular automata therefore merge with time, and after many timesteps, trajectories starting from almost all initial configurations converge onto "attractors", which typically contain only a very small fraction of possible states. Such evolution to attractors from arbitrary initial conditions allows for "self-organization", where patterns may evolve from structureless initial states. The form and extent of the emerging structures depends on the nature of the attractors, and the four classes of cellular automata behavior characterize the type of these attractors (Wolfram 1983, 1984). The first three types are roughly analogous to the limit points, limit cycles and chaotic attractors found in dynamical systems. Cellular automata of the fourth class behave in a more complicated manner, and are conjectured to be capable of universal computation, so that their evolution may implement any finite algorithm. The different classes of cellular automata behavior allow different prediction levels of the outcome of the automaton evolution from given initial states. In the first class, the outcome is determined independent of the initial state. In the second class, the value at the particular

site at large times is determined by the initial values of sites within a limited region. In the third class, the value at a particular site depends on an ever-increasing number of initial sites, and random initial values lead to chaotic behavior. On the other hand, in class four cellular automata, a particular site value may depend on many initial site values, and may apparently be determined only by an algorithm equivalent in complexity to explicit simulation of the automaton evolution (Wolfram 1984). Hence, no meaningful prediction is possible and only explicit simulation yields the behavior of such systems. The division into the four classes of one-dimensional cellular automata mentioned above serves the conceptual understanding of possible evolution scenarios of such systems rather than being a strict rule. Some cellular automata exhibit features of more than one class, with separate regions yielding different type of structures (Wolfram 1984, Packard & Wolfram 1985). Figure. 1.6 present an example of such a one dimensional automaton.

A well-known example of a two-dimensional cellular automaton of the fourth class is the Game of Life, developed by John Horton Conway in 1970. The universe of the Game of Life is an infinite two-dimensional orthogonal grid of square cells, each of which is in one of two possible states, "live" or "dead". Every cell interacts with its eight neighbors, which are the cells that are directly horizontally, vertically, or diagonally adjacent. At each step in time, the following transitions occur: any live cell with fewer than two live neighbors dies, any live cell with more than three live neighbors also dies, any live cell with two or three live neighbors continues to live, and any dead cell with exactly three live neighbors comes to life. Started with an initial configuration of dead and live cells, the system evolves to exhibit many different larger scale patterns of live cells, including static patterns ("still lives"), repeating patterns ("oscillators"), and patterns that translate themselves across the board ("gliders"). Other, more complex patterns can evolve for long periods before stabilizing or disappearing, they can repeatedly produce gliders etc. In general, the set of relatively simple rules of Life leads to very complex dynamics (Gardner 1970). The Game of Life has also been shown to have the property of computational universality, implying that suitable initial configurations can specify arbitrary algorithmic procedures (Berlekamp et al. 1982). Hence, such automaton can be seen as a computer, able to evaluate any computable function, with the initial configuration being the input data which is processed in time by the rules of the automaton. It can therefore simulate any other system, given the proper initial state configuration. The proof of the computational universality is based on the existence of automaton structures which emulate components of a standard digital computer. It should be noted that only infinite cellular automata may be capable of universal computation. Figure. 1.7 shows an example of the patterns arising in the Conway's automaton. It seems that two-dimensional cellular automata bear some local resemblance to one-dimensional cases, and the same four classes of behavior can be identified (Packard & Wolfram 1985). Nevertheless, many of the phenomena found in the two-dimensional cases depend on the geometry of the lattice, involving complicated boundaries and interfaces, rendering formal prediction of the system's behavior even more difficult than in the one-dimensional cases. Cellular automata in which the lattice itself is subject to change in time are labelled "dynamic environment" automata, and in general the more degrees of freedom the system has the more complex the resulting structures are (Packard & Wolfram 1985). Due to the intrinsic unpredictability of the behavior of most (non-trivial) cellular automata, particularly in two spatial dimensions, it is hard to generalize their behavior beyond the four classes already mentioned. Lacking the proper
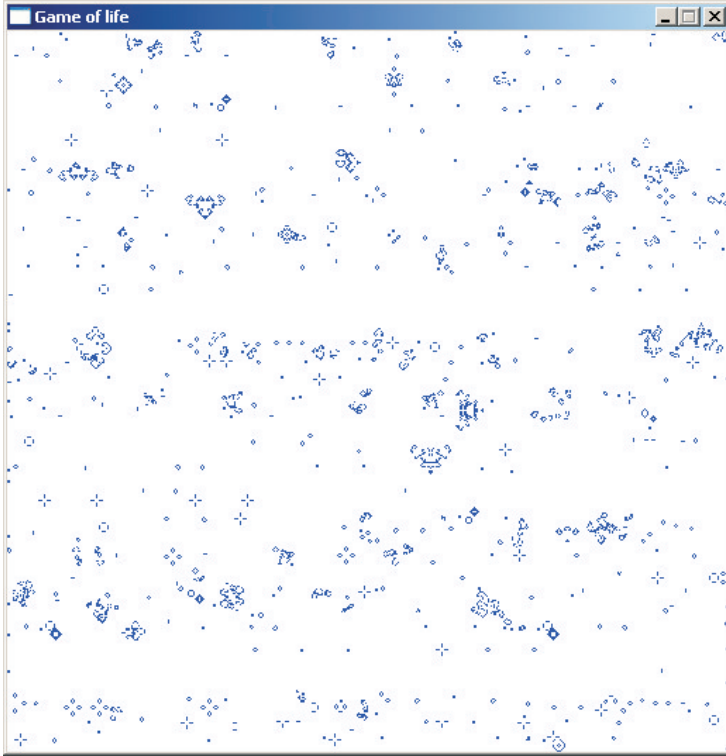
Figure 1.7: Example of a realization of the John Conway's Game of Life. Blue are the "live" cells.

description language, and, many times, also a clear definition of "self-organization", the investigation of most automata reduces to the direct computation of their evolution.

Solar granulation is an example of a physical phenomenon that can be modelled in terms of cellular automata. Even though the plasma flow is very turbulent, the convective cells (granules) persist for up to several minutes as distinct structures and can be described statistically in terms of their lifetime and size. It is also true that the granules interact only locally with each other, although the detailed nature of this interaction is not entirely clear. It is known that the exploding granules grow during their lifetime and effectively either overflow or squeeze their neighbors. Although these two possibilities are quite different in nature, they both lead to the same result, namely that the downflow lane surrounding such an exploder is also translated in space, and the spatial structure of the neighboring granules is rearranged accordingly. The evolution of the dissolvers is easier to compre-

hend. The center upflow, which spawns the granule by supplying hot plasma from below, diminishes with time, and the granule diminishes accordingly, producing the effect of the surrounding downflow lanes closing in on the hot center till it disappears altogether, i.e. the downflows merge. Hence we employ the following picture in constructing a cellular automaton model of granulation: the granules interact only locally at their common borders (downflow lanes) through the horizontal pressure they exert on each other. When the pressure on one side of a downflow is lower (the granule on that side is smaller), the downflow is pushed in that direction, effectively working to shrink or move the smaller granule. Additionally, granules disappear or fragment when their size reaches a critical value (as already mentioned in previous section, solar granulation can be justifiably seen as composed only of dissolvers and fragmenters). The fragmenting process constitutes a growth inhibitor for the granules, ensuring an equilibrium state in which the average granule size and lifetime remain constant in time. Granulation as a cellular automaton is a dynamic environment system, in which the position and the very existence of cells (granules) is subject to change. The values assigned to cells in case of granulation can be their size and/or position, or rather the translation of the position in time (i.e. velocity). By analogy to other cellular automata, one can expect such a system to exhibit self-organization, with granular size and translation velocities arranged spatially on scales larger than the granulation cell size.

This thesis presents an investigation of the mesogranulation phenomenon as a surface self-arrangement effect of the granulation. We present cellular automaton models, both one- and two-dimensional, that capture the granulation characteristics in terms of cell lifetime and size distributions, and we are able to show that mesogranulation emerges naturally in such a system. We compare the results with those from a realistic hydrodynamic simulation and find good agreement, additionally showing that mesogranulation is a robust feature, not depending strongly on the detailed granule interaction rules. In Chapter 2 we describe a simple one-dimensional granulation model, which helps to understand the concept and is an intermediate step towards the two-dimensional model. Chapter 3 describes the two-dimensional cellular model of granulation and the emerging mesogranulation properties. Many versions of the model are presented and analyzed to check how different cell interaction rules affect the mesogranular properties. Additionally, different mesogranulation detection methods are applied. It turns out that mesogranulation emerges naturally in such a cell system. In Chapter 4 we analyze mesogranulation emerging in a three-dimensional hydrodynamical simulation. This allows for comparison of mesogranule properties coming from the cell model and the more realistic simulation, and we find astonishingly good agreement between the two. Chapter 5 deals in more detail with the spatial scale of mesogranulation and how it depends on different analysis methods and parameters. In Chapter 6 we compare the results obtained from the cellular and hydrodynamical models with solar observations. We discuss the similarities and differences, additionally addressing other phenomena like the spatial distribution of granule types and the long-lived downflows. Chapter 7 contains the final conclusions.

2 One-dimensional model

2.1 Model description

The model has one spatial dimension and traces the evolution of artificial granules in time, hence producing plots of granule positions versus time. The model is quite simple and does not aim at quantitative reproduction of solar granulation, but rather serves to introduce the concept of parameterizing granulation as a cell system. It also allows a comparison with two-dimensional hydrodynamic simulations (depth plus one horizontal coordinate) by Ploner et al. (2000) and Steiner (2003). The granules are defined as the regions between the intergranular lanes, which are simple points in this model. These points start from an initial distribution and move along the spatial dimension in time, therefore producing lines that run along the time axis. Thus, at any given time, there is a number of granules present in the simulation, their sizes being the distances between neighboring points. The spatial domain is periodic: a point "escaping" through the end of
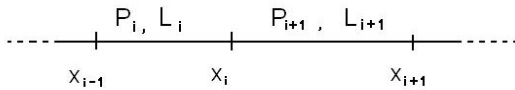
Figure 2.1: A sketch illustrating the one dimensional model construction, see text.

the domain appears at the beginning of it and vice versa. We consider a "cell competition" model, meaning that the movement of any given point (intergranular lane) at each time step is determined by a "pressure" exerted on it by the granules that the point separates. The point moves towards lower pressure. In a nearly stationary flow situation (evolving slowly compared with the acoustic timescale) one can stipulate a relation between granule size and the pressure at its boundary: the larger the granule is, the higher the pressure excess above its center must be to deflect the rising plasma horizontally and sustain the granular circulation. Form the Bernoulli principle it follows that this pressure excess is accompanied by corresponding pressure excess at the cell boundary (intergranular lane), which in turn deflects the plasma downwards (Stein et al. 1998, Stein & Nordlund 1998). We therefore assume the following rules of intergranular lane movement in the model: let

x_i be the spatial position of i-th point, then

$$\frac{d^2 x_i}{dt^2} = -\alpha(P_{i+1} - P_i) = -\beta(L_{i+1}^k - L_i^k) \qquad (2.1)$$

where P_i is the pressure exerted on the point x_i by the granule defined by the interval $[x_{i-1}, x_i]$ and L_i is the size of that granule (see Fig. 2.1). α and β are proportionality constants, k is the pressure-size dependence exponent (a free parameter in the model), unless stated otherwise, $k = 1$. Hence, intergranular lanes are points of pressure discontinuity in the model. When two points meet, they merge, marking a disappearance of a granule. This accounts for dissolving granules. On the other hand, when an expanding granule reaches a critical size, it is assumed to split in two, with a new point (intergranular lane) appearing. From observations and numerical simulations it is known that fragmenters are statistically larger and less uniform in size then dissolvers (Hirzberger et al. 1997, Ploner 1998, Müller et al. 2001). In order to reproduce this property, in our model the critical splitting size S_{crit} for fragmenters is set to:

$$S_{\mathrm{crit}} = 4 + 2R_1 + \frac{R_2}{2}[\mathrm{Mm}] \qquad (2.2)$$

where R_1 is an uniformly distributed random number in the range $[0,1]$ and R_2 is a normally distributed random number with both variance and standard deviation equal to unity. The random components R_1 and R_2 of the critical splitting size S_{crit} are evaluated individually for each granule in each timestep. The position x_n of the new-born intergranular lane is chosen randomly within the middle third part of the splitting granule. The formula is

$$x_n = x_{i-1} + \frac{1}{3}S_{\mathrm{crit}}(1 + R_3) \qquad (2.3)$$

where x_{i-1} is the position of the left-hand intergranular lane of the splitting cell and R_3 is an uniformly distributed random number in the range $[0,1]$. The model does not account for disappearance of intergranular lanes, that is for granule merging. Hence lanes can appear, but not disappear other than by lane merging (a dissolving granule disappearance). Figure. 2.2 present an example of a granule evolution plot.

2.2 Granule properties

The time scale of the model is fixed by the requirement that the mean granule lifetime agrees with that given by the two-dimensional (the vertical plus one horizontal dimension) hydrodynamical simulation of Ploner (1998). We choose Ploner's simulation in order to compare the obtained values with his detailed granulation characteristics. Figure. 2.3a present lifetime histograms of dissolvers and fragmenters of a simulation equivalent to that of Fig. 2.2 but run in a larger domain (400 Mm x 20 hours) to include more granules. The mean lifetimes are $\tau_{\mathrm{diss}} = 74.1$ timesteps for dissolvers and $\tau_{\mathrm{expl}} = 73.3$ timesteps for fragmenters. Thus, after scaling the mean timestep lifetime value 73.7 with mean granule lifetime 8.2 minutes (after Ploner, 1998) one can evaluate the timespan of Fig. 2.2 to be 4000 timesteps = 445 min = 7.4 h. Fig. 2.3b shows the size distributions of dissolvers and fragmenters, with mean values $s_{\mathrm{diss}} = 1.08$ Mm and $s_{\mathrm{expl}} = 2.73$ Mm, while
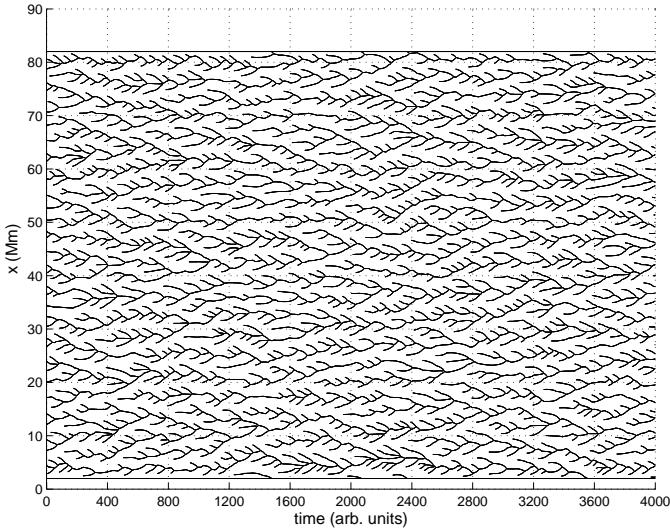
Figure 2.2: Example of a granule evolution plot of a cell-competition model (Eq. 2.1). Dark lines represent the time evolution of intergranular "lanes". Two lanes merging mark a disappearance of a granule (dissolving granule), while an appearing of a new lane splits an existing granule (exploding granule).

Fig. 2.3c is a scatter plot of granular lifetime versus size. The size of a granule is taken as the average over its lifetime. Figure. 2.4 presents the corresponding granule properties from the two-dimensional hydrodynamical simulation of Ploner (1998). From Fig. 2.3 it is clear that there is little overlapping of granule sizes between dissolvers and fragmenters. Nevertheless, the long lived granules approach the mean size regardless of the way they disappear. Therefore the mean size seems to be the "natural" granule size. The distributions in Fig. 2.4 show similar separation of sizes between dissolvers and fragmenters in the hydrodynamical simulation. In Fig. 2.3c the maximum size of a dissolver for a given lifetime is bounded by a smooth curve. It can be explained as follows: granules are born in pairs when the "parent" granule fragments. Of such pair, on average one is a dissolver and one is an fragmenter. This can be certified in Fig. 2.2 and with the fact that the number of fragmenters and dissolvers in the simulation is practically the same (within 0.1%). The bounding curve in Fig. 2.3c is obtained when one evaluates the size-lifetime relation of a dissolver formed in a dissolver-fragmenter pair by fragmentation of a stationary parent granule with a fixed size (evolution of a point between two straight parallel walls). This upper limit for the granule size of the short-lived dissolvers means, that during the evolution of such granules the granule lanes never diverge from each other. This can also be verified by close examination of Fig. 2.2. No bounding curves are present in case of
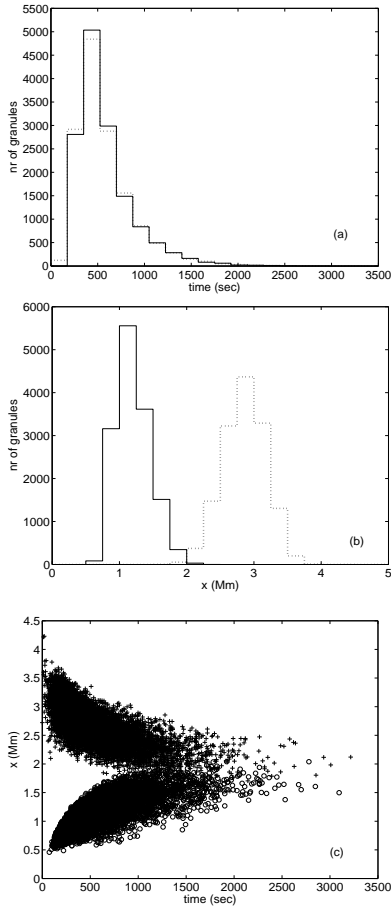
Figure 2.3: Histograms of granule lifetime (a) and size (b); (c) is a scatter plot of size versus lifetime. Solid line/circles are dissolvers, dotted line/crosses are fragmenters.

fragmenters, because both the times of appearance and vanishing of an fragmenter contain random components (see the "Model description" section). Nevertheless, if a fragmenter has a short lifetime, it means it was large enough to fulfill the splitting criterion soon after it was born. This is reflected in the fragmenter distribution in Fig. 2.3c, with the largest fragmenters being also the shortest-lived ones. The distribution of granules in the hydro-dynamical simulation (Fig. 2.4, bottom panel) does not show grouping similar to that of
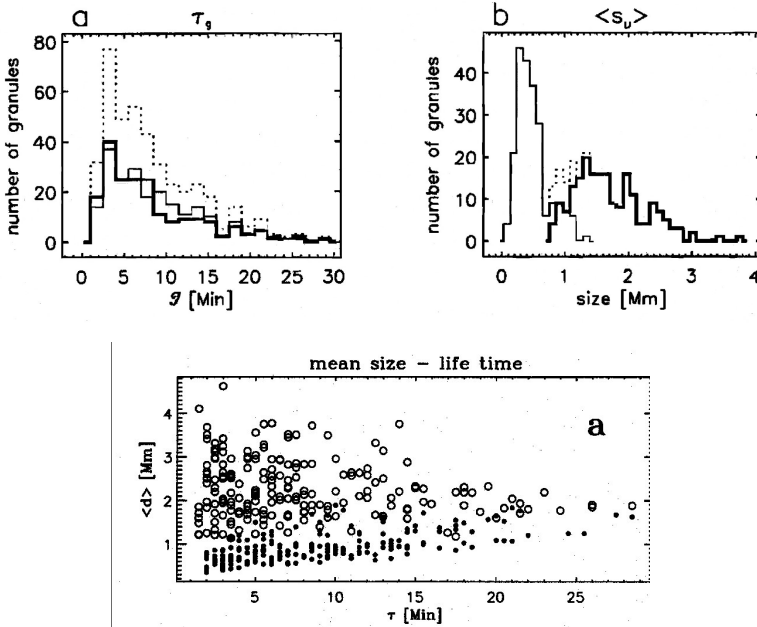
Figure 2.4: Granule properties from the 2D simulation of Ploner (1998). Top left: histograms of granule lifetimes, top right: histograms of granule sizes, bottom: a scatter plot of size versus lifetime. Bold solid line/circles are fragmenters, thin solid line/dots are fragmenters. Dashed line: dissolvers and fragmenters together.

the cell-competition model (Fig. 2.3c). First, the number of granules in Fig. 2.4 is much less than in Fig. 2.3c, hence it is possible that more data points are needed in Fig. 2.4 to clearly distinguish between the dissolver and fragmenter grouping regions in the figure. Nevertheless, the bounding region in Fig. 2.3c is a direct effect of the cell-competition rule of Eqs. (2.1) or (2.4), which in turn is a greatly simplified attempt to describe a very dynamical turbulent phenomenon of the granular flow. Therefore, it is not expected that the more realistic results from hydrodynamical simulations show such clear indications of the pressure-size relation of Eqs. (2.1) or (2.4).

Table 2.1 summarizes the averaged granular parameters derived from the model. (Note: since we scale lifetime in our model to match the results of Ploner (1998), only the relation between the dissolver and fragmenter lifetimes is relevant.) Although the model is very simple and does not include a gross part of the phenomena thought to be relevant to granulation, it reproduces quite well the simulated granules of Ploner (1998) (compare Fig. 2.3 and Fig. 2.4, parameters also included in Table 2.1). This indicates that although granulation is a dynamical flow of convective origin, it can be parameterized by

25

Table 2.1: Granulation characteristics.

parameter	diss	expl	diss+expl
lifetime(min)	8.2	8.2	8.2
Ploner(1998)	8.6 ± 5.6	7.9 ± 5.8	8.2 ± 5.7
size(Mm)	1.1	2.7	1.9
Ploner(1998)	1.3 ± 0.5	2.7 ± 0.8	2 ± 1.0

a simplified cell system without loss of the statistical characteristics of the granules.

It is interesting to observe that the patterns arising from the model run with the left hand side of Eq. 2.1 changed to velocity, that is for

$$\frac{dx_i}{dt} = -\alpha(P_{i+1} - P_i) = -\beta(L_{i+1}^k - L_i^k) \tag{2.4}$$

do not change significantly. x_i is the spatial position of i-th point, P_i is the pressure exerted on the point x_i by the granule defined by points $[x_{i-1}, x_i]$ and L_i is the size of that granule (see Fig. 2.1). α and β are proportionality constants, k is the pressure-size dependence exponent (a free parameter in the model). Figure. 2.5 shows granule scatter plot of size versus lifetime run with Eq. 2.4.
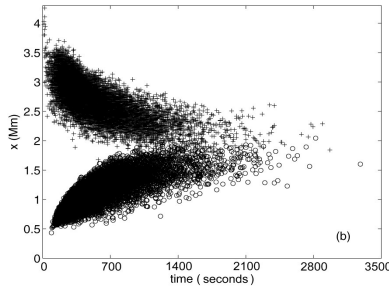
Figure 2.5: Scatter plots of granule size versus lifetime for Eq. 2.4. Circles represent dissolvers, crosses are fragmenters

2.3 Mesogranulation

2.3.1 Detection and characteristics

A convenient way to detect mesogranulation in observational data and hydrodynamical simulations is by means of "corks", test particles being passively advected by the horizontal flow at a given height. The corks are introduced into the fluid and after a few granule lifetimes they tend to gather in the long-lived intergranular lanes, which mark

places of horizontal velocity convergence (downflows). These structures have lifetimes much longer than average granule lifetime and outline areas of horizontal fluid divergence which are suggested to represent mesogranules (Simon et al. 1991, Ploner et al. 2000, Rieutord et al. 2000, Roudier et al. 2003, Cattaneo et al. 2001). Averaging the horizontal velocity over the cork evolution time (given time interval since the moment of cork introduction) can indeed produce a mesostructure with uniform radial outflow from the center of a mesocell, although the instantaneous velocities within the mesocell area do not have to be either radial or uniform (Rieutord et al. 2000). In our toy-model there are no explicit fluid velocities, but motivated by the results of the two-dimensional HD simulation (Ploner et al. 2000) we argue that an intergranular lane that lives long enough will accumulate enough corks to become a mesogranular border-lane. This is how we define mesogranulation in the model, and we mark intergranular lanes that have lifetime longer than a given threshold time t_0 as mesogranular. Whenever two lanes merge, we keep the lifetime of the older one. Figure. 2.6 is the same as Fig. 2.2 but with the mesogranular lanes marked as thick for $t_0 = 440$ timesteps (corresponding to 50 min). The
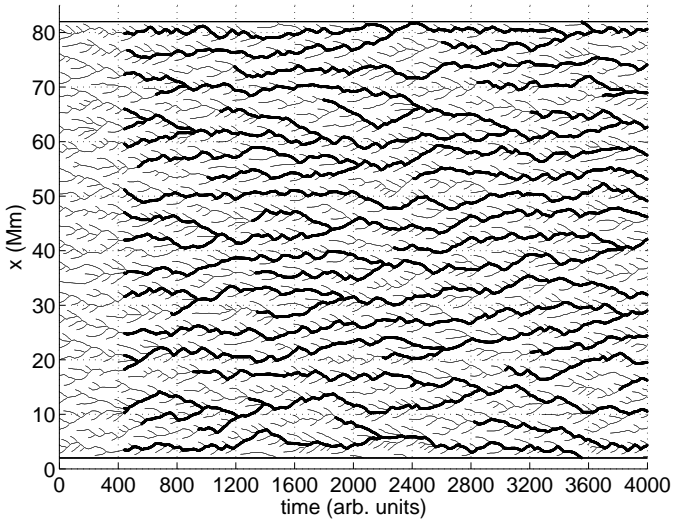
Figure 2.6: Plot of Fig. 2.2 with mesogranular lines marked as thick for lifetime $t_0 = 440$ timesteps (50 min). Timespan of the domain is 445 min.

mesogranules can also be divided into meso-exploders and meso-dissolvers, according to the means of their decay. As such, it is interesting to see whether the properties of the t_0-defined mesogranulation are qualitatively different from those of granulation. Figure. 2.7a-b present lifetime and size distribution of mesogranules from the model run depicted in Fig. 2.6, respectively (again run in the large domain to include more mesogranules). Figure. 2.7c is a scatter plot of mesogranular lifetime versus size. Table 2.2

Table 2.2: Mesogranulation characteristics for threshold time $t_0 \sim 50$ min

parameter	mesodiss	mesoexpl	mesodiss+mesoexpl
lifetime(min)	91.8	111.6	101.7
Ploner(1998)	–	–	$60 - 120$
size(Mm)	2.8	5.8	4.3
Ploner(1998)	–	–	7

contains a summary of averaged mesogranular characteristics for threshold time $t_0 \sim 50$ min. The lifetime value $60 - 120$ min given by Ploner (1998) is not an average, but a range in which most of the lifetimes were found. Provided that the calculation domain is large enough to include a statistically sufficient number of mesogranules (ex. 400 Mm x 19 h), we do not find any deviation of detected mesogranular values between many simulation runs. Comparing Figures 2.3 and 2.7 leads to the conclusion that mesogranulation detected in this manner bears some similarities to granulation. Like the granules, the mesogranules approach the mean size with increasing lifetime regardless of whether they are mesodissolvers or mesoexploders. This is not surprising, since the mode of death does not depend on the history of a granule/mesogranule and has little effect on the mean size provided that the structure lives long enough. The mean size is such that a (meso)granule can remain so for a long time because it is neither probable that it splits, nor does it face being squeezed by the neighbors.

In Fig. 2.7c there is a separation of meso-fragmenters and meso-dissolvers similar to that of Fig. 2.3c for granules, and similar arguments can be employed to explain it. Like granules, the mesogranules in the model can only be born through fragmentation of the parent object. The splitting mechanism is not explicitly built into the mesogranule evolution, but rather follows from the granular motions. The fact that in Fig. 2.7c the largest meso-exploders are the shortest-lived ones can be explained as follows: if a mesogranule is large, then the probability of its splitting is proportionally larger than for a smaller meso-exploder, because it is more likely that long-lived intergranular lanes already exist within the mesocell interior. Hence it takes less time for these lanes to reach the critical mesogranular lifetime t_0, therefore splitting the cell. What is more interesting, Fig. 2.7c also shows a tendency for short-lived meso-dissolvers to be grouped and bounded similarly to dissolvers in Fig. 2.3c. This behavior of mesogranules is an indirect indication of an average mesoscale network existence, since it is the network that bounds the evolution of these new-born meso-dissolvers, setting the lifetime-size dependence. Like in case of the granules, the bounding curve of the maximum size-lifetime dependence is equivalent to a lane evolution between two straight parallel walls according to rules of equation 2.1 or 2.4. This means that in the one-dimensional model the t_0-defined mesogranule evolution can be roughly approximated with the size-pressure scheme of equations 2.1 (2.4).

2.3.2 Dependence on parameters

The mesogranular features present in the simulation may depend in principle on the model parameters y (see Eq. 2.1) and t_0 (threshold time). However, we have found that the av-
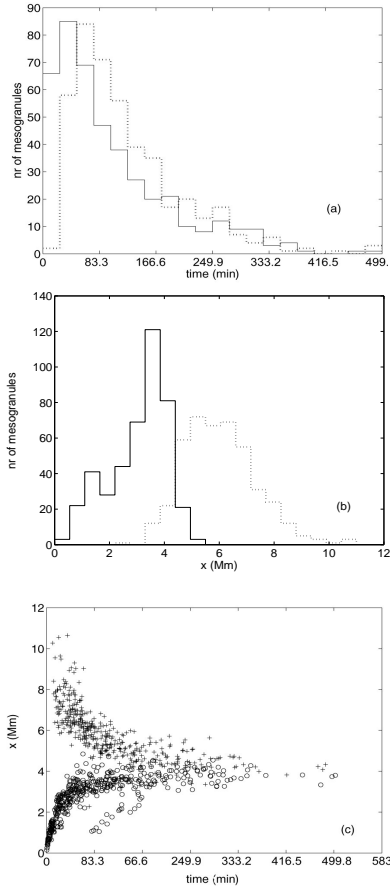
Figure 2.7: Mesogranule lifetime (a) and size (b) histograms, (c) is a scatter plot of size versus lifetime. Solid line/circles are meso-dissolvers, dotted line/crosses are meso-exploders.

erage mesoscale size and lifetime virtually do not change for y between 1 and 3. This is an indication that mesogranulation in our model is a feature of the cellular structure and is independent of the detailed properties of the granule interaction. Figure. 2.8 shows how the average mesogranular lifetime and size change with t_0 in the range between 15 min and 4 hours. Fig. 2.8 indicates that the choice of the threshold time t_0 influences the detected mesogranular features. Apart from the first hour, the increase of size and
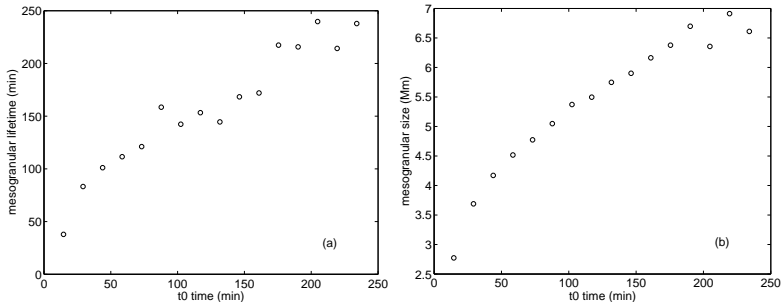
Figure 2.8: Dependence of the average mesogranule lifetime (a) and size (b) on the threshold time t_0.

lifetime of mesogranules in the cell-competition model is linear. The increase of the detected meso-characteristics with the threshold time in such simple one-dimensional model is not surprising. The larger t_0 is, the fewer intergranular lanes have reached this value and are present in the domain at a given moment. Hence, the larger the separation between the lanes i.e., the mesogranular size. A mesogranule can only disappear when two mesolanes merge, or a new mesolane appears. When the distance between the mesolanes is larger, it takes longer for them to meet and merge, hence the increase of the lifetime. The same logic applies to splitting of mesogranules, if the t_0 is large, it takes longer for the intergranular lanes within a mesogranule to become mesolanes and split the existing mesocell. Concluding, the t_0-defined mesogranulation in the model has no intrinsic time- and length-scale, since the measured values depend on the choice of the threshold time t_0.

2.4 Comparison with a random-walk model

We will now study how strongly the granule interaction rules affect the mesogranular properties. Therefore, we have constructed a random-walk granulation cell model, for which the previous rules of lane movement (Eq. (2.1) or (2.4)) are replaced by a random displacement (with normal distribution). To keep the time scale comparable with the cell-competition model the velocities of lane movement have to be larger, since a randomly walking lane changes the direction of motion much more frequently and hence travels a shorter distance in a given direction then a pressure-driven lane. The average lane velocities found in the random-walk model are of order of 2 kms^{-1}, a factor of 3 larger than in the cell-competition case ($\sim$0.7 kms^{-1}). One way to compare the effects of the different interaction rules is to consider the number of the oldest lanes in the simulation, i.e. lanes that start at $t = 0$ (zero-lanes). Their number can decrease in time only by merging of such lanes, in which case we keep the lifetime of the older one. In case of lanes performing a random walk in the domain one expects their number to decrease as $\sqrt{t}^{-1}$ since the rms displacement of a random lane is proportional to $\sqrt{t}$ (Chandrasekhar,

1943). Figure 2.9 shows the number of zero lanes versus time for the cell competition and random-walk models, fitted with function $N(t) = A\sqrt{t}^{-1}$ (dashed line). Obviously, for both models the decrease of the number of zero-lanes is consistent with the $\sqrt{t}^{-1}$ law. Hence we conclude that the difference between the two models lies predominantly in the small-scale interaction, and the resulting average motion of the zero-lanes in the cell competition case is indistinguishable from a random one. Fig. 2.10 presents the
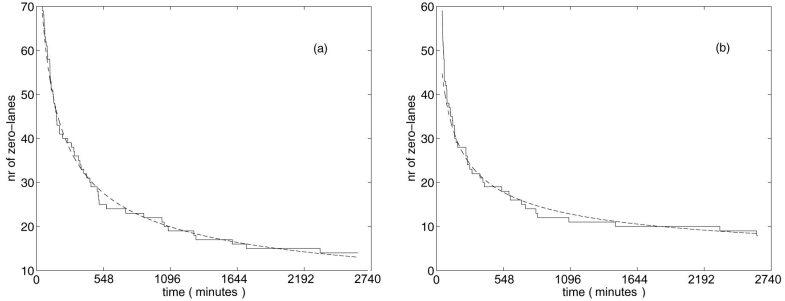
Figure 2.9: Time evolution of the number of zero-lanes in (a) cell-competition and (b) random-walk model

random model example of the granule and mesogranule evolution, equivalent of Fig. 2.6 for the cell competition model, while Fig. 2.11a-b show granulation lifetime and size distributions of a random walk model. Figure. 2.11c is a scatter plot of granular lifetimes versus size which can be compared with Fig. 2.3c. Similarly, Fig. 2.12 is the random model equivalent of Fig. 2.7, presenting mesogranular scale characteristics. In Fig. 2.12c one can see that short-lived meso-dissolvers in the random model are bounded, similarly to meso-dissolvers of the competition model in Fig. 2.7c. Again, one can see that as an indication of the mesoscale network existence. It can also be seen that the envelope bounding the mesodissolvers extends to longer lifetimes in case of the competition model (Fig. 2.7c). This means that the "coherence" time (the time interval during which the mesodissolvers can be approximated as evolving between straight parallel walls) of the meso-network is shorter for the random-walk model, hence it is less regular than in the cell-competition case. This can be seen directly by comparing Fig. 2.6 and Fig. 2.10. Table 2.3 summarizes the granule and mesogranule statistics for the random walk model (threshold time $t_0 \sim 50$ min).
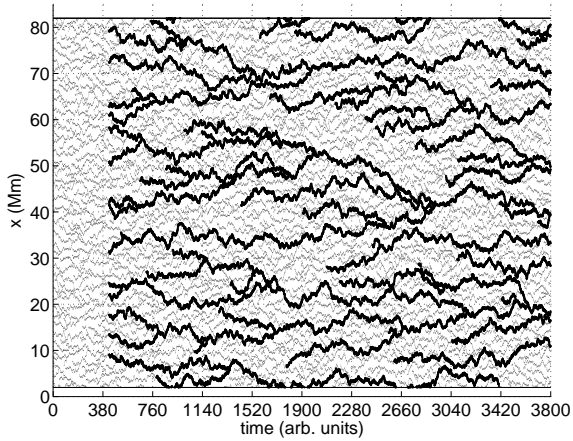
Figure 2.10: Random walk model equivalent of Fig. 2.6. Timespan of the domain is 445 min

Table 2.3: Granulation and mesogranulation characteristics for random walk model (the threshold time $t_0 \sim 50$ min)

parameter	diss	expl	diss+expl
lifetime(min)	8.0	8.4	8.2
Ploner(1998)	8.6 ± 5.6	7.9 ± 5.8	8.2 ± 5.7
size(Mm)	1.4	2.5	2.0
Ploner(1998)	1.3 ± 0.5	2.7 ± 0.8	2.0 ± 1.0
parameter	mesodiss	mesoexpl	mesodiss+mesoexpl
lifetime(min)	43.7	66.4	55.0
Ploner(1998)	–	–	60 − 120
size(Mm)	2.9	8.0	5.4
Ploner(1998)	–	–	7
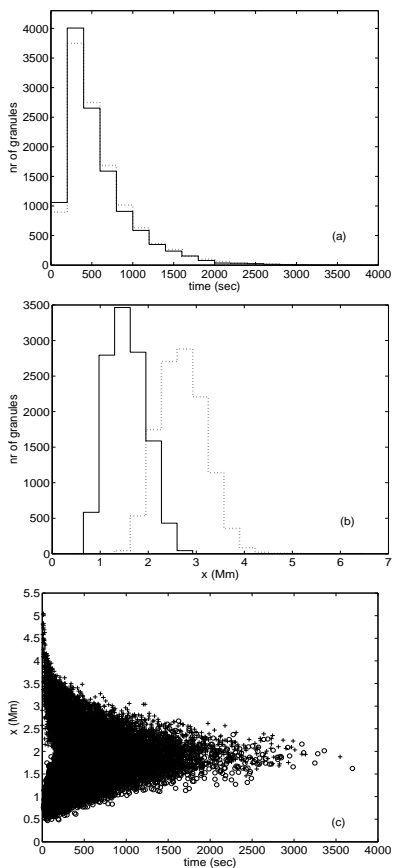
Figure 2.11: Granule lifetime (a) and size (b) histograms, (c) is a scatter plot of size versus lifetime. Solid line/circles are dissolvers, dotted line/crosses are exploders. Random walk model equivalent of Fig. 2.3
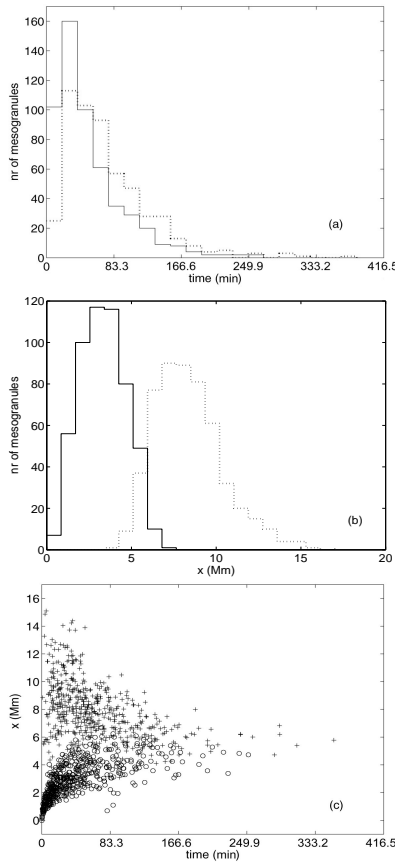
Figure 2.12: Mesogranule lifetime (a) and size (b) histograms, (c) is a scatter plot of size versus lifetime. Solid line/circles are mesodissolvers, dotted line/crosses are meso-exploders. Random walk model equivalent of Fig. 2.7

Comparing Figures 2.3 and 2.11 one can notice that although the average granule size in the cell competition and random walk models is roughly the same, there is more overlapping of dissolver and exploder sizes in the latter. This is due to the fact that in the random-walk model the systematic effect of competition is missing, and hence the fate of the offspring granules bears less dependence on the position of the new lane. Therefore, for short-lived granules it is less clear which become dissolvers and which exploders than it is in the cell-competition case. Since the granule statistics derived from an hydrodynamic simulation of Ploner (1998) show little overlapping, this would favor the cell competition model as the one giving better approximation to the phenomenon.

Figure. 2.13 presents the dependence of mesogranular lifetime and size on t_0 for the random walk model, equivalent to Fig. 2.8 of the cell-competition case. Apart from a slight nonlinearity for $t_0 < 1$h in Fig. 2.8, which is not present in the random model results, the dependence of the mesoscale characteristics on the threshold time is similarly linear for both models. For a given t_0 the mesogranular sizes given by the cell-competition model are smaller than those produced in the random model. On the other hand, for a given t_0 mesogranular lifetimes are larger for the competition model than for the random-walk one. In the random walk model (Fig. 2.13a) the average mesogranule lifetime yields the threshold time t_0, while in the cell-competition model (Fig. 2.8a) these lifetime values are slightly larger than the t_0. For $t_0 = 1$h the random-walk meso-lifetime is half of the cell-competition one (~50 min and ~100 min, respectively).
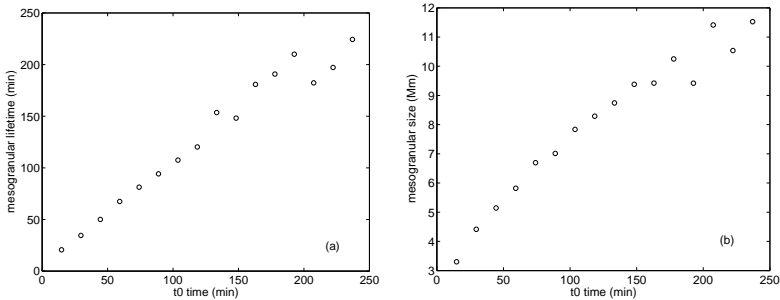
Figure 2.13: Mesogranule lifetime (a) and size (b) dependance on the threshold time t_0 for the random walk model.

2.5   Discussion

The main conclusion from the one-dimensional model is that the granulation size and lifetime properties can be reproduced with such a simplified cell system. Moreover, the t_0-defined mesogranulation emerges as a robust property of the model, only weakly depending on the detailed granule interaction schemes. The simple rules of splitting and disappearing of granules result in a self-arrangement of the system and emergence of larger scale pattern. The differences between the random walk and the cell-competition cases

lie predominantly in the small scales (Fig. 2.9) and the resulting statistical properties of mesogranules are quite similar for the two models. The dependence of the mesogranular size and lifetime on the threshold time is also roughly the same for the two versions of the model, and suggests that there is no characteristic scale associated with the phenomenon in the one-dimensional case. The lifetime-size dependence of the short-lived mesodissolvers in the cell-competition model, visible in the scatter plot in Fig. 2.7c, corresponds to the similar behavior of dissolving granules in the model (Fig. 2.3c). Such grouping effect is the result of the pressure-size relation of equation 2.1 (2.4), with the bounding curve of the region in which the cell characteristics tend to group corresponding to the size-lifetime relation of a dissolver, created in a dissolver-fragmenter pair by splitting of a parent granule of a constant size. In other words, such dissolver-fragmenter pairs evolve as if bound by straight parallel walls. The existence of this effect also for mesodissolvers indicates the effective existence of an average mesogranular network, and suggests that mesogranule evolution in the cell-competition model ca also be roughly approximated by the size-pressure relation of equation 2.1 (2.4) applied to mesocells. Interestingly, a self-similar behavior of the cellular flow structures has been conjectured by recent hydrodynamical simulations (Stein et al. 2006). In the random-walk model traces of this effect can be found only for the very short-lived mesodissolvers, which suggests a much shorter "coherence" time of the mesonetwork. Nevertheless, this model is too simple to draw conclusions about the three-dimensional phenomenon on the Sun. Even if the granular arrangement and mesogranulation emergence is a surface effect, it still requires at least two dimensions to describe it properly. The one-dimensional model qualifies as a class one cellular automaton, meaning that the resulting mesogranular lane pattern does not depend on the initial configuration of granules. The model has been run many times, always starting with a different randomized initial state, and it always converges quickly to the patterns seen in Figs. 2.6 and 2.10. This is predominantly due to the granule splitting mechanism, which prevents indiscriminate cell growth. The splitting and vanishing of cells also introduce a timescale in the model, which is the average granule lifetime.

3 Two-dimensional model

3.1 Motivation

As seen in the previous chapter, statistical properties of solar granulation in one dimension can be reproduced by a simple cellular automaton model. In principle, this should also be possible in two spatial dimensions. Such a two-dimensional model is much more interesting due to the fact that solar granulation pattern on the surface is two-dimensional. The granular flow itself is a three-dimensional convective phenomenon and as such cannot be reproduced by a surface model. Nevertheless, we do not aim at describing the hydrodynamical plasma flow, but rather at a parameterization of the cellular flow pattern in terms of mutually interacting two-dimensional cells. The model presented here is a two-dimensional extension of the one-dimensional cellular automaton model described in the previous chapter. One more spatial dimension poses many more challenges in constructing the model, most obvious of them being the shape of the cells. For simplicity we parameterize the granules as triangles. The cell evolution is parameterized through the motion of the vertices, which translate on the plane according to a given set of rules. As in the one-dimensional case, we present two distinct types of vertex interaction, the random walk and cell-competition schemes. The splitting and vanishing of cells in two dimensions present additional questions which must be dealt with. For example, to keep the triangular cell structure, the splitting procedure has to affect two adjacent cells simultaneously. Since one method of mesogranulation detection involves the age of the structures, the age inheritance rules when splitting and removing cells have to be set properly. The details of the model construction are discussed in the following sections. The one-dimensional model results encourage the construction of the two-dimensional version by producing larger scale patterns similar to mesogranulation. As will be seen in this chapter, the two-dimensional model also exhibits this property.

3.2 Model description

3.2.1 Initial conditions

We model granules as space-filling triangles on a square plane. We start with a square grid of points which constitute the vertices of triangular cells. Each initial vertex position has a random component to avoid artificial pattern formation and shorten the initial transient state phase of the model. The size of the grid d (d^2 being the number of vertices) is a free parameter. Figure. 3.1 is an example of an initial plane triangulation for $d = 12$. The outer square outlines the domain. The domain is periodic, meaning that the outermost vertices
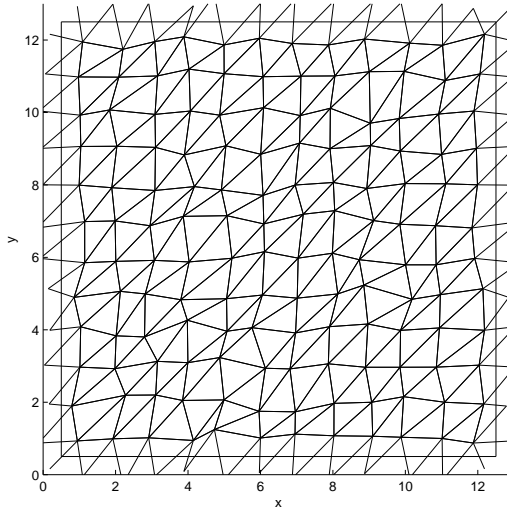
Figure 3.1: Example of initial plane triangulation for number of vertices $d^2 = 144$

on opposite sides of the domain are connected with each other to form triangles in the same manner as vertices inside the domain do. These "periodic" connections are visible on Fig. 3.1 as those that cross the domain boundary.

3.2.2   Data structure

Each vertex in the model has a unique index N and six arrays assigned to it: a position array $[X, Y]$, vertex age array, link array (containing indices of vertices connected to the vertex), two link-type arrays (one for each spatial dimension), determining the type of connections of vertex N to vertices in the link array, and a connection age array, containing the age of connections to vertices in the link array. The values in the link-type and connection age arrays describe connections with vertices whose index occupies a corresponding location in the link array. The values in the link-type array can be either 0, -1 or 1. Zero means that the connection is within the domain, while 1 is a cross-boundary connection directed from vertex N through the right/uppper boundary and -1 means a connection through the left/lower boundary. It follows that vertices on the opposite sides of a cross-boundary connection have opposite corresponding link-type values (1 and -1).

3.2.3   Time evolution

Movement of vertices in the domain is restricted to motion towards one of the neighboring vertices, that is along triangle sides. When a vertex crosses a domain boundary it

reappears on the opposite side, with its link type arrays and link type arrays of vertices connected to it updated accordingly. We apply two kinds of motion schemes: random motion and cell-competition. Moreover, each scheme has two different versions of vertex movement: constant velocity and constant acceleration. We label them shortly *CA*, *CV*, *RA* and *RV* for cell competition constant acceleration, cell competition constant velocity, random walk constant acceleration and random walk constant velocity, respectively. The *RV* algorithm is as follows: for each vertex a neighbor is chosen randomly and the vertex is moved towards that neighbor by a random displacement δ (a uniformly distributed random number between 0 and 0.28, the domain size is 12×12). For the *CV* scheme, the vertex is moved towards its closest neighbor by a constant displacement ($\delta = 0.05$). If the step is larger than the distance between the vertex and the neighbor towards which it is being moved, we merge the vertices (see Section 3.2.4 for vertex merging process description). In case of constant acceleration schemes, the movement of a vertex in each timestep is the projection of a vector sum of all previous displacements of the vertex on the triangle side along which the vertex is moved plus δ (which is the same as in constant velocity case for corresponding models). To prevent "cell flipping", which happens when a vertex crosses a connection between two other vertices (thus destroying the triangular topology), we introduce the following scheme, illustrated in Fig. 3.2. For each vertex
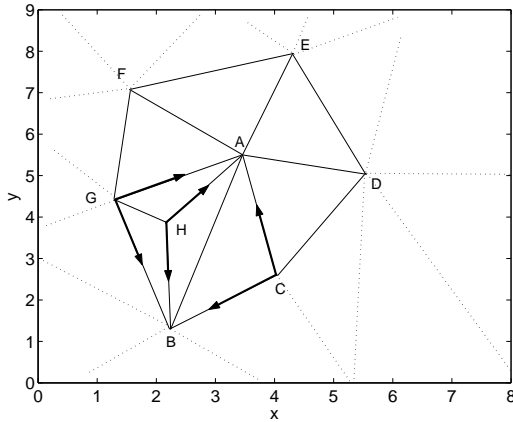
Figure 3.2: Illustration of the procedure preventing cell-flipping. For details see text.

in the domain that is being moved (*A*) we find all its neighbors, i.e. all other vertices connected to it (*B* - *H*). Next, for each neighbor (illustrated in the case of vertex *B* in Fig. 3.2) we find all vertices connected both to the moving vertex (*A*) and the neighbor (*B*), and for each of them we calculate the cross products of the pair of vectors pointing towards vertices *A* and *B*, respectively (shown as black thick arrows). Then we calculate the corresponding cross products with the position of vertex *A* after its displacement and determine the product of both. If for any of the vertices this value is negative, i.e.

the angle between both vectors has changed sign, or the post-movement cross product is zero, then we cancel the movement of A for this timestep. In this case, for the constant acceleration schemes we also reset the sum of all previous displacements of the vertex to zero, otherwise those models have a tendency to "freeze" after some time, with only a few vertices actually moving.

3.2.4   Cell vanishing - vertex merging

In order to allow for vanishing of cells, we have to define a procedure and criteria for the merging of vertices. After a vertex has moved towards one of its neighbors, the distance between them is measured. If it is below a critical value Δ (free parameter, unless stated otherwise $\Delta = 8 \cdot 10^{-5}$; the domain size is 12×12), the vertices are merged so that one of the vertices and all the associated array structures vanish and are removed form the data structure. For all common neighbors of the merging vertices, the reference to the disappearing one in the link and other arrays is removed. For all other vertices connected to the disappearing vertex, its reference in the associated link arrays is changed to the remaining, "merged" vertex. In "pathological" cases, as illustrated in Fig. 3.3, when the merging vertices (A and B) have more than two common neighbors (C - E), we have to remove all vertices which are connected to only one other vertex besides A and B (in this case, vertex D). Otherwise, vertices like D would be connected to only two vertices after A and B had merged, thus breaking the triangular topology. As the age of vertices and
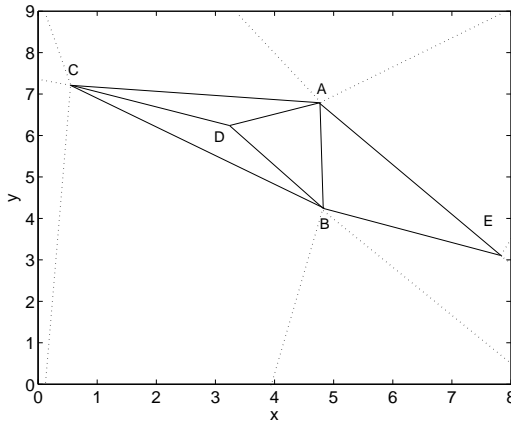
Figure 3.3: "Pathological" case of a vertex merger. For details see text.

lanes (connections) in the model is used to detect mesogranulation in a way similar to the cork method applied in observations and simulations, it is important to define the age inheritance rules properly. Corks are artificial particles which are advected passively on a horizontal plane by the velocity field. They tend to accumulate in downflow regions

i.e. downflow lanes and vertices separating granules (Cattaneo et al. 2001, Rieutord et al. 2000, Roudier et al. 2003, Ploner et al. 2000). We postulate a relation between the number of corks accumulated in a downflow structure and its age: the older the structure the more corks it is likely to attract. It follows that when two lanes or vertices merge, the corks naturally remain in the merged lane or vertex. Hence, when two vertices A and B merge (Fig. 3.3), we keep the older age of the connections A-E and B-E as the age of the new connection of the merged vertex with E, and similarly for C. The age of the merged vertex is also the older age of vertices A and B. The merged vertex inherits the neighbors of both A and B (with link and age arrays updated accordingly). We do not allow vertices to have multiple references to another vertex (a link array has to have unique entries); therefore, the domain has to be bigger than 3×3 vertices. This also leads to errors in case of "domain collapse", when merging of vertices produces a few giant cells and vertices from opposing ends of domain become connected also through the domain. Such case is neither interesting nor sought for, and with proper cell splitting rules it never occurs.

3.2.5   Cell splitting - vertex appearance

Since the construction of the two-dimensional model allows for many different schemes for cell splitting, it is reasonable to investigate what differences those schemes produce, both in the granulation characteristics, as well as in the emerging mesogranulation features. Hence, we apply four different cell splitting schemes: critical cell side length, critical cell area, critical cell area plus the longest side, and random splitting. We label them L, A, AL and R, respectively. Thus, a cell-competition constant acceleration model with random splitting is labelled CA/R etc.

3.2.5.1   Critical cell side length (L)

When a connection between two vertices A and B (see Fig. 3.4) exceeds a critical length (an uniformly distributed random number between 2 and 3.5, evaluated individually for each connection in each timestep; the box size is 12×12), the following splitting procedure is initiated: first, two unitary vectors $\vec{e_1}$, $\vec{e_2}$ perpendicular to $\overrightarrow{AB}$ are determined (thick arrows). Next, the common neighbor of A and B with the smallest $\mathcal{L}_{\mathcal{AB}}$ (sum of distances to A and B) is found (C in Fig. 3.4). Knowing the dot product of $\overrightarrow{AC}$ with $\vec{e_1}$ and $\vec{e_2}$, we use the dot product of the connections to the remaining common neighbors (i.e. vectors $\overrightarrow{AE}$, $\overrightarrow{AF}$, $\overrightarrow{AD}$ in Fig. 3.4) with vectors $\vec{e_1}$, $\vec{e_2}$ and minimize $\mathcal{L}_{\mathcal{AB}}$ to determine the closest common neighbor of A and B on the opposite side of $\overrightarrow{AB}$ that vertex C is (vertex D in Fig. 3.4). The new vertex X is inserted halfway between vertices A and B, splitting both triangles that share the side $[A,B]$. The link array associated with X has four entries, namely A, B, C and D. Since the appearance procedure is initiated in the code after the displacement loop but before the periodic-boundary check, the new vertex can be techni-cally treated as laying within the domain. If it is positioned outside domain boundaries, the periodic-boundary code will update all the associated arrays. Therefore the link-type array of X consists of zero for A, and the same link-type value for B, C and D as vertex A has for those vertices. Link array of A (B) is updated with the number of X in place of B (A). The link-type arrays of A are updated with zeros for X. The link arrays of C and D are extended by one position for the number of X. All other arrays of A, B, C and D are
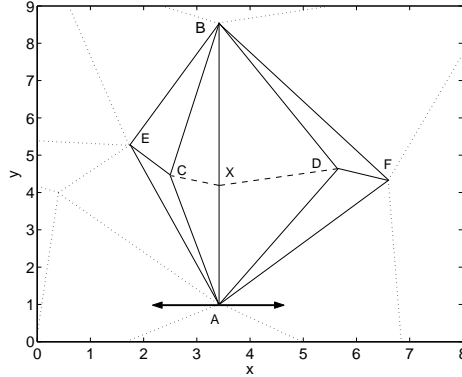
Figure 3.4: Illustration of the splitting process, with new vertex *X* appearing between vertices *A* and *B*. Dashed lines are the new connections appearing.

adjusted accordingly (link-type, age etc.) Since the connections of the new vertex *X* to *A* and *B* inherit the age of the former *A-B* connection, the only new structures appearing are the connections *X-C*, *X-D* and the vertex *X*.

3.2.5.2   Critical cell area (A)

In this scheme the cell is split when it exceeds a critical area value (a uniformly distributed random number between 1.5 and 2.5; the box size is 12×12). The splitting partner cell is chosen to be the neighbor with the largest area. The rules of new vertex position and age inheritance of new structures are like in the "critical side length" splitting case.

3.2.5.3   Critical cell area plus the longest side (AL)

The cell is split when it exceeds a critical area value, and the splitting occurs through the longest side of the cell (in Fig. 3.4 the "splitting connection" *A-B* is chosen to be the longest side of the cell), regardless of the area of the neighbor sharing the side with the cell. The rules of new vertex position and age inheritance of new structures are like in the "critical side length" splitting case.

3.2.5.4   Random splitting (R)

In this scheme the splitting is not based on any cell characteristics. Therefore, to keep the number of cells present in the domain constant throughout the simulation, the number of the splitting events in each timestep is equal to the number of vanishing events that took place in this timestep. The cell that is split is chosen randomly (each cell having the same probability of being chosen), as well as the side through which the splitting occurs. The

rules of new vertex position and age inheritance of new structures are like in the "critical side length" splitting case.

3.3   Granule properties

In this section we present the statistics of granulation cell size and lifetime distributions for selected versions of the two-dimensional model. The statistics for the remaining model versions can be found in the Appendix. The lifetime of a cell is the time (in timesteps) from its birth by parent-cell splitting to its demise (either by splitting or by vanishing). The size of a cell is taken as the average size over the cell's lifetime (sum of size in each timestep divided by the number of timesteps). We present statistics for two kinds of cells, distinguished by the way the disappear in the simulation: dissolvers (those who vanish by vertex merging) and fragmenters (those that split). For each model, four figures are shown: lifetime distribution, size distribution, scatter plot of the cell size versus lifetime and a domain snapshot. The lifetime of granules is normalized with the average granule lifetime for the given model.

The reported lifetime and area histograms of solar granules are close to exponential (Title et al. 1989, Brandt et al. 1991, Hirzberger et al. 1996, 1997, 1999, Müller et al. 2001). A similar behavior in the cellular model can be seen in the random-walk and the random splitting versions. In other model versions the distributions tend to peak around a certain value, and the small short-lived cells are not the most abundant ones. On the other hand, we find that the granule characteristics of the cell-competition models agree better with those obtained from a two-dimensional hydrodynamical simulation (Ploner 1998, PhD thesis) than their random-walk counterparts, which was the case in the one-dimensional model as well. The main difference between the two schemes is, similarly to the one-dimensional case, the statistical separation of the dissolver and fragmenter sizes. Hence, while the cell-competition model versions reproduce the statistical separation between the dissolvers and fragmenters better than the random-walk versions, they do not produce the cascade of very small, short-lived cells. The opposite is true for the random-walk model versions. Naturally, one should not expect the cellular model to perfectly reproduce the properties of real granules. Additionally, since the solar granule analysis methods involve algorithms with a somewhat arbitrary detection level threshold, while in the cellular model we are able to extract the exact properties of each triangle, the comparison between the two becomes difficult. It is important to stress again that the fundamental aim of the cellular model is not the perfect reproduction of the properties of solar granulation. Rather, it serves to verify how much the emerging mesogranular properties depend on the detailed granule interaction rules.

The existence of very small fragmenters in the models in which the splitting criterion is based on the cell size (i.e. X/A and X/AL) can be understood when one remembers that the splitting always affects two neighboring triangular cells. The fragmentation procedure is initiated when a given cell exceeds the critical area, but the splitting partner can be of any size. In the X/L versions, it is the cell side length that determines whether a cell splits or not, therefore it may happen that one or even both splitting cells have small area. In the random splitting models there is no criterion for splitting, hence there is almost no difference in sizes between dissolvers and fragmenters. The fact that in those models

fragmenters are statistically still a bit larger is due to the fact that the majority of cells that end as dissolvers are the initially small cells. The vertices of such cells are closer to each other, hence it takes less time for the random walk process to bring those vertices together (the distance covered by a random walk process scales as $\sqrt{t}$, t being time). Hence, a cell that is initially larger persists on average longer, and therefore is more probable to become a fragmenter.
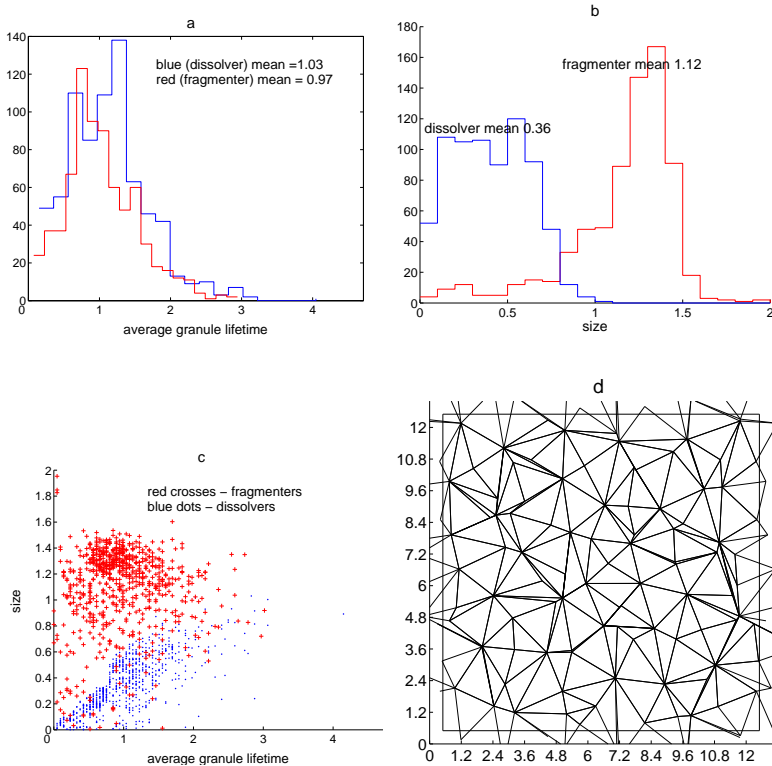
Figure 3.5: (a) cell lifetime and (b) cell size distributions, (c) scatter plot of size versus lifetime and (d) domain snapshot; *CV/AL* version.
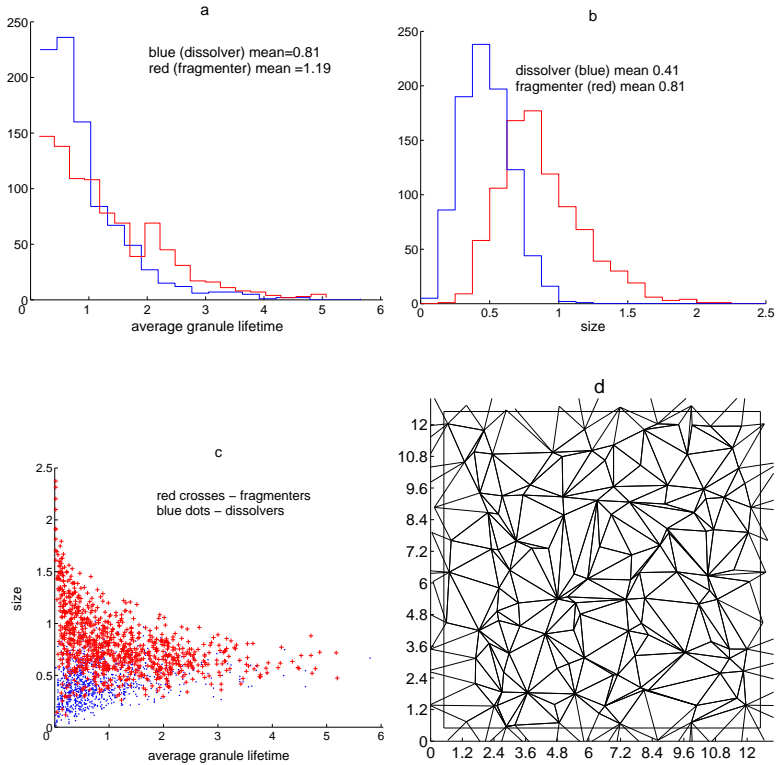
Figure 3.6: (a) cell lifetime and (b) cell size distributions, (c) scatter plot of size versus lifetime and (d) domain snapshot; *RV/AL* version.
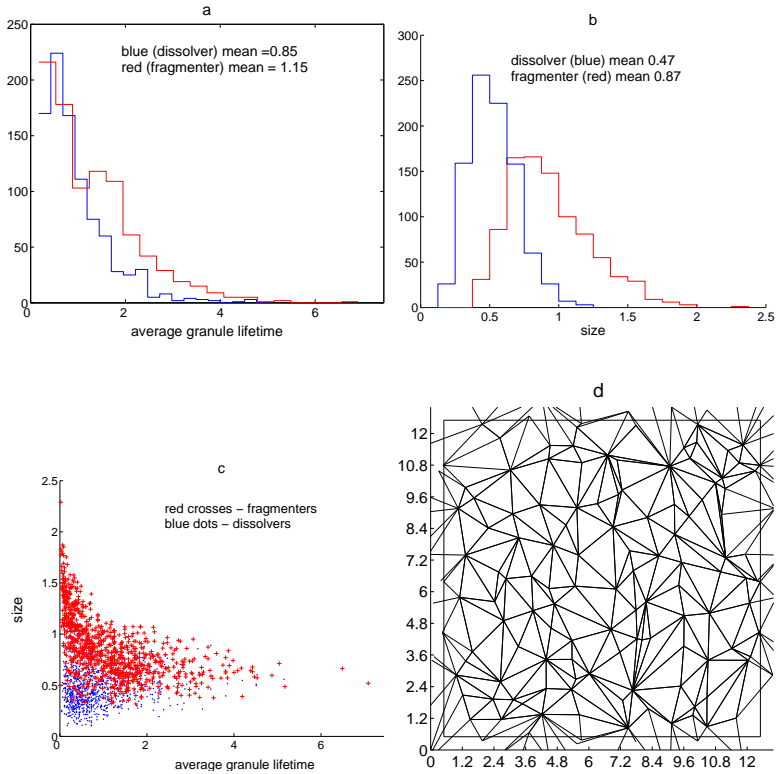
Figure 3.7: (a) cell lifetime and (b) cell size distributions, (c) scatter plot of size versus lifetime and (d) domain snapshot; *RV/A* version.
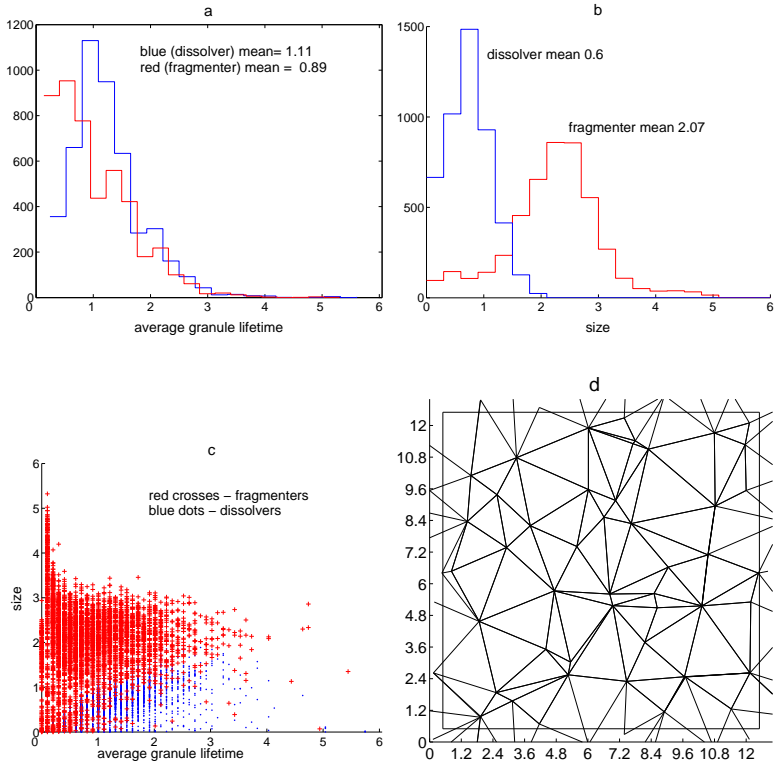
Figure 3.8: (a) cell lifetime and (b) cell size distributions, (c) scatter plot of size versus lifetime and (d) domain snapshot; *CA/L* version.
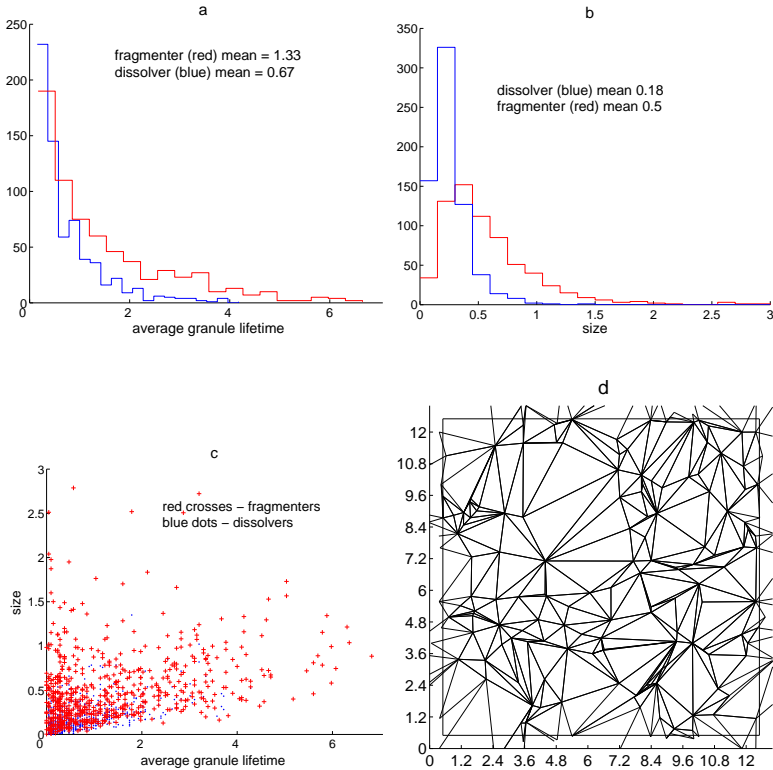
Figure 3.9: (a) cell lifetime and (b) cell size distributions, (c) scatter plot of size versus lifetime and (d) domain snapshot; *RV/R* version.

When examining the cell characteristics it is apparent that some model versions produce patterns which are less desirable than others when approximating granulation (see domain snapshots for the *CV/A*, *CA/A* and *RA/R* versions in the Appendix for example). The constant acceleration versions differ only marginally from the constant velocity ones, hence it is not necessary to include both for the same splitting scheme in further analysis. Therefore we retain only the *CV/AL*, *RV/AL*, *RV/A*, *RV/R* and *CA/L* models for mesogranulation investigation.

3.4 Mesogranulation: definition

Solar mesogranulation was originally detected as a pattern in the vertical velocity (November 1981). Since the upflowing plasma diverges horizontally upon reaching the surface, there exists a close correspondence between the upflow and outflow regions on the solar surface, which may also be used to detect and analyze mesogranules (Simon et al. 1991, Ploner et al. 2000, Rieutord et al. 2000, Roudier et al. 2003, Cattaneo et al. 2001). As discussed in the previous sections, the cork pattern outlines horizontal velocity divergence areas, thus providing another way to visualize mesogranulation. The construction of the model presented in this chapter is a two-dimensional extension of the one-dimensional model concept of Chapter 2, with the age of the vertices and intergranular lanes being a measure of the number of corks they would accumulate. The idea is the following: the corks tend to gather in the long-lived intergranular lanes, which mark places of horizontal velocity convergence (downflows). These structures have lifetimes much longer than average granule lifetime and outline areas of horizontal fluid divergence which are suggested to represent mesogranules. Therefore, we argue that an intergranular lane that lives long enough will accumulate enough corks to become a mesogranular border-lane. Hence, one method of the mesogranulation detection in the model is based on the age of the intergranular structures. Additionally, in the two-dimensional model we can readily apply the methods used in the analysis of observations and HD simulations to obtain the horizontal velocity field and find mesogranules directly as the velocity divergence areas.

3.4.1 Intergranular lane age

As explained in Section 3.2.4, the rules for the age determination of lanes and vertices in the model are constructed in a way that corresponds to the cork method of mesogranulation detection used in observations and simulations. Therefore, once a given structure (vertex or connecting lane) gets older than a given time t_0 (a free parameter), it is marked as "mesogranular". The time in the models is scaled with the average granule lifetime. In the following figures mesostructures are marked as thick and red in contrast to blue granulation features. Figure. 3.10 and Fig. 3.11 show snapshots from the *CV/AL* and *RV/AL* model versions, respectively. The mesogranulation evolution time t_0 equals $10 \cdot \tau_{av}$ (τ_{av} is the average granule lifetime) in each case. The main difference between the red (mesogranular) patterns in Figures 3.10 and 3.11 is that in the *CV/AL* model (Fig. 3.10) the structure seems to be more uniformly spaced. One measure of the regularity of the pattern is the width of the distribution divided by the mean value of the distances between the closest mesovertices (the red dots in the figures). Figure 3.12 shows the histograms of such distances for the chosen models, while Table 3.1 contains the values of the standard deviation divided by the mean of the distributions. Table 3.1 along with Fig 3.12 suggest

Table 3.1: Values of the standard deviation divided by the mean value for the mesovertex distance distributions from Fig. 3.12

Model version	CV/AL	RV/AL	RV/A	RV/R	CA/L
(Std.deviation)/mean	0.5	0.97	0.86	1.05	0.66
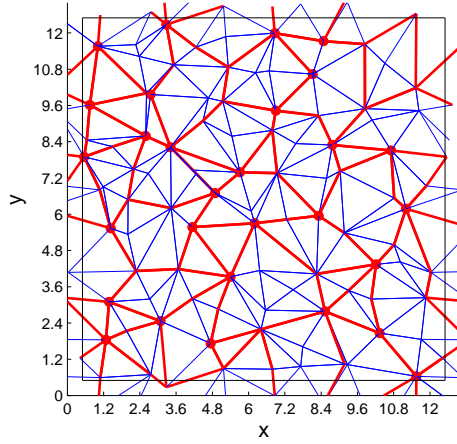
Figure 3.10: Snapshot from a *CV/AL* model version. Mesostructures corresponding to 10 average granule lifetime evolution time are marked in red.
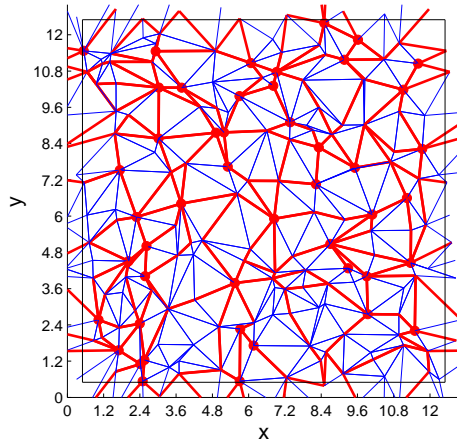
Figure 3.11: Same as Fig. 3.10, but for *RV/AL* model version.

that the cell-competition models produce the most uniformly spaced mesovertex pattern, while the largest spread is found for the random models. Naturally, the histogram of distances between the closest mesovertices only tell us how uniformly they are distributed
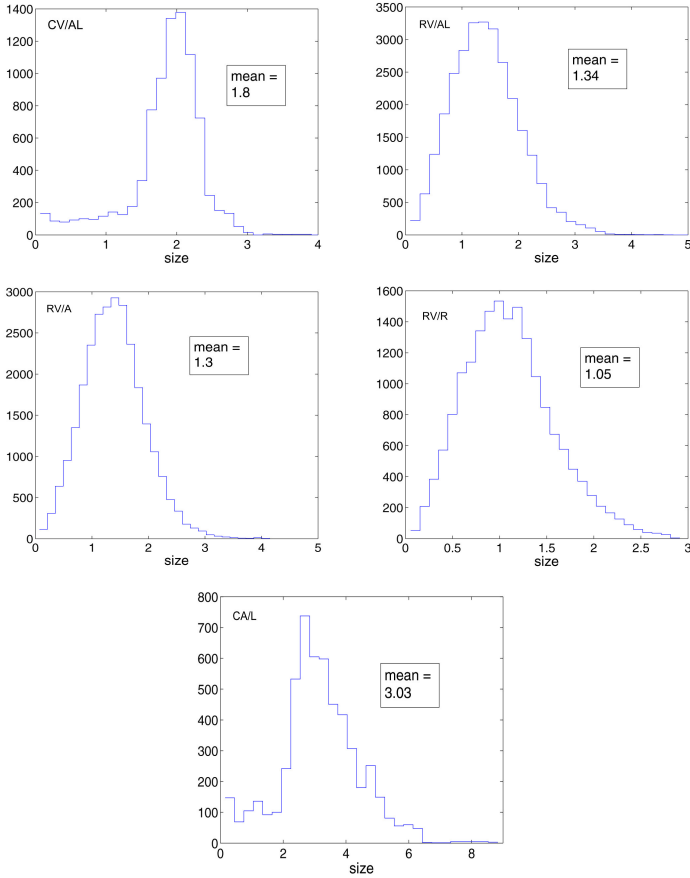
Figure 3.12: Histogram of the distances between the closest mesovertices in the different model versions.

on the surface, and does not necessarily reflect on the properties of mesogranular cells. These are defined as the area confined by the mesolanes and there is no simple relation between mesovertices and mesogranular cells. The analysis of the mesogranulation size and lifetime characteristics follows in Section 3.5.

51

3.4.2 Horizontal velocity divergence areas

A different way of detecting mesogranulation in the model is to analyze the horizontal velocity divergence field. In this method patches of velocity divergence are associated with the mesogranular flow, the size and lifetime of the patches characterizing the temporal and spatial scales. In the case of observations, the horizontal velocity field is usually obtained with a Local Correlation Tracking (LCT) algorithm, which is based on tracking brightness patterns throughout the domain (November et al. 1988, Berger et al. 1998, Welsch et al. 2004). In our model we apply two methods of obtaining the horizontal velocity field: direct cell tracking, and a LCT algorithm analogous to that applied in observational data analysis.

3.4.2.1 Cell tracking

The cell tracking methods takes advantage of the fact that in the cell model we explicitly know the position of each vertex constituting a triangular cell. This allows us to track the cell's movement, which is done in the following way: in each timestep we record the position of each cell's geometrical center. The translation of this point from one timestep to the next is taken as the horizontal velocity vector; all such vectors are stored for all cells throughout the simulation. Next, we divide the domain into a number of square bins. The velocity vectors lying within one bin during a chosen time interval (called the averaging time) are added up to produce a temporally and spatially averaged velocity vector, which is then assigned to the bin center. The default number of bins is 15×15, which was found to be optimal. If the number of bins is too large, many of them contain no velocity vectors at all. Too few bins, on the other hand, can average out the interesting velocity variations. The averaging time interval is chosen to be the mesogranulation threshold time t_0 used for the lane-age method, so that the resulting velocity divergence field can be compared with the intergranular mesolane pattern present in the domain at a given timestep. The divergence of the velocity is calculated using the velocity vectors from four neighboring bins as illustrated in Fig. 3.13. The formula is as follows:

$$\nabla \cdot \overrightarrow{V_H} = \frac{(V_{xD} - V_{xB}) + (V_{xC} - V_{xA})}{2d} + \frac{(V_{yD} - V_{yC}) + (V_{yB} - V_{yA})}{2d} \qquad (3.1)$$

with V_{xi} and V_{yi} being the x and y velocity components at the point i, and d being the bin length. The velocity divergence value is assigned to the point X, which is the common vertex of the bins used for calculation. Fig. 3.14 and Fig. 3.15 show the division of the domain into bins and an example of the resulting velocity divergence field for a CV/AL model. In Fig. 3.15 the mesogranulation averaging time t_0 is $7.5 \cdot \tau_{av}$, where τ_{av} is the average cell lifetime ($7.5 \cdot \tau_{av}$ is roughly one hour if $\tau_{av} = 8$ min is taken from solar observation). White lanes are the mesolanes (intergranular lanes older than $t_0 = 7.5 \cdot \tau_{av}$).
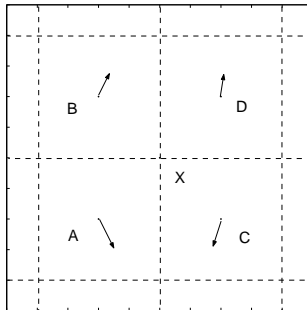
Figure 3.13: Illustration of the velocity divergence calculation procedure.
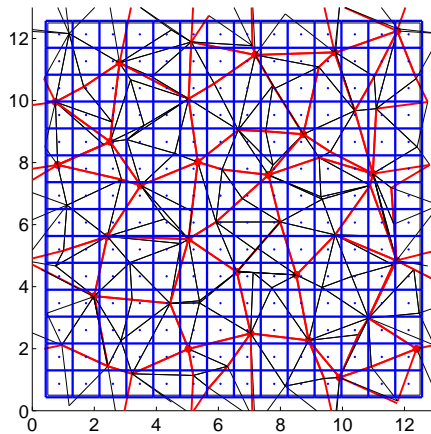
Figure 3.14: Example of domain bin division for velocity divergence calculation (see text).
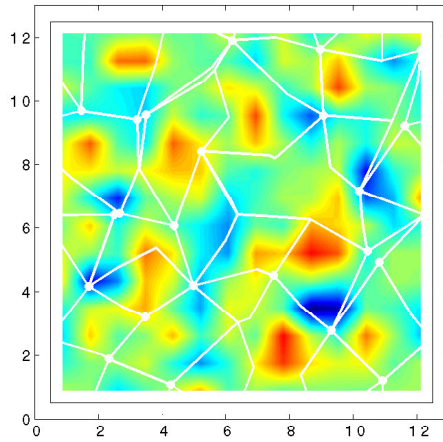
Figure 3.15: Example of a velocity divergence map for a *CV/AL* model. $t_0 = 7.5 \cdot \tau_{av}$. Blue color indicates convergence while red signifies divergence. Overplotted in white are the mesolanes determined by the lane age criterion with the same value of t_0. The divergence areas correspond well with the mesogranules defined by mesolanes.

3.4.2.2   Local Correlation Tracking

We use a public LCT algorithm developed and described by Welsh et al. (2004). The code computes the horizontal velocity field by tracking granule motions in the domain using a Fourier-transform based cross correlation function of subsequent intensity patterns. We apply the LCT algorithm to timeseries of granulation intensity images, which are images like the one in Fig. 3.1, to which a shading algorithm (Eq. 3.2) had been applied. The timeseries are $100 \cdot \tau_{av}$ to $150 \cdot \tau_{av}$ long, depending on the model. The LCT window is a gaussian, with the full width at half maximum set to the average granule size. The resulting velocity field agrees well with the cell tracking method velocities described in the previous section. Figure. 3.16 presents an example of the velocity divergence field for the *CV/AL* model acquired with the cell tracking method and with the LCT algorithm, respectively. Averaging time is $7.5 \cdot \tau_{av}$. One can see a clear correspondence of divergence and convergence areas for the both methods in Figure 3.16.
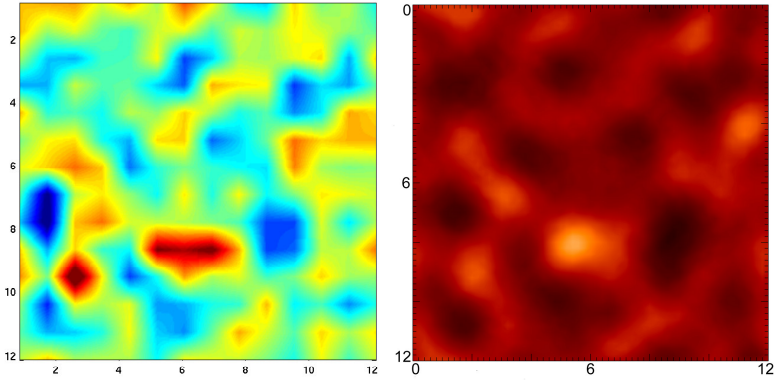
Figure 3.16: Velocity divergence field for the *CV/AL* model; comparison between the cell tracking (left) and LCT methods (right) of acquiring the velocity.

3.4.3   Velocity divergence patches versus mesolanes: comparison

Given the two methods of defining mesogranulation in the model, it is interesting to see how the mesofeatures emerging from both methods relate to each other. The intergranular lane age method is constructed to correspond to the cork advection method, while corks are used in data analysis to outline areas of velocity divergence. Hence, we can verify whether the mesolanes determined by the lane-age method at a given time actually outline the corresponding divergence patches obtained from the t_0-averaged horizontal velocity. This is done in two ways: by calculating the cross-correlation function between the mesolane features and the velocity convergence areas present at a given time in the model,

and by actually advecting cork particles with the LCT-obtained velocities and comparing their resulting positions with the mesolanes.

In order to calculate the cross correlation function (the cross correlation coefficient as a function of the relative shift of the images), the divergence and the mesolane images need to be of a correct form (grayscale intensity). Figure 3.17 shows an example of such images used for cross correlation calculation. The mesolane image (Fig. 3.17, right
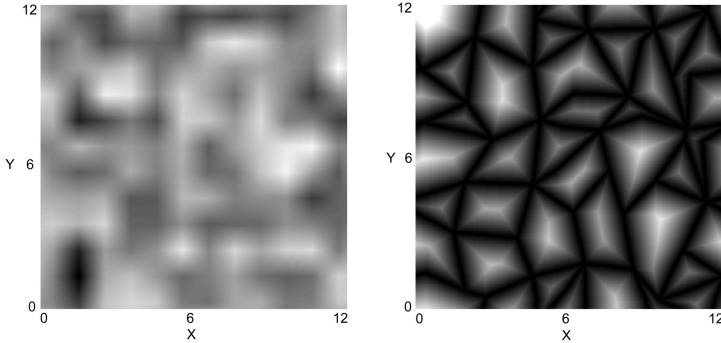
Figure 3.17: Example of a velocity divergence image (left) and a corresponding mesofeature image (right), *CA/AL* model.

panel) is produced from images like the one in Fig. 3.10 with an algorithm that records the positions of red features (mesofeatures) in the image and then transforms them into a grayscale intensity image. It works in the following way: first, all features in the image except the mesolanes are removed and the color of the mesolanes is changed to black. Next, we assign to each pixel $I(i, j)$ in the image matrix I which is not black (i.e is not a mesolane) a following brightness value:

$$I(i, j) = \min[\min(I(i + 1, j), I(i - 1, j)) + A, \ \min(I(i, j - 1), I(i, j + 1)) + A] \quad (3.2)$$

where min(a,b) signifies the lower value of the numbers a and b. The parameter A controls the gradient of the shading, the larger the value the higher the gradient. In case of Fig. 3.17 (b) $A = 3$. We run the above algorithm for i and j increasing from minimum to maximum value as well as for i and j decreasing from maximum to minimum to achieve symmetric shading. Both the maximum and minimum pixel numbers i and j lie well within the image matrix $I(i, j)$, so that there are no problems with the initial values $I(i - 1, j)$ etc. The image matrix $I(i, j)$ is much larger than the resulting shaded image and has values of 255 ("white") everywhere except mesolanes. Figure. 3.17 (left) is the velocity divergence plotted in a grayscale colormap. The horizontal and vertical pattern seen in the divergence image is a consequence of a linear data interpolation algorithm applied.

To reduce the noise, the cross correlation function between the velocity divergence and the mesolane images was averaged over 63 independent runs for each version of the

model: at the end of each run, the correlation function between the two corresponding images (like those in Fig. 3.17) was calculated and then a mean of 63 cross correlation functions was produced. Fig. 3.18 shows the averaged cross correlation function for the
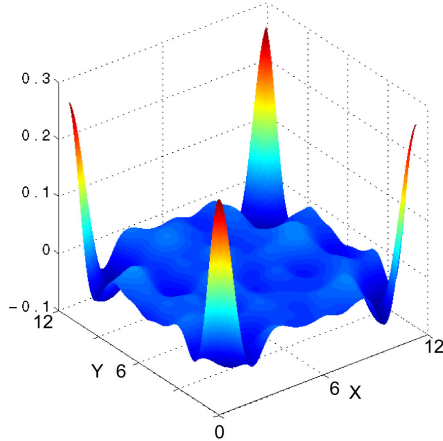
Figure 3.18: Averaged cross correlation function between velocity divergence and mesolanes for the *CV/AL* model. $t_0 = 7.5 \cdot \tau_{\mathrm{av}}$.
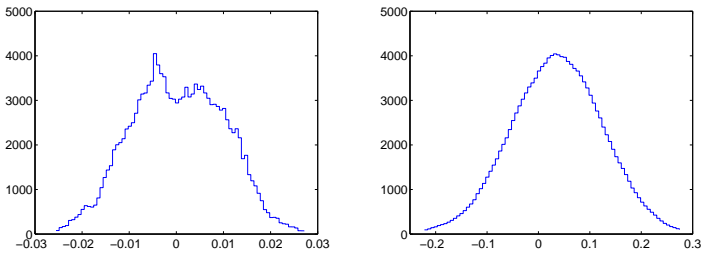
Figure 3.19: (left) histogram of an average of the 63 correlation functions between velocity divergence and mesolanes, (right) histogram of an average of the 63 correlation function histograms *CV/AL* model (see text).

CV/AL model, $t_0 = 7.5 \cdot \tau_{\mathrm{av}}$. To estimate the significance of the peak of the cross correlation function in Fig. 3.18, we calculate 63 correlations of image pairs like in Fig. 3.17 but
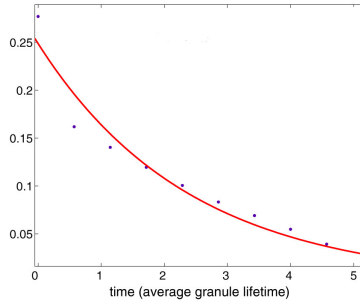
Figure 3.20: Decrease of correlation between velocity divergence and mesolanes with the velocity divergence averaging time. The curve is an exponential fit, *CV/AL* model. The e-folding time is $2.4 \cdot \tau_{av}$

with the velocity divergence image coming from a different dataset than the mesolane image (hence unrelated). Next, we average those 63 correlations of unrelated images in two different ways to produce two histograms: a histogram of an average of the 63 correlation functions, and a histogram of an average of the 63 correlation function histograms. Figure. 3.19 shows both histograms, it follows that the correlation value of 0.27 is significant at best at the 2σ level and there is correlation between velocity divergence and mesolanes in the *CV/AL* model.

It is instructive to study how the cross correlation between velocity divergence structures and mesolanes decreases with evolution time. We take a given mesolane intensity image and vary the time over which the velocity divergence was averaged to produce the divergence image. For each velocity divergence averaging time, 63 independent model runs are included to produce an averaged cross correlation function as in Fig. 3.18. Figure. 3.20 shows the decrease of correlation with the velocity divergence averaging time for the *CV/AL* model. On the x axis is the time subtracted from the end of the full $7.5 \cdot \tau_{av}$ of evolution (0 means that the velocity divergence was averaged over full $7.5 \cdot \tau_{av}$, 1 means the velocity divergence was averaged over the first $6 \cdot \tau_{av}$ only, and so on). The correlation decrease in Fig. 3.20 is not quite exponential, but the fit provides some idea about the timescale. The rather short e-folding time $2.4 \cdot \tau_{av}$ means that the mesolane positions are determined mostly by the most recent velocity field and are advected over the surface and change their spatial position more than the velocity divergence patches. Alternatively, the longer the velocity divergence averaging time, the more of the small-scale noise is removed from the divergence images, leaving only the large patches that are well correlated with the mesolanes.

The close to exponential form of the correlation decrease in Fig. 3.20 can be understood when we consider a following example: suppose we have two gaussians $f_1 = A_1 e^{-x^2}$ and $f_2 = A_2 e^{-(x-\delta(t))^2}$, whose spatial separation $\delta(t)$ is a function of time in a form $\delta(t) =$

$a \sqrt{t}$. Calculation their convolution yields:

$$(f_1 * f_2)(x) = \int_x e^{-x^2} e^{-(x-\delta(t))^2} dx = \int_x e^{-2x^2} e^{-2x\delta(t)} e^{-\delta(t)^2} dx = e^{-a^2 t} \int_x e^{-2x^2} e^{-2x\delta(t)} dx \quad (3.3)$$

Therefore, the signal F_t of such drifting gaussians is exponential in time:

$$F_t = \int_t e^{-a^2 t} \int_x e^{-2x^2} e^{-2x\delta(t)} dx dt = -a^{-2} e^{-a^2 t} \int_x e^{-2x^2} e^{-2x\delta(t)} dx \qquad (3.4)$$

The same conclusions are true for the other versions of the model, there is a significant correlation between the horizontal velocity convergence areas and mesolanes for $t_0 = 7.5 \cdot \tau_{av}$ (one hour) and the decrease of this correlation (like in Fig. 3.20) is quite fast. The equivalents of Fig. 3.18 to 3.20 for those models can be found in the Appendix.

The velocity field obtained by tracking the granules also allows for cork advection analysis. Once the cork results are obtained, we can overplot their final position (position after evolving for the time equivalent to the mesolane minimum age) on the corresponding mesolane image to verify if their positions match. We start with a dense uniform distribution of corks, no additional corks are introduced during the advection process. The cork evolution time equals $t_0 = 7.5 \cdot \tau_{av}$ (equal to the mesolane minimum age, ~1 hour). Figure. 3.21 presents corks position overplotted on the corresponding velocity divergence field for the *CV/AL*, *RV/AL* and *RV/R* models, respectively. The corks accumulate in velocity convergence regions, while being pushed out of the divergence areas. The velocities are larger in the random models owing to the nature of random motion: the path of a vertex integrated over a granule lifetime in a random model is longer than in a cell-competition model, therefore the calculated velocity is also larger. This explains why the corks travel a longer distance in the random models. This also explains why in the random models the corks in some places are not as well aligned with the convergence areas as in the cell-competition models. The cork positions are strongly influenced by the last few timesteps, which can push the corks significantly, while the velocity divergence field will not be so strongly affected. Looking at the images in Fig. 3.21 it is instructive to notice that the structure of the divergence field evolves from a larger, seemingly regular cell-like pattern in the *CV/AL* case, to more chaotic small-scale pattern in the most random case of *RV/R*. Since the observed solar mesogranulation images (velocity divergence) are most similar to the *CV/AL* case, this fact favors the cell-competition granule interaction rules as a better description of the real granule interactions than the random walk model.

To study how the cork pattern relates to the corresponding mesolane positions, we present two kinds of pictures: one is the corks overplotted on a single mesolane image taken at the last timestep of the $7.5 \cdot \tau_{av}$ cork evolution time. The other is corks overplotted on the mesolane positions averaged over the whole $7.5 \cdot \tau_{av}$ of the cork evolution time. Figures 3.22-3.24 present the images for the *CV/AL*, *RV/AL* and *RV/R* models, respectively. In both types of images the corks tend to accumulate away form the bright regions (mesogranule centers). Visual inspection of Fig. 3.22-3.24 indicates that the corks are better aligned with the most recent position of the mesolanes rather than with their t_0-averaged locations. This is not surprising since the definition of mesolanes corresponds to the cork convergence areas. Nevertheless, the correspondence of corks and mesolane positions in both types of images is far from perfect and there is no one-to-one relation between these structures. Figure. 3.21-3.24 help to realize that the mesogranules defined

by the lane age differ from those defined by the velocity divergence field. This is also seen in Fig. 3.15, where the white mesolanes are overplotted on the corresponding velocity divergence field. Even though a significant correlation between the mesolanes and convergence regions (i.e. downflows) exists, it is apparent that the shape, size and position of mesogranules defined by the both methods differ. The mesolane pattern changes more rapidly due to the arbitrary age condition, which leads to an abrupt "on-off" behavior which is not present in the divergence field. The position of the mesolanes in the last mesolane image in a t_0 timeseries is a good approximation of the position of the t_0-old corks, as seen in Figures 3.22-3.24. Nevertheless, since the LCT-obtained velocity divergence method is the same as used in observations to define mesogranules, it is a more relevant way to analyze mesogranulation in the model. The intergranular lane age method results depend more directly on the construction details of the model (triangular topology, age inheritance rules etc.), and hence are more likely to reflect the properties of this model only.
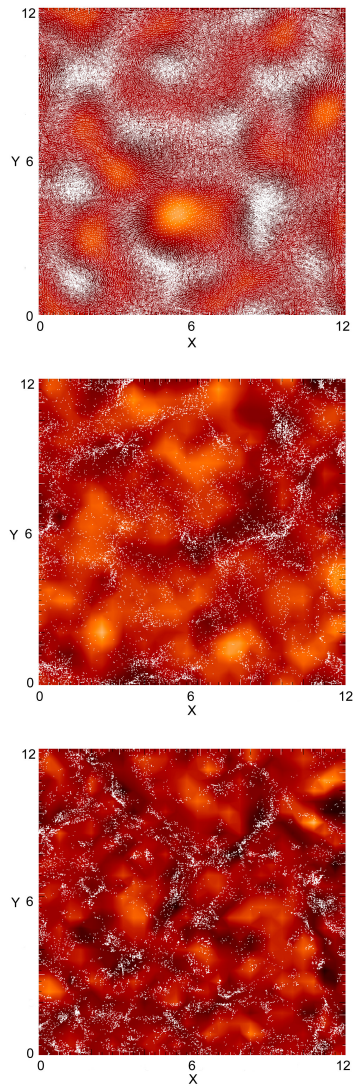
Figure 3.21: Cork positions overplotted on the corresponding time-averaged velocity divergence field, *CV/AL* (top), *RV/AL* (middle) and *RV/R* (bottom) models.
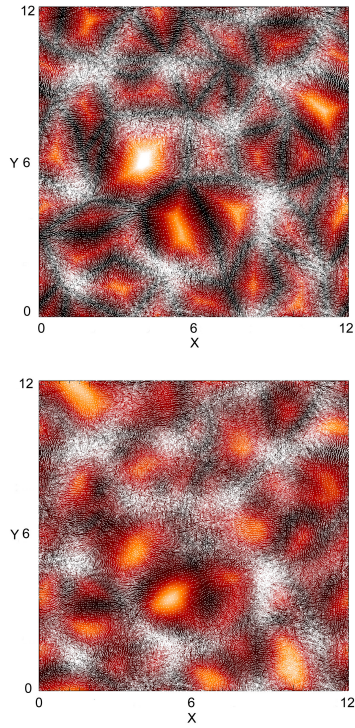
Figure 3.22: Cork positions overplotted on the last mesolane image (top) and a time-averaged mesolane image (bottom) , *CV/AL* model.
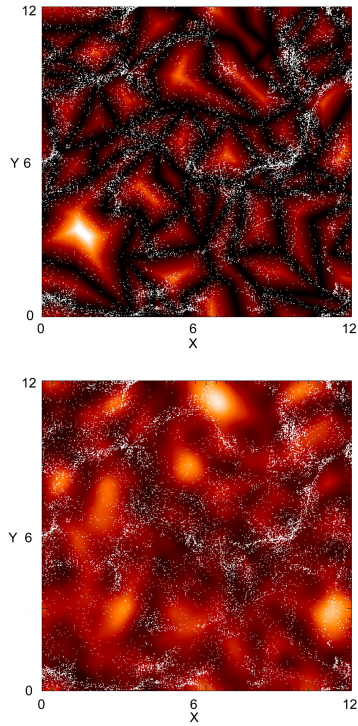
Figure 3.23: Cork positions overplotted on the last mesolane image (top) and a time-averaged mesolane image (bottom) , *RV/AL* model.
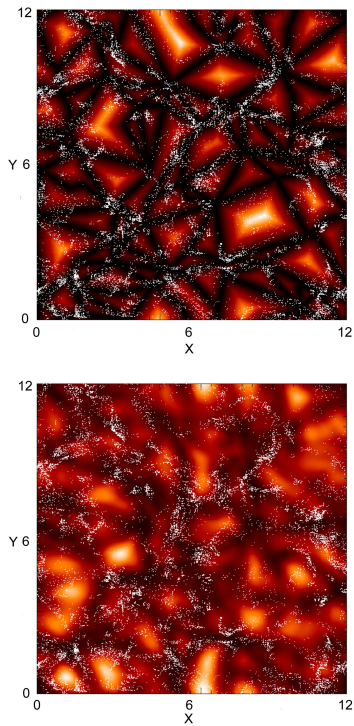
Figure 3.24: Cork positions overplotted on the last mesolane image (top) and a time-averaged mesolane image (bottom) , *RV/R* model.

3.5   Mesogranulation: results

This section presents the statistical results of mesogranule areas and lifetimes extracted from the model by the two methods described in the previous sections. One method defines mesogranules as regions confined by the mesolanes, while the other as horizontal velocity divergence patches. In both methods, the analysis consists of uniquely identifying the mesogranules in a timeseries of images. In the intergranular age method we obtain the mesogranule properties by tracking the cells in time. Hence we are able to directly extract the mesogranule lifetimes and areas, the latter defined as the average area over cell's lifetime. In case of the velocity divergence method we include two types of results: the tracking and snapshot statistics. The tracking method is analogous to the mesolane tracking method. In the snapshot statistics we consider statistically independent velocity divergence images and extract the area properties of mesogranules from each image individually. The lifetime information is then obtained by calculating the cross correlation coefficient between a given divergence image and the images at later times. The time interval after which the correlation coefficient drops to the noise level is taken as a measure of the lifetime of the structures.

3.5.1   Intergranular lane age method

The mesogranular size and lifetime statistics presented here are obtained using a $37.5 \cdot \tau_{av}$ (5 hours) long time series of images like that shown in Fig. 3.17 b. The size of a mesogranular cell is taken as the average area over the cell's lifetime (sum of area in each timestep divided by the number of timesteps). The obtained mesogranule properties may depend on t_0 (the threshold time for the lanes to be marked as mesolanes, the averaging time in case of the velocity divergence field), hence we set t_0 equal to $7.5 \cdot \tau_{av}$ (one hour) for the presented analysis and consider the dependence on t_0 in the next section. We use a segmentation algorithm to uniquely label each mesogranule and track it throughout the timeseries. Figure. 3.25 shows an example of a segmented mesogranule image. The tracking algorithm works as follows: first, in each mesogranule image the mesocells are uniquely labelled with a number. Next, for each pair of subsequent mesogranule images, the algorithm finds the mesocells that share the most area in both images. Unless a splitting has occurred, such cells are taken to be the same mesogranule. The time resolution of the timeseries is sufficient so that the mesocells do not significantly shift their position between subsequent images, and the above scheme works properly. Mesogranules defined by the mesolane method appear and disappear in the model in the similar way as the granules do: a mesogranule can either contract to a point or split in two or more new mesogranules. These evolution properties follow from the granule evolution, no new parameters are introduced.

For technical reasons, we remove in each image all features whose area is smaller than 10 pixels. Such features arise due to the image processing algorithm, usually they are small mesogranules (or parts of mesogranules) with the mesolanes very close to each other (a few pixel distance). The algorithm can lead to an artificial connection of the mesolanes, resulting in a splitting and production of smaller features with an area of only a few pixels. Hence, in order to prevent such an artificial cascade of very small mesogranules, we remove these small features.
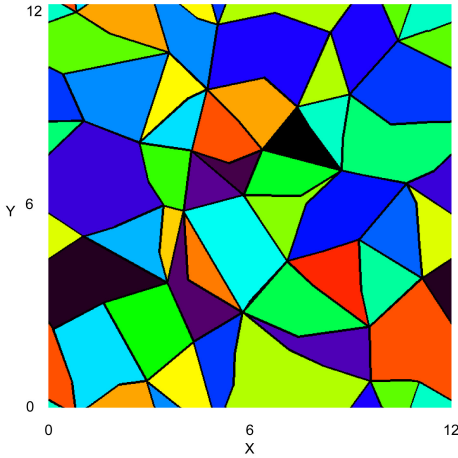
Figure 3.25: Example of a segmented image used to obtain mesogranule statistics.

There is a bias in the mesostatistics data due to the fact that the mesogranules which still exist in the domain at the end of the dataset, and thus have not covered their full life span (here called SE cells), are also included in the statistics. To check the significance of the bias we applied two other rules of data acquisition in case of the *CV/AL* model: (A) we excluded the SE cells from the statistics, and (B) we extracted the statistics from a $7.5 \cdot \tau_{av}$ shorter dataset and used the remaining $7.5 \cdot \tau_{av}$ of the data to extract the correct values for the SE cells. The mean and median vales of mesolifetimes and sizes for all models are presented in Table 3.1.A. For the CV/AL model we also present the case (A) and (B) values, along with the same values extracted from a $150 \cdot \tau_{av}$ long dataset (all the other values come from a $37.5 \cdot \tau_{av}$ long dataset). As seen in Table 3.1.A, the SE cells do not affect the obtained values significantly. Hence, for the other versions of the model we do not apply any special treatment to the SE cells.

The mesostatistics for the random walk model versions are biased due to the following reason: as already mentioned, when a mesogranule contracts and becomes less than 10 pixels in size, it is removed from the segmented image (Fig. 3.25) and substituted with a intergranular lane. Nevertheless, it is still present in the original images from which the segmented images are produced. In the cell-competition models such small mesogranules will vanish in the next few timesteps due to the cell-competition movement rule, but in the random walk case the vertices of the small cell can move apart in the next timesteps, enlarging the cell above 10 pixel size. Such an event will produce a new mesogranule in the segmented image and will be recorded as a splitting event of one of the neighboring mesogranules. Since in the random motion scheme the vertices have no preferred direction of motion, it often happens that such small features oscillate around the 10 pixel size, hence confounding the results. To prevent this, we introduce the "S-splitting" rule, which

states that an offspring cell with an area equal or greater than 90% of the parent cell inherits the identity of the parent. This prevents such reappearance of small mesogranules from being recorded as a splitting of a neighbor, but the small mesogranule is still recorded as a new one, thus increasing the number of small short-lived cells. Figures 3.26 to 3.35 show the mesogranule statistics for the selected models, with the mesogranular threshold time t_0 equal to $7.5 \cdot \tau_{av}$ (one hour). The corresponding figures for the S-splitting method can be found in the Appendix.
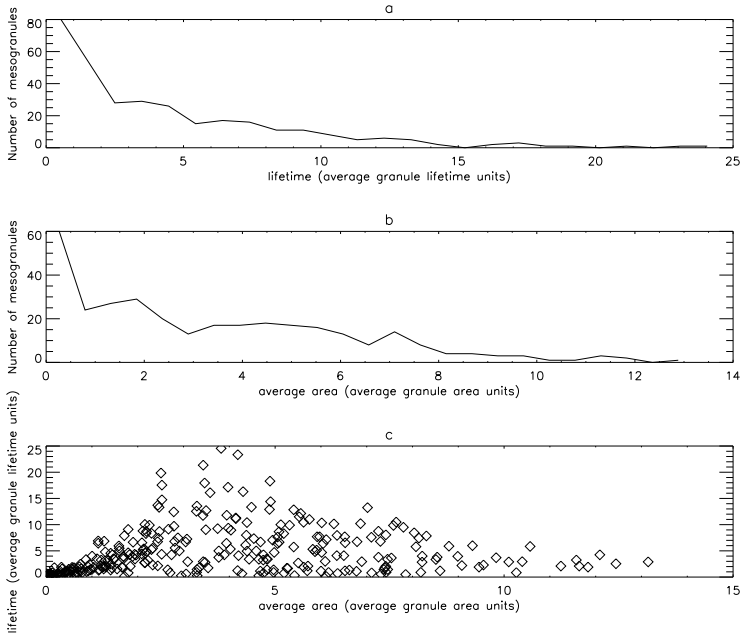
Figure 3.26: Mesogranulation statistics: histograms of (a) lifetime and (b) average area, (c) is a scatter plot of size versus lifetime. *CV/AL* model.
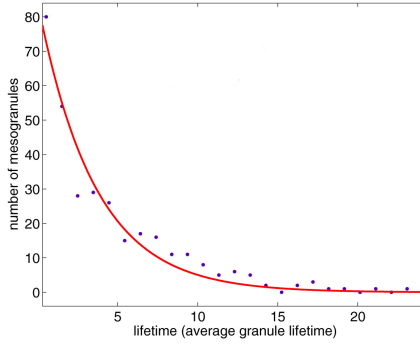
Figure 3.27: Mesogranular lifetime histogram with an exponential fit. *CV/AL* model. The e-folding time equals $3.5 \cdot \tau_{av}$.
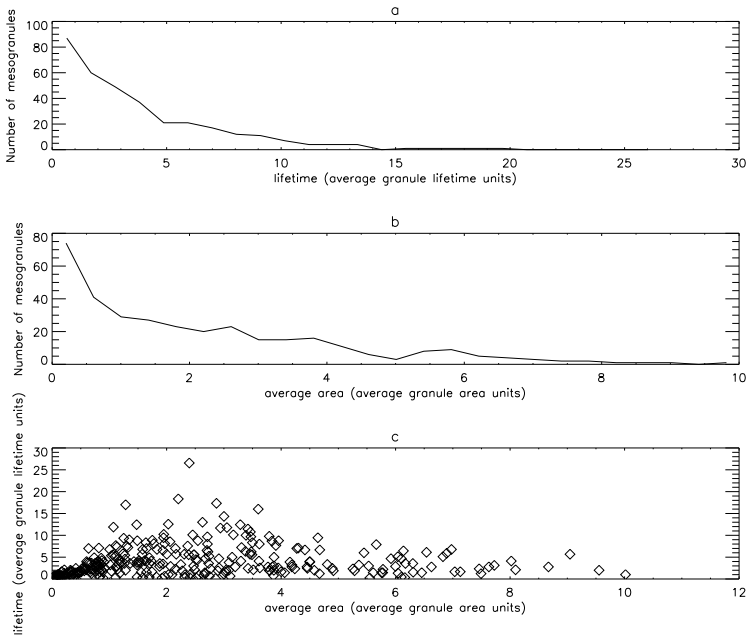
Figure 3.28: Mesogranulation statistics: histograms of (a) lifetime and (b) average area, (c) is a scatter plot of size versus lifetime. *CA/L* model.
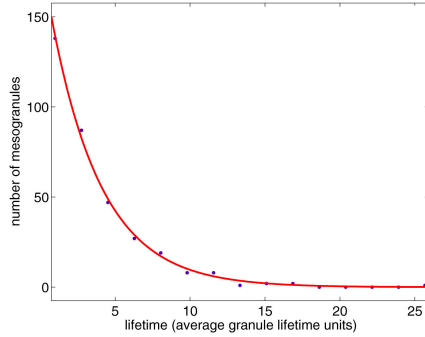
Figure 3.29: Mesogranular lifetime histogram with an exponential fit. *CA/L* model. The e-folding time equals $3.4 \cdot \tau_{\mathrm{av}}$.
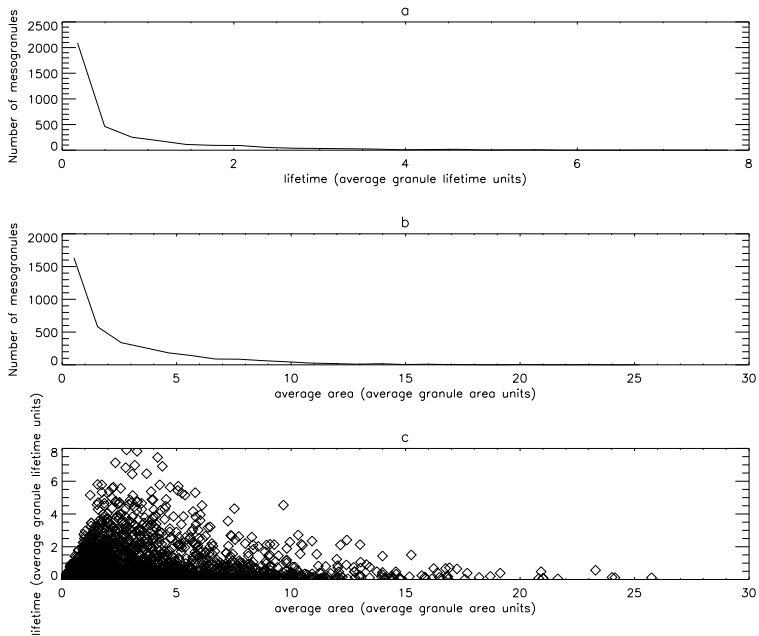
Figure 3.30: Mesogranulation statistics: histograms of (a) lifetime and (b) average area, (c) is a scatter plot of size versus lifetime. *RV/AL* model.
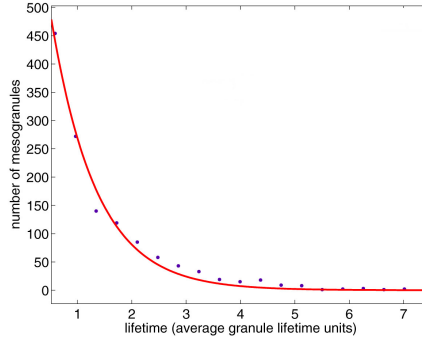
Figure 3.31: Mesogranular lifetime histogram with an exponential fit. *RV/AL* model. The e-folding time equals $0.8 \cdot \tau_{av}$.
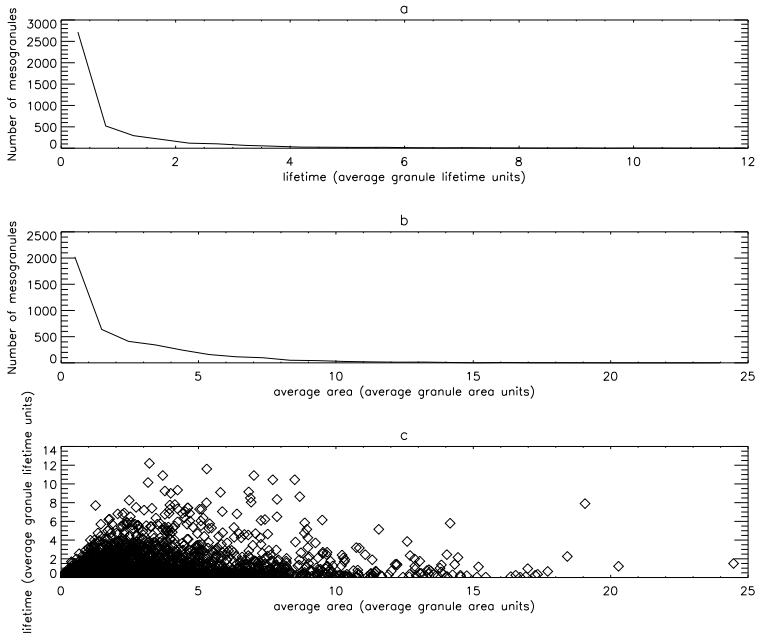
Figure 3.32: Mesogranulation statistics: histograms of (a) lifetime and (b) average area, (c) is a scatter plot of size versus lifetime. *RV/R* model.
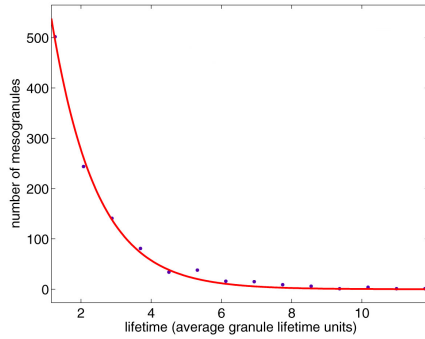
Figure 3.33: Mesogranular lifetime histogram with an exponential fit. *RV/R* model. The e-folding time equals $1.3 \cdot \tau_{av}$.
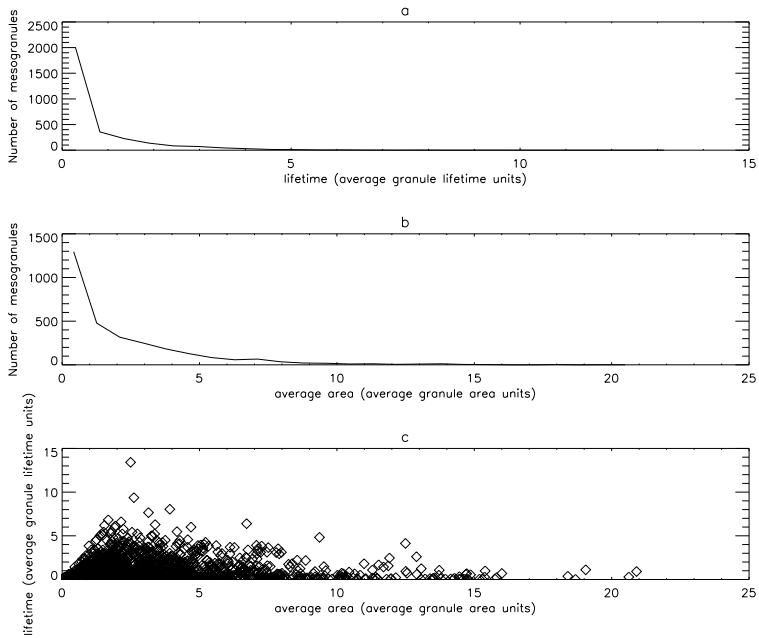
Figure 3.34: Mesogranulation statistics: histograms of (a) lifetime and (b) average area, (c) is a scatter plot of size versus lifetime. *RV/A* model.
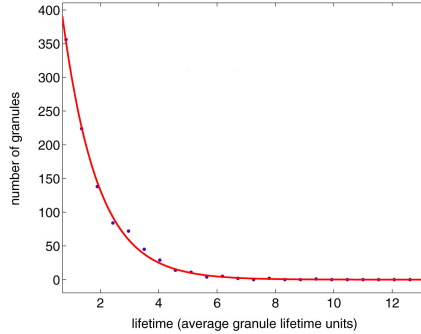
Figure 3.35: Mesogranular lifetime histogram with an exponential fit. *RV/A* model. The e-folding time equals $1.2 \cdot \tau_{\text{av}}$.

The mesogranule lifetime and size histograms for all the analyzed model versions can be approximated by an exponential, as illustrated in corresponding figures for lifetime distribution in each case. The most abundant are the smallest, shortest-lived cells. The exponential distribution is a memoryless random distribution, which means that the rate at which mesogranules disappear is constant, and a cell is just as likely to disappear in the first second of its existence as it is in the n-th.

The S-split rule increases the average lifetimes of mesogranules, while decreasing the average area. This is due to the following: the S-split rule preserves the identity of a mesogranule when a splitting event cuts off an area smaller than 10% of the cell, therefore increasing the lifetime of such mesogranule. On the other hand, without the S-split rule, the large area offspring of such an unequal splitting is recorded as a new mesogranule and increases the number of large cells, hence increasing the average area. In the scatter plots of the cell-competition versions of the model one can see traces of a relation between mesogranule size and lifetime, particularly for the small (short-lived) cells. In the random cases the number of detected mesogranules is much larger, many of those being artifacts of the mesogranule detection/tracking algorithm, as discussed earlier in this section. In particular, the number of very short-lived cells of all sizes in the no-S-split random versions is produced by constant reappearing of small mesogranules, which oscillate around the 10 pixel detection threshold. The other reason for a larger number of mesogranules in the random versions of the model is that the average granule size in those versions is smaller, hence more granules/mesogranules in the domain. The properties of mesogranules in all the analyzed model versions are very similar, suggesting that the statistical characteristics of mesogranulation defined by the mesolanes in the model do not depend strongly on the detailed granulation interaction rules.

Table 3.1.A: Mesogranulation properties for the selected models. All values in average granule lifetime (τ_{av}) and area (Area$_{av}$) units, respectively. Symbols: "-S" = S-split rule, "ns" = only cells larger than $2 \cdot$ Area$_{av}$ and living longer than $2 \cdot \tau_{av}$ were included, "CV/AL-L" = values extracted from a $150 \cdot \tau_{av}$ long timeseries, "no SE" = no SE cells included (see text), "*" = including correct values for the SE cells (see text)."E-fold. time" = the e-folding time of the exponential fit to the lifetime histograms.

-	Median area	Mean area	Median lifetm.	Mean lifetm.	E-fold. time
RV/A	1.2	2.2	0.2	0.7	1.2
RV/A-S	0.5	1.1	0.2	1.3	2.2
RV/A ns	3.6	4.1	3.1	3.3	1.6
RV/A-S ns	3.3	3.8	5.3	5.9	4.2
RV/R	1.2	2.3	0.3	0.8	1.3
RV/R-S	0.6	1.3	0.4	1.5	2.9
RV/R ns	3.9	4.6	3.2	3.9	1.9
RV/R-S ns	3.6	4.2	5.0	6.1	4.0
CV/AL	2.8	3.5	3.0	4.4	3.5
CV/AL no SE	2.5	3.5	3.0	4.3	-
CV/AL *	2.8	3.5	3.4	4.7	-
CV/AL-L	3.1	3.9	3.3	4.7	-
CV/AL-L *	3.1	3.9	3.4	4.9	-
CV/AL ns	4.8	5.2	6.7	7.8	6.7
CV/AL ns no SE	5.1	5.5	6.8	7.7	-
CV/AL ns *	4.9	5.3	7.2	7.9	-
CV/AL-L ns	5.1	5.5	6.5	7.8	-
CV/AL-L ns*	5.1	5.5	6.7	7.9	-
CV/AL-S	2.4	2.6	4.3	7.5	3.4
CV/AL-S ns	4.0	4.3	10.4	13.2	11.7
RV/AL	1.3	2.6	0.2	0.6	0.8
RV/AL-S	0.5	1.2	0.2	1.2	2.0
RV/AL ns	3.5	4.2	2.9	3.2	1.2
RV/AL-S ns	3.5	4.0	4.7	5.5	3.6
CA/L	1.7	2.3	2.4	3.6	3.4
CA/L-S	1.2	1.6	3.9	6.2	4.3
CA/L ns	3.6	4.1	5.0	5.9	3.8
CA/L-S ns	2.9	3.2	12.0	12.7	14.2

3.5.1.1 Mesogranulation properties: dependence on the threshold time t_0

The important question concerning mesogranulation is whether it has distinctive time and size scales, which are independent of the data analysis methods applied, and particularly of the choice of the threshold time t_0. Figures 3.36-3.37 show the dependence of mesogranular characteristics on the threshold time in the CV/AL and RV/R model versions

$(150 \cdot \tau_{av}$ long datasets). Since the emerging mesogranulation properties are qualitatively quite similar for all granule interaction rules, we chose only these two model versions as the most opposite in nature for this analysis. The "ns" means that only cells larger than $2 \cdot Area_{av}$ and living longer than $2 \cdot \tau_{av}$ were included. The mean mesogranule size and lifetime increase with threshold time t_0 for both model versions, suggesting that mesogranulation defined by the mesolanes in the model has no intrinsic scale. The corresponding figures for the S-splitting method for the two model version can be found in the Appendix.
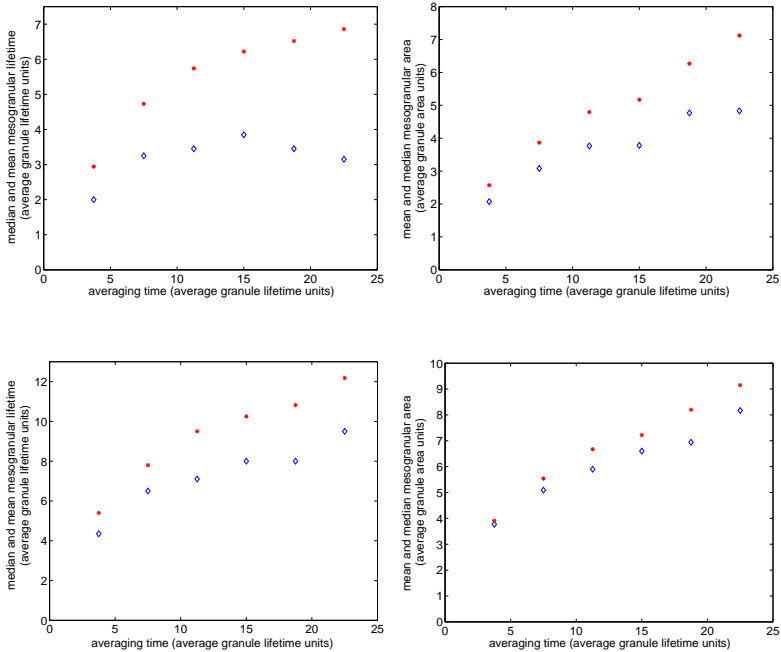
Figure 3.36: Dependence of mesogranular median (diamonds) and mean (asterisks) lifetime (left) and size (right) on the threshold time. Top row *CV/AL* model, bottom row *CV/AL* ns model.
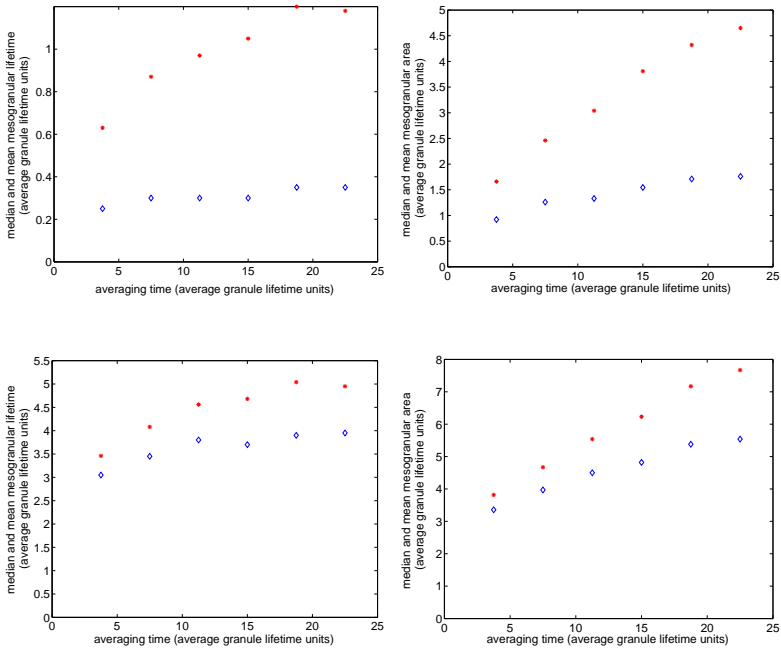
Figure 3.37: Dependence of mesogranular median (diamonds) and mean (asterisks) life-time (left) and size (right) on the threshold time. Top row *RV/R* model, bottom row *RV/R* ns model.

3.5.2   Horizontal velocity divergence patch method

Mesogranulation statistics presented here are extracted from the divergence of the LCT horizontal velocity. The datasets are $150 \cdot \tau_{av}$ long timeseries of granulation intensity images (images like the one in Fig. 3.1, to which the shading algorithm given by Eq. 3.2 was applied), from which the horizontal velocity was obtained with the LCT algorithm (see Section 3.2.2 for details). When analyzing velocity divergence areas one must set a threshold for mesogranule labelling, that is the cutoff level above which image pixels are treated as belonging to a mesogranule. This obviously influences the retrieved area statistics; higher cutoff levels produce smaller cells and vice versa. The cutoff is set in the following way: a t_0 (averaging time) running mean is employed for each dataset to produce a time sequence of t_0-averaged velocity divergence maps. For each map the rms (root mean square) value is recorded, and then the time average of the rms over the whole dataset is calculated. This produces an average rms value Λ for a given t_0. The cutoff value is then set to be a fraction of Λ. Figure. 3.38 shows an example of two velocity divergence patch images for the cutoff level 0.5Λ and 0.7Λ for the CV/AL model, t_0 equals $7.5 \cdot \tau_{av}$. For the mesogranulation analysis we choose the cutoff level
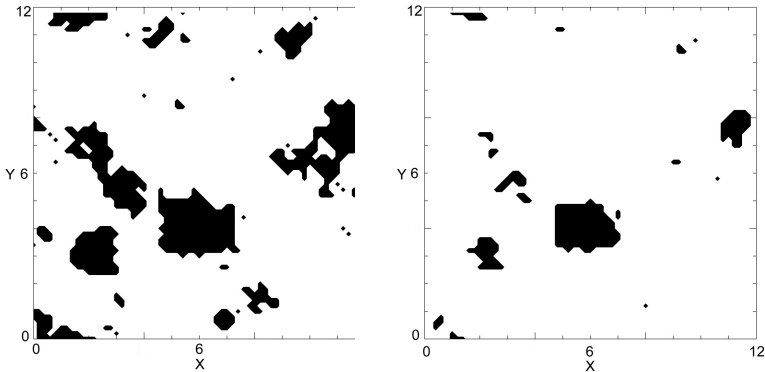
Figure 3.38: Velocity divergence patch image for the cutoff level $0.5 \cdot \Lambda$ (left) and $0.7 \cdot \Lambda$ (right), CV/AL model.

to be $0.5 \cdot \Lambda$. In the analysis all patches smaller than 0.66 of the average granule area are disregarded. This number has been chosen to roughly correspond to the 10 pixel size objects removed from the images in the intergranular lane age method. Mesogranules are analyzed in two ways: one method is based on tracking mesogranules in time, hence allowing for explicit extraction of mesogranule lifetimes. The tracking algorithm is the same as used in the mesolane method (see Section 3.5.1). The size of mesogranules is then taken as a lifetime-averaged area of the cell. The other method is the snapshot analysis: each mesogranule image (t_0-averaged velocity divergence map) in the dataset is treated as independent, and the instantaneous mesogranule areas are extracted from each

such image separately. The latter approach avoids the problems posed by the tracking algorithm, when, for example, a divergence patch lies just above/below the threshold, appearing and disappearing consecutively from one image to the next. Without tracking mesogranules in time, it is not possible to explicitly measure the lifetime of each cell. A measure of the time persistence of mesogranules in the snapshot analysis can therefore be the decay time of the coefficient of cross-correlation between subsequent divergence maps.

3.5.2.1 Tracking statistics

The following Figures 3.39-3.44 present mesogranulation size and lifetime statistics for the selected model versions, obtained by tracking individual mesogranules present in the simulation. The averaging time t_0 equals $7.5 \cdot \tau_{av}$ (~1 hour). The size of a mesogranule is the average size over the cell's lifetime. The presented statistics are obtained with the S-split method, which states that an offspring cell with an area equal or greater than 90% of the parent cell inherits the identity of the parent. This decreases the number of very short-lived cells, since such an unequal splitting will not be recorded. Nevertheless, the number of short-lived cells is still artificially multiplied by events where the mesogranule (or its part) lies close to the threshold level and "flickers" between subsequent divergence maps, with each reappearing being recorded as a new mesogranule.
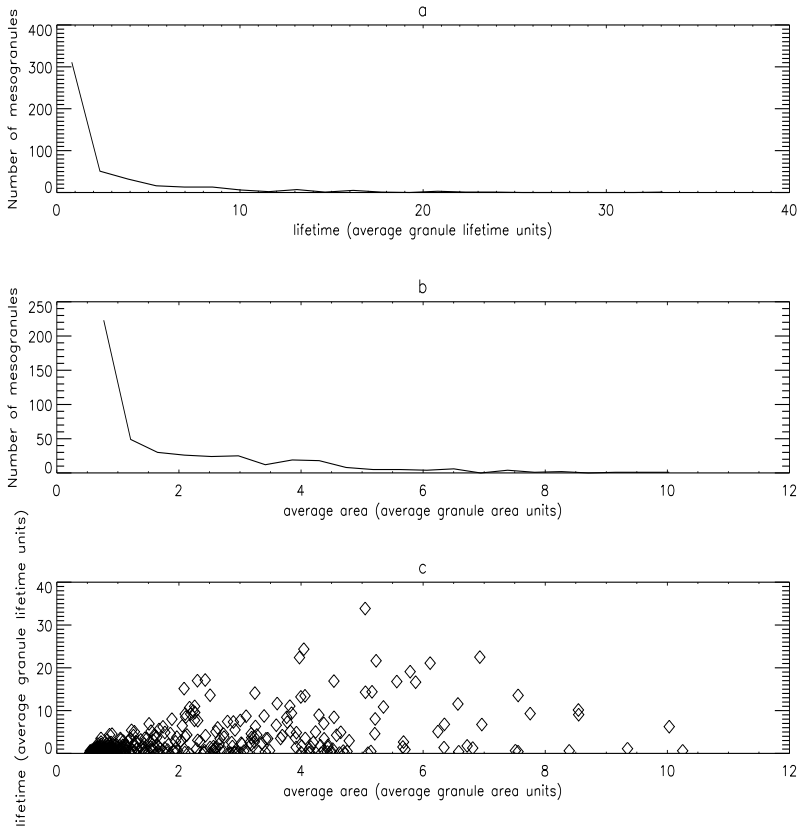
Figure 3.39: Histograms of mesogranule lifetime (a), size (b), and a scatter plot of size versus lifetime (c). *CV/AL* model, $t_0 = 7.5 \cdot \tau_{av}$.
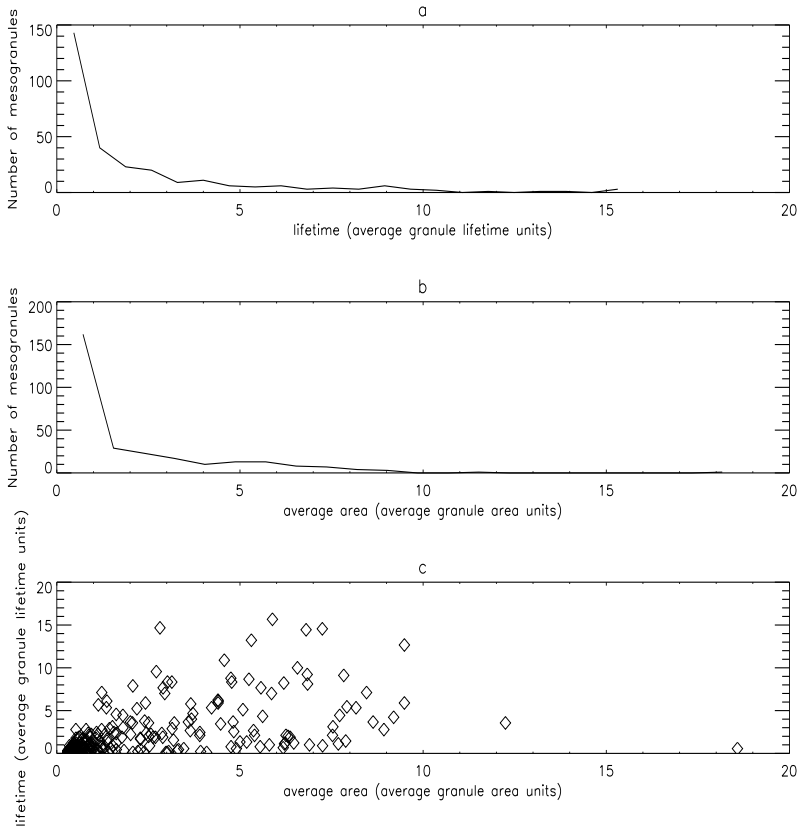
Figure 3.40: Histograms of mesogranule lifetime (a), size (b), and a scatter plot of size versus lifetime (c). *CA/L* model, $t_0 = 7.5 \cdot \tau_{av}$.
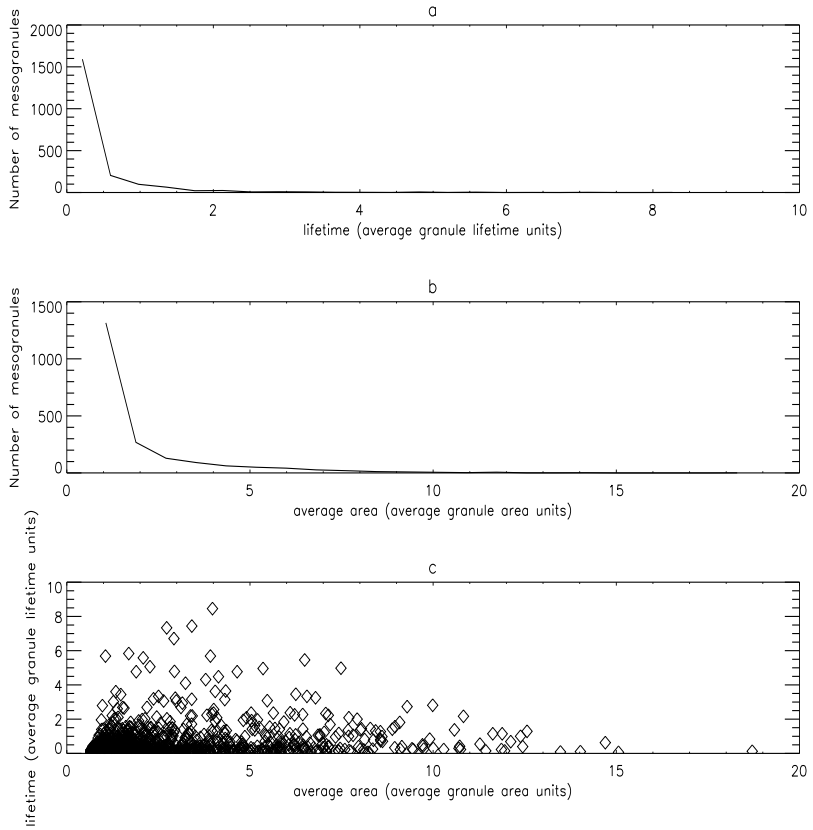
Figure 3.41: Histograms of mesogranule lifetime (a), size (b), and a scatter plot of size versus lifetime (c). *RV/AL* model, $t_0 = 7.5 \cdot \tau_{av}$.
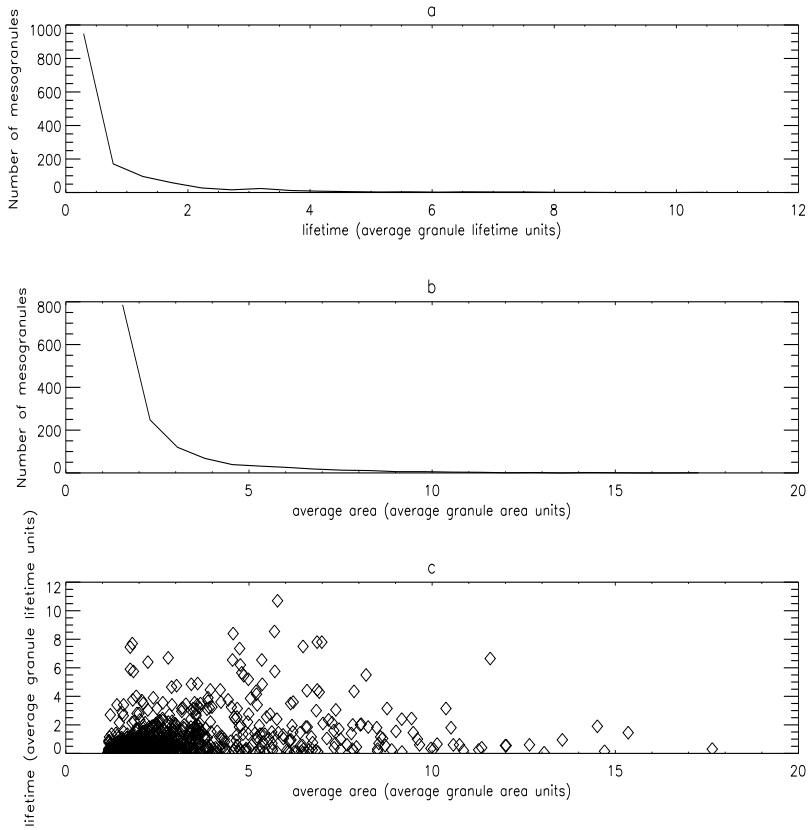
Figure 3.42: Histograms of mesogranule lifetime (a), size (b), and a scatter plot of size versus lifetime (c). *RV/R* model, $t_0 = 7.5 \cdot \tau_{av}$.
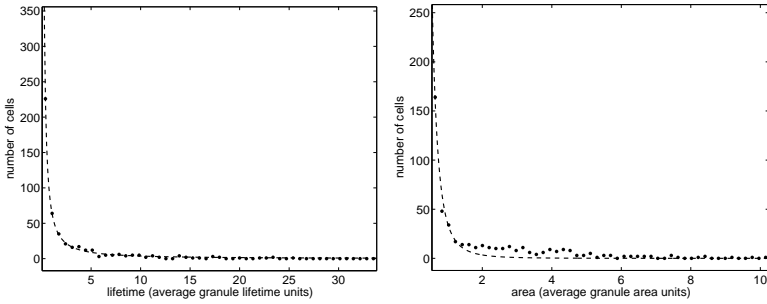
Figure 3.43: Mesogranule lifetime and size histograms from Fig. 3.39 (CV/AL model) with a power law fit. The power law exponents are -1.27 for lifetime and -3.38 for the area.
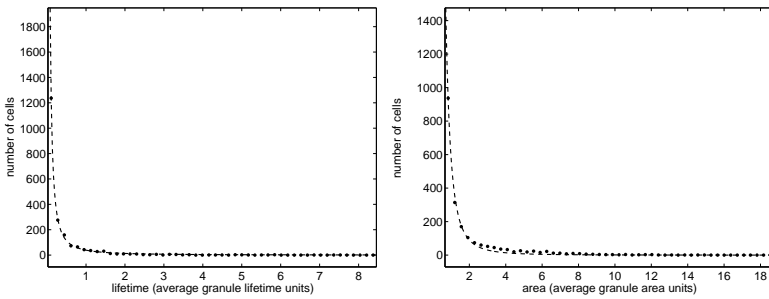
Figure 3.44: Mesogranule lifetime and size histograms from Fig. 3.41 (RV/AL model) with a power law fit. The power law exponents are -1.54 for lifetime and -2.67 for the area.

The size and lifetime histograms of mesogranules in Figs. 3.39-3.42, obtained by tracking the positive velocity divergence patches, obey a power law distribution as seen in the examples for the *CV/AL* and *RV/AL* models (Figs.3.43-3.44). This means that there is no characteristic scale of mesogranulation obtained with the tracking method for a given averaging time t_0. This result is different from the intergranular lane age method from Section 3.5.1, where the mesogranule size and lifetime histograms were exponential. Since the same tracking algorithm was used for both methods, the difference lies in the mesogranule definition. Table 3.2 shows the power law exponents of the fits to the size and lifetime distributions for the selected models. The power law behavior of Figs. 3.39-3.42 is also true for the properties obtained without the S-split method.

Table 3.2: Values of the exponents of the power law fits to the mesogranule area and lifetime distributions for the selected models (Figs. 3.39-3.42) .

Model version	CV/AL	RV/AL	RV/R	CA/L
Lifetime fit exponent	-1.27	-1.54	-1.43	-1.27
Size fit exponent	-3.38	-2.67	-2.72	-1.75

Tracking statistics: dependence on the averaging time   Again, it is interesting to see how the average mesogranule properties depend on the choice of the averaging time t_0. Figures 3.45-3.52 present this dependence for mesogranules defined as positive velocity divergence patches. The "ns" model versions mean that only cells larger than two average granule areas and living longer than two average granule lifetimes were included in the analysis. This was done to check how the statistics are influenced by the number of small short-lived cells that may appear as artifices of the tracking algorithm.
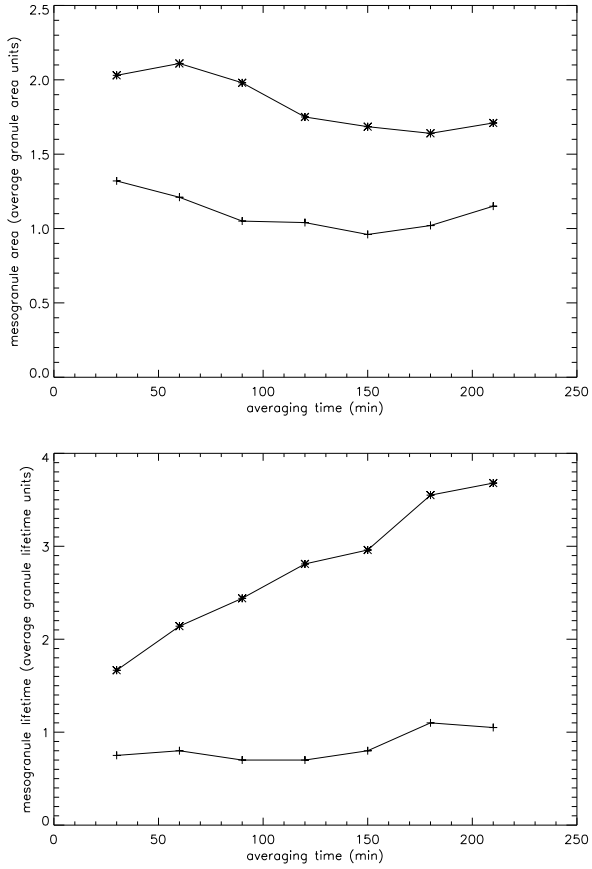
Figure 3.45: The dependence of the mean (asterisks) and median (crosses) mesogranule area (top) and lifetime (bottom) on the averaging time t_0, *CV/AL* model version.
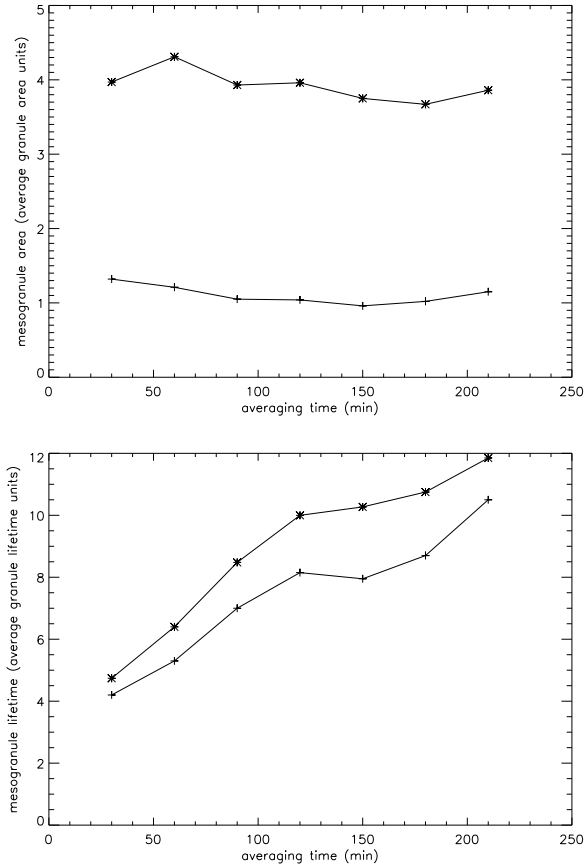
Figure 3.46: The dependence of the mean (asterisks) and median (crosses) mesogranule area (top) and lifetime (bottom) on the averaging time t_0, $CV/AL - ns$ model version.
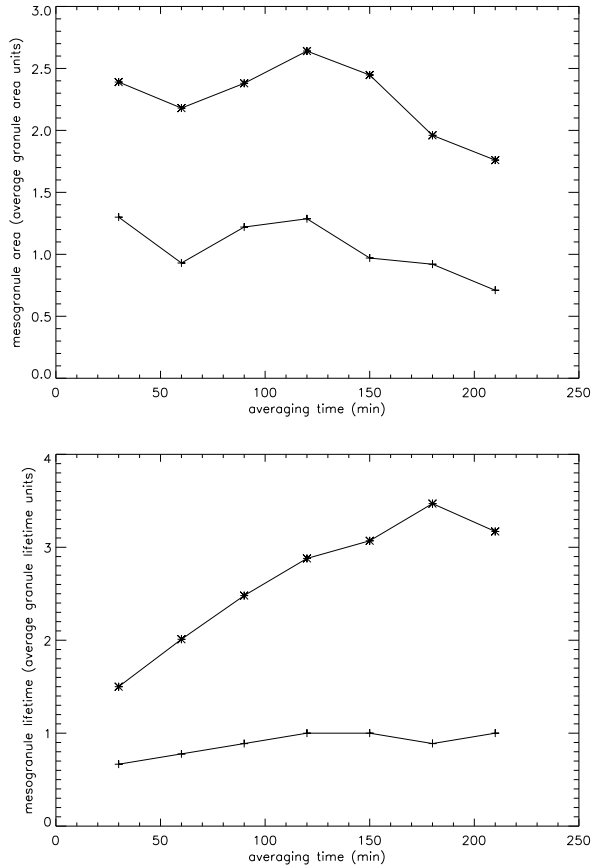
Figure 3.47: The dependence of the mean (asterisks) and median (crosses) mesogranule area (top) and lifetime (bottom) on the averaging time t_0, CA/L model version.
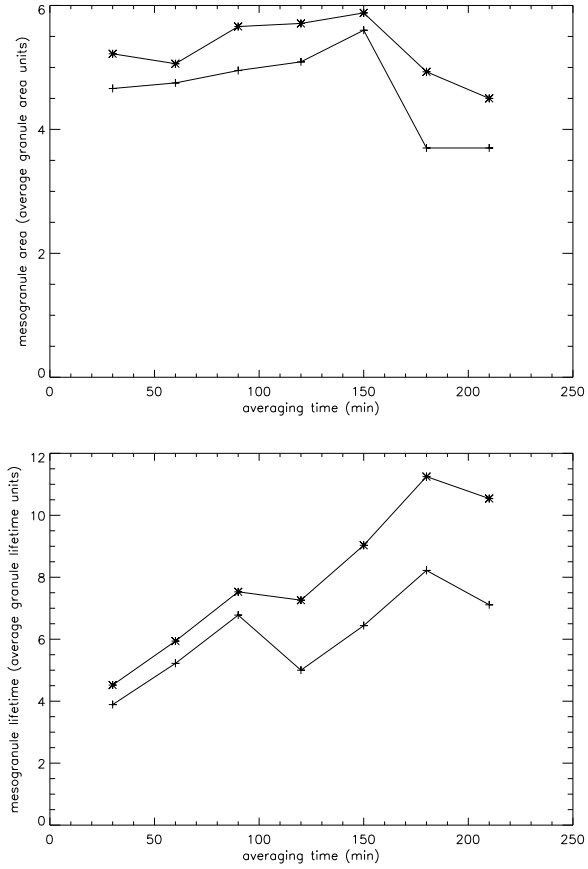
Figure 3.48: The dependence of the mean (asterisks) and median (crosses) mesogranule area (top) and lifetime (bottom) on the averaging time t_0, $CA/L - ns$ model version.
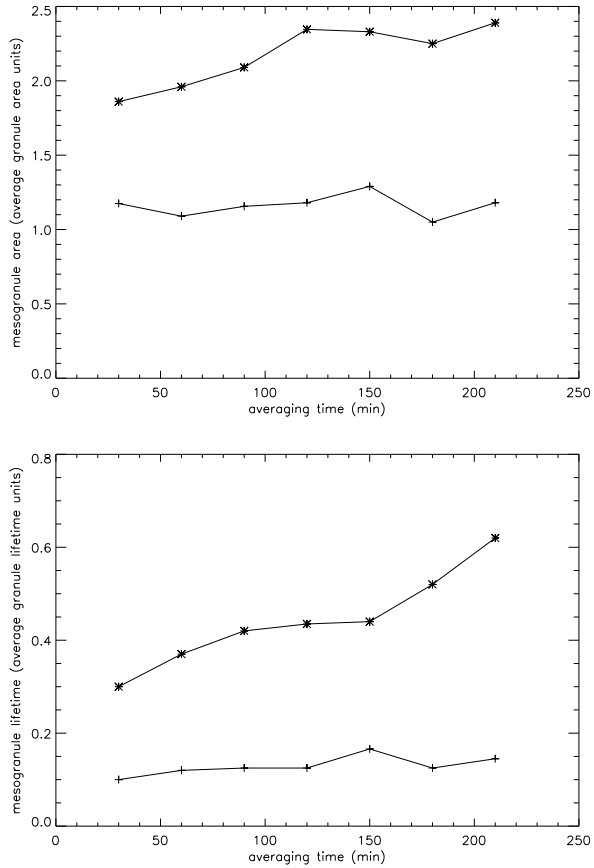
Figure 3.49: The dependence of the mean (asterisks) and median (crosses) mesogranule area (top) and lifetime (bottom) on the averaging time t_0, *RV/AL* model version.
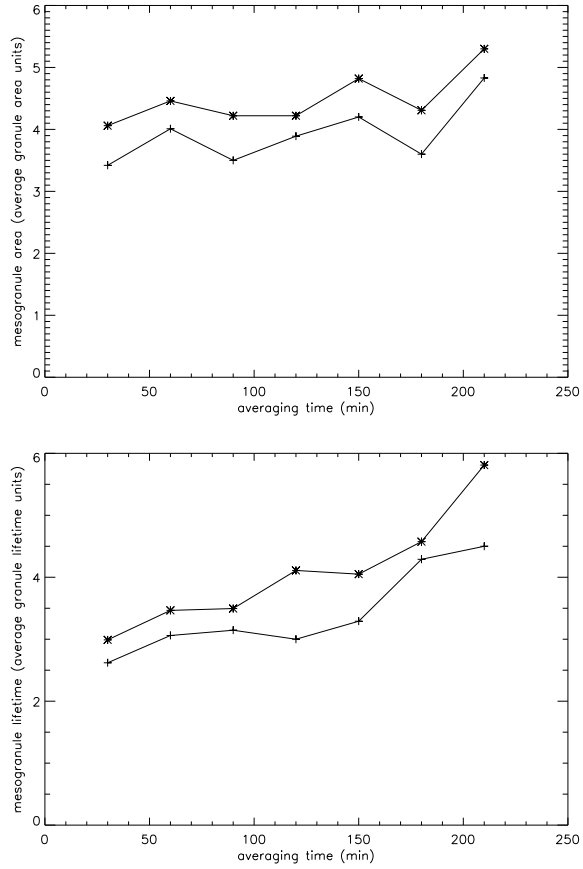
Figure 3.50: The dependence of the mean (asterisks) and median (crosses) mesogranule area (top) and lifetime (bottom) on the averaging time t_0, $RV/AL - ns$ model version.
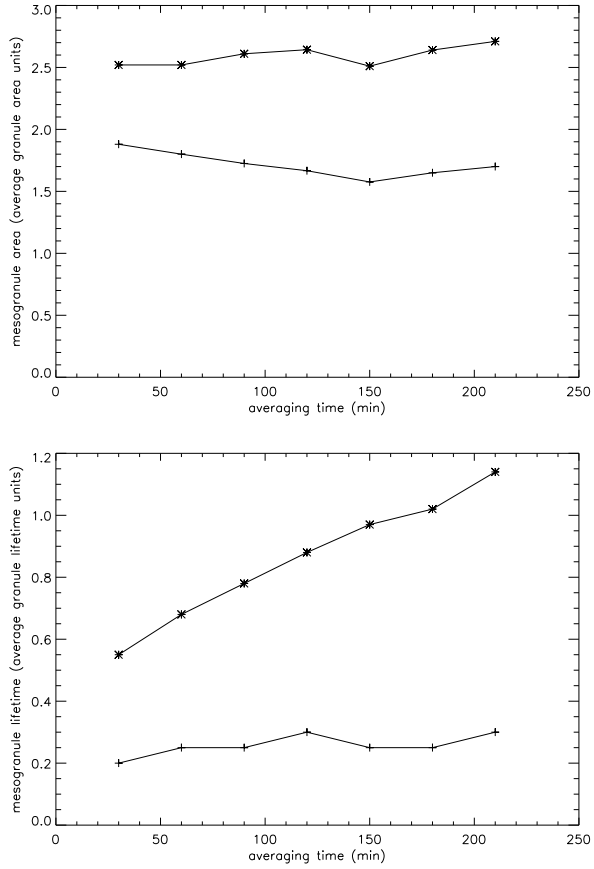
Figure 3.51: The dependence of the mean (asterisks) and median (crosses) mesogranule area (top) and lifetime (bottom) on the averaging time t_0, RV/R model version.
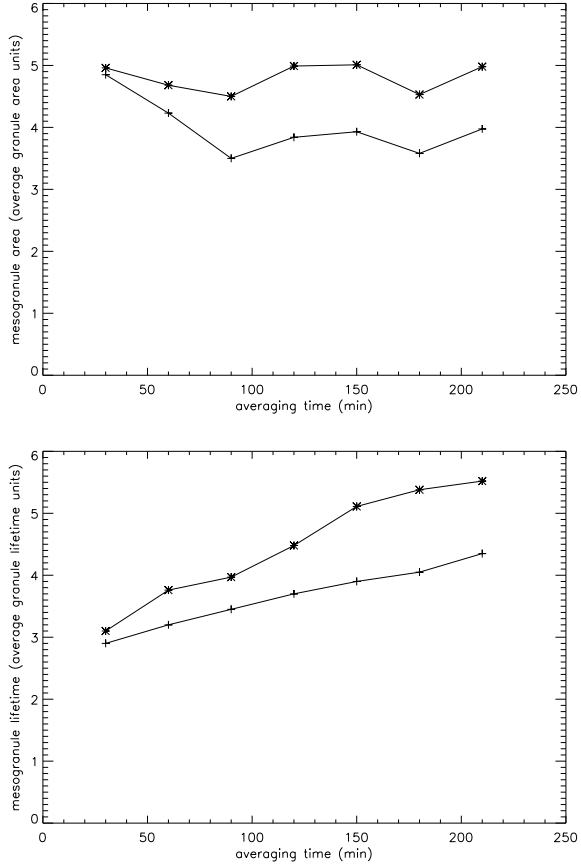
Figure 3.52: The dependence of the mean (asterisks) and median (crosses) mesogranule area (top) and lifetime (bottom) on the averaging time t_0, $RV/R - ns$ model version.

Figures 3.45-3.52 reveal that the mean mesogranule area stays more or less constant while the mean lifetime increases with the averaging time t_0. The only exception seems to be the *RV/AL* case (Fig. 3.49) where both values tend to increase slightly with t_0. Nevertheless, this effect diminishes when we exclude small short-lived mesogranules (Fig. 3.50). Hence, as opposed to the intergranular lane age method, the velocity divergence method produces mesogranules that do not have an intrinsic lifetime, but have a spatial scale that does not depend on the choice of the averaging time t_0. Nevertheless, the value of the average mesogranule area is not intrinsic, since it depends on the definition and value of the threshold.

3.5.2.2 Snapshot statistics

This section presents the mesogranule snapshot characteristics, for which each mesogranule image (t_0-averaged velocity divergence map) in the dataset is treated as independent, and the instantaneous mesogranule areas are extracted from each such image separately. In this way the difficulties associated with the application of the tracking algorithm can be avoided, but we lose any explicit information about the lifetimes of the cells. The cutoff level for mesogranule detection equals 0.3Λ.

A measure of the time persistence of mesogranules in the snapshot analysis can therefore be the decay time of the coefficient of cross-correlation between the subsequent divergence maps. Given a divergence map at time T, we cross-correlate it with all the divergence maps at later times. The time interval t, for which the cross-correlation coefficient between divergence images at times T and $T + t$ drops down to noise level, is taken as the mesogranule lifetime. Figure 3.53 presents the snapshot area histograms for the various model versions. The area distributions of mesogranules obtained with the snapshot method are exponential.

To understand why the size distributions are exponential, consider a following one-dimensional example: let's say there are N neighboring cells in a line. For a random walk model, the velocities of the cell motions are randomly distributed, as is the velocity divergence. Hence, the probability P_i that the velocity divergence at each cell site is above threshold is the same for each cell, regardless of the neighbors. To have a positive divergence area we need n sites in a row to have a positive divergence value, which yields $P(n) = P_i^n = e^{n \cdot ln(P_i)}$. Therefore, in such case the shape of the size distribution of the divergence areas is exponential. In the cell-competition case, the velocities of the cell motions are randomly distributed above a certain spatial scale of a few cells. This is verified by the behavior of the zero-lanes in the one-dimensional model (Fig. 2.9), which are randomly advected in the domain for both the random walk and the cell-competition model versions. Hence, the above reasoning applies also to the cell-competition case. In the two-dimensional model the formulas will be more complicated, but the logic is the same and the resulting size histograms of the velocity divergence areas should also be close to exponential.
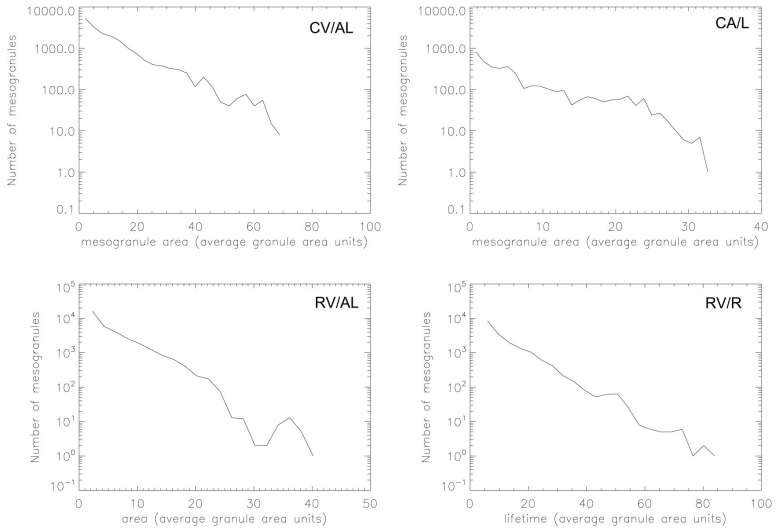
Figure 3.53: The snapshot statistics of the mesogranule area for the selected model versions.

Snapshot statistics: dependence on the averaging time The following Figures 3.54-3.57 present the dependence of the mean (and median) mesogranule area and the correlation decay time on the averaging time t_0 for the chosen model versions.
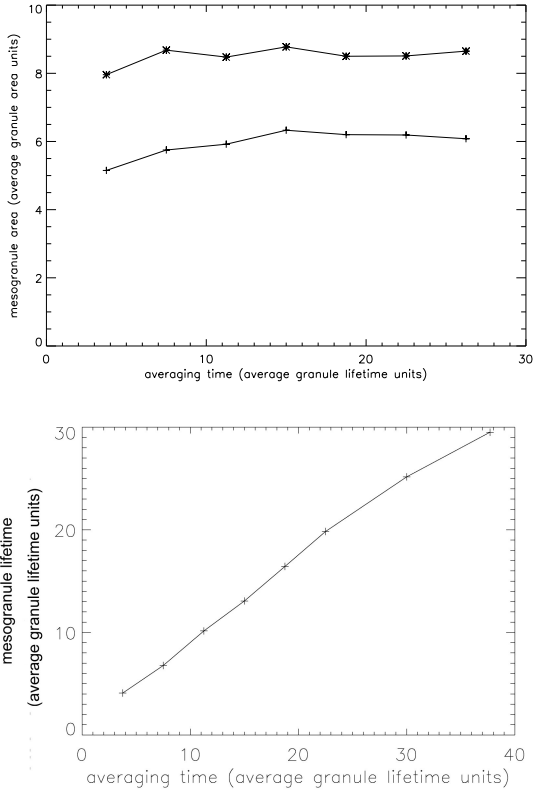
Figure 3.54: Top: the dependence of the mean (asterisk) and median (crosses) snapshot mesogranule area on the averaging time t_0. Bottom: the dependence of the cross-correlation decay time on the averaging time t_0. *CV/AL* model version.
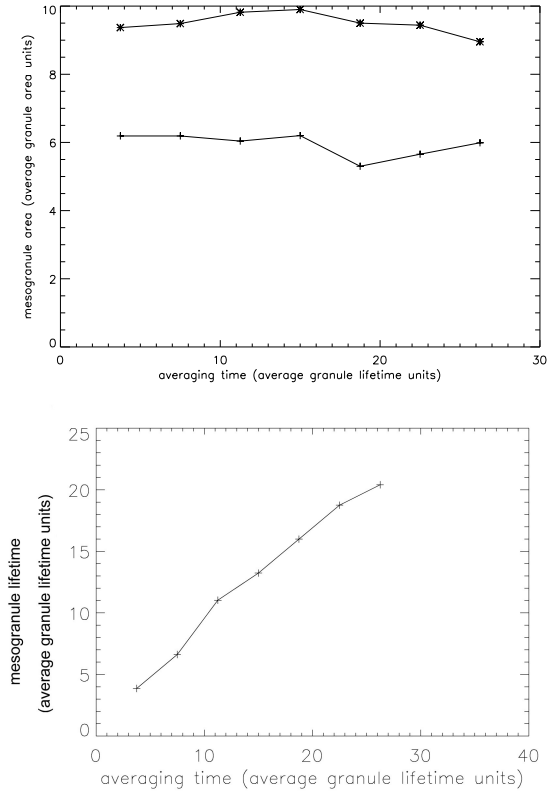
Figure 3.55: Top: the dependence of the mean (asterisk) and median (crosses) snap-shot mesogranule area on the averaging time t_0. Bottom: the dependence of the cross-correlation decay time on the averaging time t_0. CA/L model version.
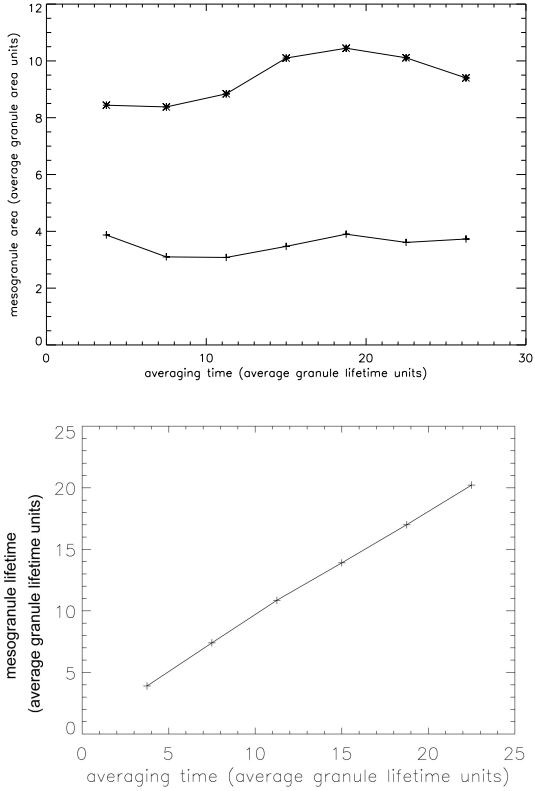
Figure 3.56: Top: the dependence of the mean (asterisk) and median (crosses) snapshot mesogranule area on the averaging time t_0. Bottom: the dependence of the cross-correlation decay time on the averaging time t_0. *RV/AL* model version.
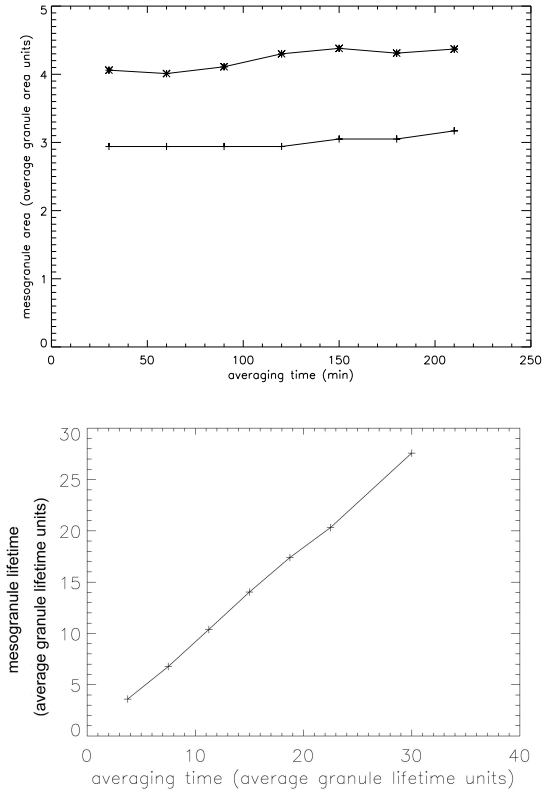
Figure 3.57: Top: the dependence of the mean (asterisk) and median (crosses) snapshot mesogranule area on the averaging time t_0. Bottom: the dependence of the cross-correlation decay time on the averaging time t_0. *RV/R* model version.

Just like in case of the tracking statistics, the mean mesogranule area does not depend on the choice of the averaging time t_0. Since the value of the area depends on the threshold definition and value, it is not intrinsic. The cross-correlation decay time for a given t_0 yields roughly the value of t_0, particularly so in the random walk cases, hence increasing linearly with the averaging time. Therefore, the snapshot statistics reveal no intrinsic scales of mesogranulation, confirming the results obtained with the tracking method.

3.6 Fragmenters and Trees of Fragmenting Granules (TFGs)

A so-called "Tree of Fragmenting Granules" (TFG) consists of all cells which originate form a single fragmenter cell, with repeatedly fragmenting granules (the offspring of a fragmenter that become fragmenters themselves) spawning the TFG structure. The investigation of the fragmenting granules, their spatial distribution on the solar surface, and whether they conglomerate into TFGs, has been the focus of recent studies of possible mesogranulation causes (Rieutord et al. 2000, Roudier et al. 2003, Roudier et al. 2004). The authors analyzed the TFGs and found that they are constantly present on the Sun. Moreover, they found that over 60% of the area covered by granules belonged to TFGs and that the lifetime of such granule families can reach many hours. From the power law behavior of the TFG's lifetime histograms they deduce that no characteristic timescale is present. The velocity field produced by a TFG, when averaged over the TFG's lifetime, yields a divergence area, with most of the TFGs covering an area with a diameter of ~6 Mm. Additionally, when performing the cork advection analysis, the authors found that the corks tend to accumulate in the areas of low granule splitting rates. Since the cellular automaton model presented in this work exhibits the mesogranulation effect, it is instructive to investigate the existence and characteristics of the TFGs, and the spatial distribution of the fragmenting granules. Since the splitting of a fragmenter is the only way of introducing new cells in the model, it follows that TFGs have to exist in such a system. Moreover, all granules present in the model at large times can be traced back to one parent cell. Figure 3.58 shows an example of a few coexisting TFGs in the domain (when a splitting occurs, we mark the position of the rectangle enveloping the two splitting triangular cells).
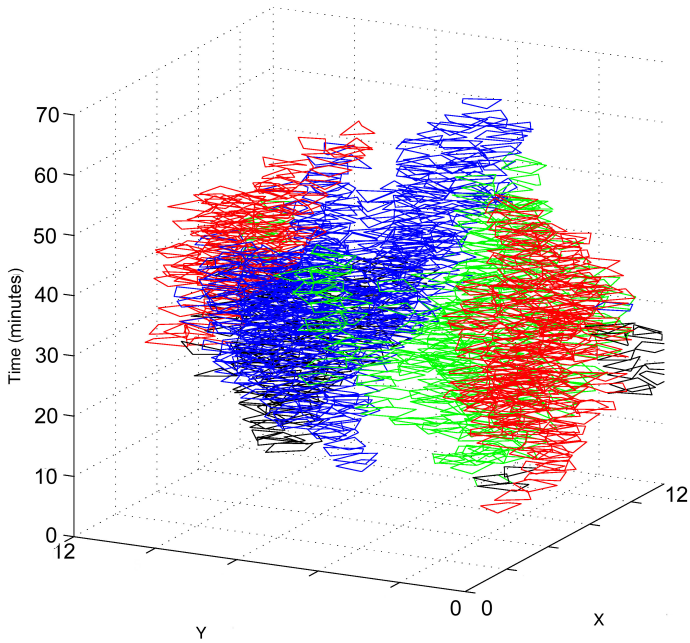
Figure 3.58: Example of the Trees of Fragmenting Granules (TFGs) in the *CV/AL* model version. Different colors depict different TFGs.

Fig. 3.59 shows a lifetime histogram of TFGs present in the model over a time interval of one hour. The histogram can be quite well fitted with a power law $f(x) = Ax^\alpha + B$, with the exponent $\alpha = -0.62$. The power law behavior is consistent with the findings of Roudier and coworkers (Roudier et al. 2003, Roudier et al. 2004) and it implies the absence of a characteristic timescale for TFGs. Concluding, the identity of a particular TFG depends only on the time at which we start our observation, and what seems to be two independent TFGs when we start their tracking at time t, will turn out to be two branches of a single TFG when we start the observation at time $t - T$, provided that T is sufficiently large. On the Sun not all granules appear by splitting of a fragmenter, there are singular events when a granule evolves out of a bright point in the intergranular lane. Hence, not all granules can be traced back to a single fragmenter, and there will be new TFGs appearing occasionally from such events. The merging of granules, which happens on the Sun but not in the cellular model, does not influence the conclusions drawn here, since the TFG-identity of the parent granules is preserved in the offspring cell.
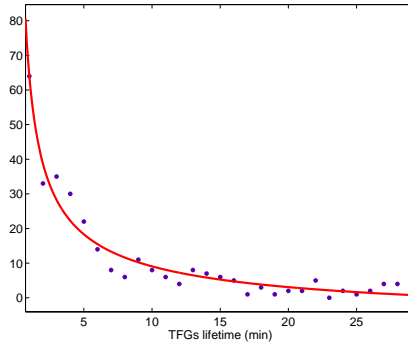
Figure 3.59: Histogram of the TFG lifetimes recorded over half an hour in the *CV/AL* model version, fitted with power law function $f(x) = Ax^\alpha$, where $\alpha = -0.62$.

3.6.1 Spatial distribution of the fragmenting granules

The occurrence and spatial distribution of the fragmenting granules on the Sun has been investigated in connection to mesogranulation. Oda (1984) studied the surface distribution of fragmenters during a 4 minute time interval, and interpreted them to outline a meso-size pattern, while Hirzberger et al. (1997) found that fragmenters exist predominantly in the mesogranule centers. Figures. 3.60 and 3.61 show the LCT velocity divergence field obtained from the cellular model (*CV/AL*) for the averaging time $t_0 = 7.5 \cdot \tau_{av}$ (~1 hour), together with the positions of fragmenting granules that occurred during the whole $7.5 \cdot \tau_{av}$ (Fig. 3.60) and over the last 5 minutes (Fig. 3.61) overplotted as white dots (when two adjacent triangles split, we mark the position of the new vertex, see Fig. 3.4). In both cases we find no preference of fragmenter positions, neither in the positive divergence

(mesogranule) nor in the negative divergence areas. The same is true for the spatial distribution of fragmenters that occurred during the last 10, 20 or 30 minutes of the $7.5 \cdot \tau_{av}$
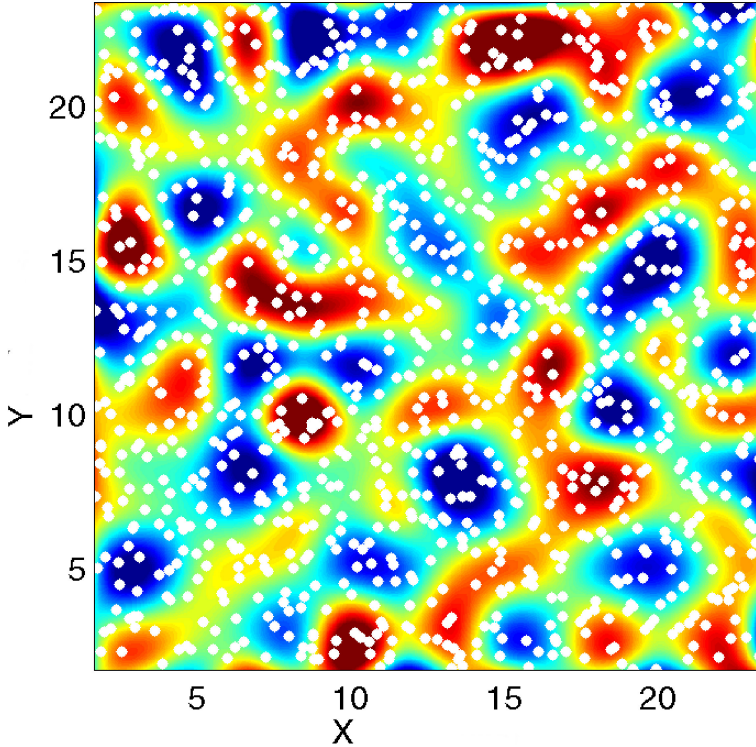
Figure 3.60: Positions of fragmenting granules over $t_0 = 7.5 \cdot \tau_{av}$ (~1 hour) period (white circles) overplotted on the t_0-averaged LCT velocity divergence field (red-positive, blue-negative) , *CV/AL* model version.
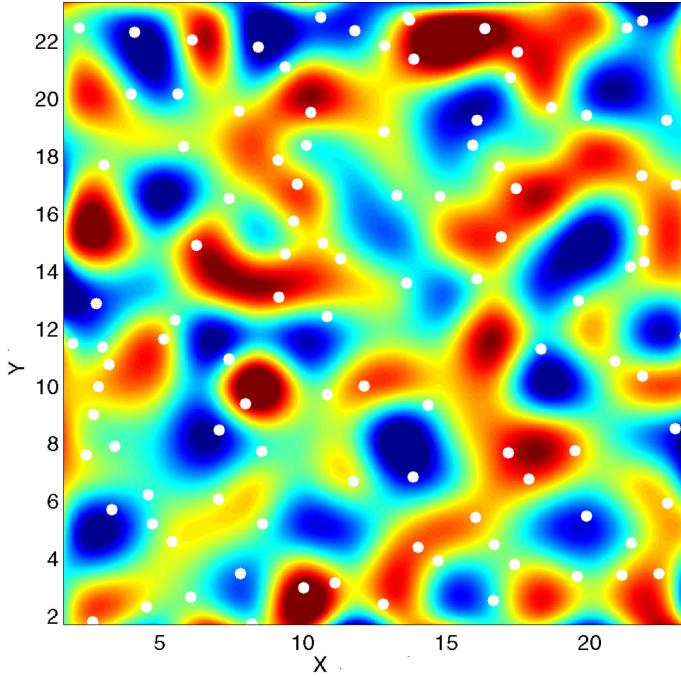
Figure 3.61: Positions of fragmenting granules over 5 minute period (white circles) over-plotted on the $t_0 = 7.5 \cdot \tau_{\text{av}}$-averaged LCT velocity divergence field (red-positive, blue-negative) , *CV/AL* model version.

3.7   Summary

In this chapter we presented a two-dimensional cellular automaton model of granulation, and showed that it is able to approximate the statistical size and lifetime properties of both observed and simulated granules quite well. The observed granulation size and lifetime distributions are close to exponential (Title et al. 1989, Brandt et al. 1991, Hirzberger et al. 1996, 1997, 1999, Müller et al. 2001), which is also true for most of the cellular model versions. Additionally, it is known that the fragmenting granules are statistically larger than the dissolving ones, while their lifetimes are very similar. This properties are also true for the granules in the cellular model. Hence, even though in the cellular model granules are parameterized by triangles, their statistical properties simulate the observed granulation properties sufficiently well for the purposes of this work i.e., investigation of mesogranulation as a self-arrangement effect of granulation cells.

Two cell interaction rules were presented: the cell-competition scheme, which approximates the scenario where the large cells spread and squeeze small cells out of existence, and a random walk scheme in which the motion of granules has no relation to the cell's properties. Additionally, four different cell splitting rules were employed to check the sensitivity of the result to the granule behavior rules. We have shown that mesogranulation emerges naturally in such a cell system, regardless of the employed cell motion and splitting schemes. Two methods of defining and detecting mesogranules were presented. The first one is based on the analogy to the cork analysis and the one-dimensional model presented in Chapter 2. We stipulate that an intergranular lane that lives long enough would accumulate enough corks to be considered as a mesogranular border lane. Hence, in this method the intergranular lanes whose age is older than the given time t_0 are marked as mesogranular. In the two-dimensional model we are able to apply the Local Correlation Tracking algorithm to define a horizontal velocity field from the cell motions in the same way as done in the analysis of the solar observations. Hence, the second method defines mesogranules as the positive velocity divergence areas.

The histograms of mesogranule areas and lifetimes obtained with the lane age mesogranule definition are all close to exponential. The exponential lifetime distribution means that the rate at which mesogranules disappear is constant and independent of the cell lifetime. In the velocity divergence mesogranule definition two ways of obtaining the statistics are applied: the tracking and snapshot statistics. In the first method we track mesogranules in time from birth till demise, obtaining their lifetimes and lifetime-averaged areas (like in case of the statistics in the lane age mesogranule definition). The second method extracts mesogranule areas from each velocity divergence map (mesogranular image) independently. This avoids the difficulties associated with tracking of granules, but we lose the information about the lifetime of the cells. In the tracking statistics we obtain power law distributions of both mesogranule sizes and lifetimes for all model versions. The snapshot area statistics on the other hand have an exponential form. An exponential distribution of the mesogranule sizes at any given time does not imply that the distribution should also be exponential when we track the cells in time and obtain the lifetime-averaged area values (the tracking statistics). In fact, the tracking statistics results are determined by the tracking algorithm rules. The fact that for a given mesogranule definition and analysis method the mesogranulation properties are the same for the different model versions suggests that, similarly to the one-dimensional case of Chap-

ter 2, the different cell interaction rules do not differ much in the effect they have on the mesogranular-scale evolution.

Another difference between the two mesogranule definitions occurs when analyzing the dependence of the mean mesogranule size on the averaging time t_0. Both methods yield mesogranulation without an intrinsic lifetime, as the mean mesogranule lifetime increases linearly with the averaging time. Nevertheless, the mesolane method gives also no intrinsic size, while in the velocity divergence areas analysis the mean mesogranule size remains constant, independent of t_0. This result is obtained with both the tracking and the snapshot statistics; the mean mesogranule size is roughly constant with respect to t_0 for both methods. Since the particular value of the mean mesogranule size depends on the choice of the threshold level for mesogranule detection/labeling, it cannot be regarded as intrinsic. It has to be noted that the mesogranular properties also depend on the threshold definition. The time-averaged value of the rms of the divergence maps (Λ threshold, see Section 3.5.2) has a value which depends on the averaging time t_0. As t_0 increases, the amplitude of the t_0-averaged velocity divergence decreases, hence the value of Λ threshold decreases as well. Keeping the threshold value fixed for all averaging times produces a decrease of mean mesogranule size with increasing t_0. The Λ threshold definition is equivalent to those used in analysis of the solar observations (Leitzinger et al. 2005) and agrees with the intuitive understanding of the problem: when one increases t_0 and visually inspects the resulting divergence maps, the size of the positive and negative divergence patches does not change with t_0, but rather the contrast between them, since the amplitude of the divergence is decreasing.

An important difference between the model versions for the velocity divergence method can be seen in the shape of the divergence areas (mesogranules), with the cell-competition model (*CV/AL*) producing more uniform circular mesogranules that resemble the observed ones. This fact favors the cell-competition granule interaction rules as a better description of the real granule interactions than the random walk model.

It is not obvious why the LCT-velocity divergence method yields a spatial scale of mesogranulation for a given threshold level. This question is addressed in more detail in Chapter 5. The intergranular lane age method, which does not produce a threshold-time-independent spatial scale of mesogranulation, is quite a different way of analyzing the model. Even though this method is based on an analogy to the cork analysis, which is in turn equivalent to the divergence method, and a significant correlation exists in the model between the mesolanes and the velocity divergence structures for the threshold/averaging time $t_0 = 7.5 \cdot \tau_{\mathrm{av}}$, the two methods are not equivalent. The particular choice of the age inheritance rules for merging structures along with the triangular topology of the cells leads to the formation of patterns whose size, as opposed to the velocity divergence method, depends on t_0. Since the velocity divergence method is the same as used in observations to define and analyze mesogranules and can therefore be more easily compared with other results, it seems more relevant than the mesolane method.

Mesogranulation emerging from the cellular automaton model of granulation is a very robust feature of such a system. It is present for all the model versions, and in that sense does not depend on the detailed local granule interaction rules (the cell competition and random walk cellular automaton rules). Moreover, the dependence of the mesogranule mean lifetime and area on the averaging time is the same for all model versions for the given analysis method. Additionally, we show that the Trees of Fragmenting Granules

(TFGs) emerge naturally in the model where granule splitting is the main way of introducing new cells. Such TFGs have no intrinsic lifetime, with their identity (and hence lifetime and area covered on the surface) depending only on the times at which we begin and stop the observation. Another question associated with mesogranulation is the occurrence of the fragmenting granules on the surface. Having analyzed the spatial distribution of fragmenting granules in the cellular model, we do not find any tendency for those cells to appear more likely either in the divergence nor in the convergence areas. Hence, no spatial grouping of fragmenters is needed for the mesogranular pattern to appear.

Similar to the one-dimensional model presented in Chapter 2, the two-dimensional model can be recognized as class one cellular automaton, with the outcome determined regardless of the initial configuration of cells. This is partially due to the cell splitting mechanism, which prevents the cells from growing indiscriminately in the versions of the model where the splitting is based on the cell properties (A, AL, and L splitting versions). Soon after the start of the model an equilibrium is reached in those versions, with the average granule size and lifetime remaining constant in time. In the random splitting case (R) the number of granules that split per timestep is equal to the number of cells that disappeared by dissolving in this timestep. Each cell has an equal probability of being split, and the number of such events per timestep is sufficient to split all granules before they get too large. This results in the average size and lifetime of cells being close to constant in time in the random splitting versions of the model as well.

4 Three-dimensional hydrodynamical simulation results

In this chapter we present mesogranulation results obtained from a three-dimensional hydrodynamical (HD) simulation of the solar photospheric region (MURaM code). It is a compressible MHD code incorporating the radiative transfer equations and partial ionization effects under the assumption of local thermal equilibrium (Vögler 2003 PhD thesis, Vögler et al. 2005). The simulation domain size is $24 \times 24 \times 2.3$ Mm, with periodic horizontal boundary conditions. The $\tau = 1$ level is located roughly 600 km below the top of the simulation box. The spatial resolution is 20.8 km in the horizontal and 14 in the vertical direction. The magnetic field is set to zero. The bottom boundary is open and allows for mass flow, with the specific entropy of the in- and outflows being constant over the bottom boundary. The top boundary is closed, with vanishing horizontal viscous stress. The length of the simulation is 11 hours. Figure 4.1 shows an intensity snapshot from the simulation. The advantage of using the HD simulation data is that it reproduces the three-dimensional solar granulation flow very well, therefore allowing us to perform mesogranulation analysis on a realistic dataset. If mesogranulation is a self-arrangement of granules, it should be present in the HD simulation.

We define mesogranules in the simulation as patches of positive horizontal velocity divergence, analogous to the definition used in the case of solar observations and one of the definitions assumed in the two-dimensional cellular model analysis presented in the previous chapter. Hence, we can readily compare the results obtained with this method from the cellular model and the HD simulation. From the moment of obtaining the granulation intensity timeseries the procedure is identical for both the cellular model and the HD simulation, with the same code used in both models for mesogranulation analysis. The intensity images produced in the HD simulation have the cadence of 30 sec. The first step is to apply the Local Correlation Tracking (LCT) algorithm which extracts the velocity field from the granular motions (developed and described by Welsh et al. 2004). Then, we average the velocity field over a given averaging time t_0 and calculate the velocity divergence of such a t_0-averaged field. Next, mesogranules are identified as the patches of positive divergence (horizontal outflows). To produce a timeseries of mesogranulation images, we apply the same threshold for mesogranule labelling as in the cellular model. The threshold is a fraction (0.5) of a time-averaged root mean square value of the velocity divergence maps (see Section 3.5.2). As in the cellular model, we analyze mesogranule properties in two ways, producing the tracking and snapshot mesogranule statistics. For the tracking method, the individual mesogranules are tracked in time and both the lifetime and the lifetime-averaged area of mesogranules are extracted. In the snapshot
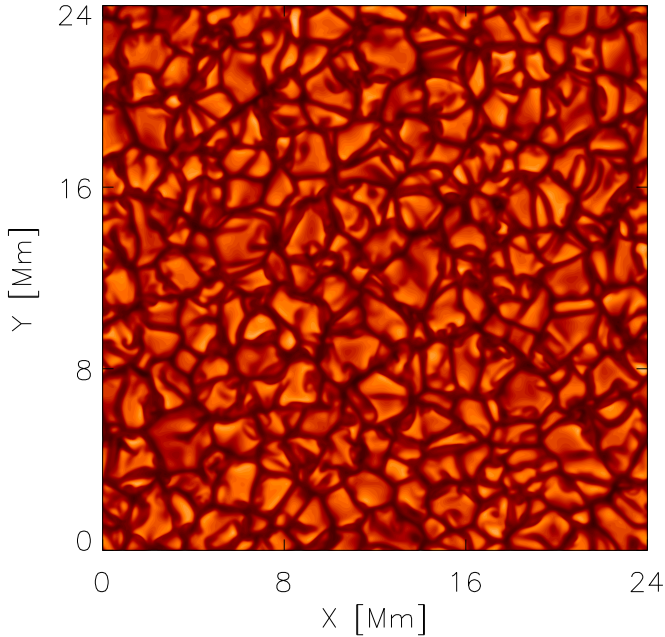
Figure 4.1: Example of a intensity snapshot from the simulation with the MURaM code. Brighter hot plasma upflows in the cell centers (granules) and flows back into the interior in the darker intergranular lanes.

method mesogranule areas are extracted from each of the t_0-averaged velocity divergence maps (mesogranule images) independently. The timescale of mesogranulation persistence in the snapshot method is given by the decay time of the coefficient of cross-correlation between the subsequent mesogranular images (see section 3.5.2).

4.1   Velocity divergence field

Fig. 4.2 presents an example of the LCT-velocity divergence image for the averaging time $t_0 = 60$ min obtained from the HD simulation. Figure. 4.3 shows an example of mesogranules present in the simulation (divergence patches lying above the threshold of 0.5Λ, see Section 3.5.2) for an averaging time of $t_0 = 60$ min.
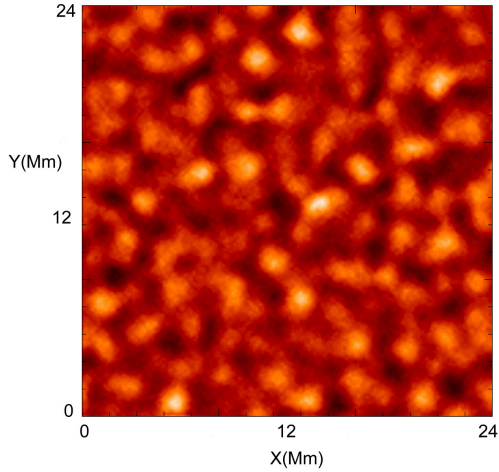
Figure 4.2: The LCT-velocity divergence map obtained from the HD simulation for the averaging time $t_0 = 60$ min.
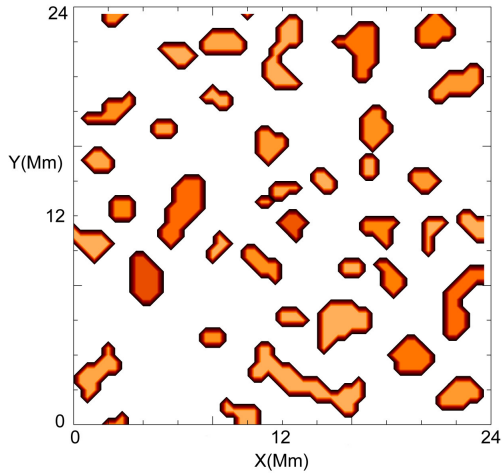
Figure 4.3: Example of the velocity divergence patches (mesogranules) lying above the 0.5Λ threshold in the HD simulation, the averaging time t_0 equals 60 min.

109

The velocity divergence field in the HD simulation (Fig. 4.2) is very similar to that obtained from the *CV/AL* model (Fig. 3.16 right, Fig. 3.21 top). To further investigate the structure of the divergence maps in both models we present in Fig. 4.4 plots of average mesogranule size (obtained with the snapshot method for a fixed averaging time of 1 hour) versus the rms threshold value for both models.
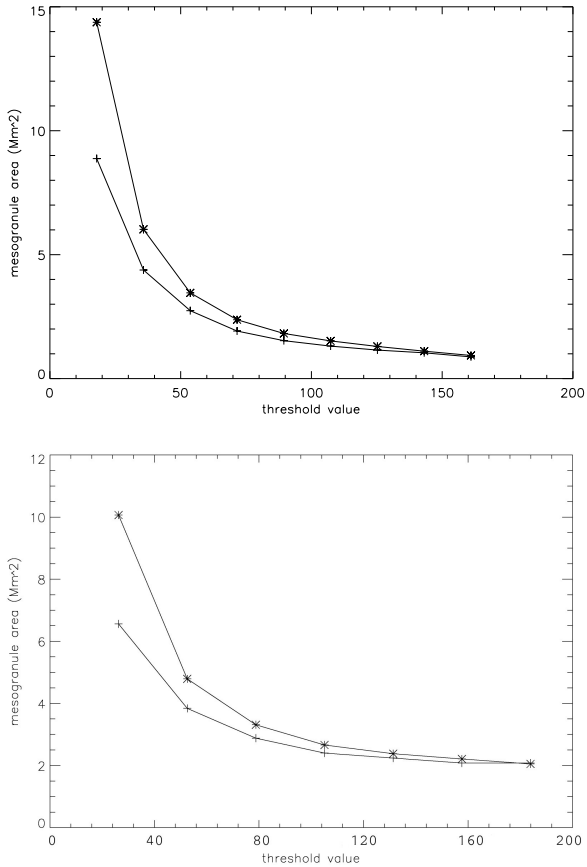
Figure 4.4: Mean (asterisks) and median (crosses) mesogranule area versus the threshold value for the *CV/AL* cellular model (top) and HD simulation (bottom).

The behavior of the curves in Fig. 4.4 is very much the same, indicating that the structure of the velocity divergence field (hence mesogranulation) produced by the *CV/AL* cellular model is similar to that in the realistic HD simulation.

4.1.1 Local Correlation Tracking (LCT) velocity versus plasma velocity

The velocity field, in case of solar observations, is usually obtained with a LCT algorithm, which tracks intensity patterns on the surface. As such, it is not obvious that the velocity field obtained in such way should correspond to the actual plasma flow velocities in the granules. Using data from the MURaM hydrodynamical simulation of the solar photospheric region, we show that this is indeed the case, and the LCT velocity approximates well the real velocity field, averaged spatially over the LCT tracking window. Figure. 4.5 presents the cross correlation between the two velocity divergence fields: one is the LCT velocity divergence, the other the divergence of the actual plasma velocity averaged spatially over the LCT window size. The cross correlation coefficient equals 0.8. Figure. 4.6 shows the LCT velocity divergence field overplotted with contours of the divergence of the real velocity averaged spatially over the LCT window size. One can see that the correspondence of the two velocity divergence fields is quite good.
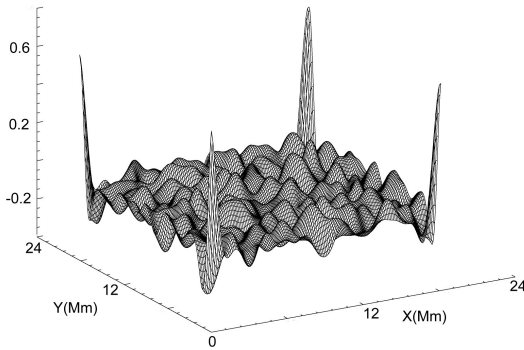
Figure 4.5: The function of cross correlation between the LCT-velocity divergence field and the real velocity divergence field averaged spatially over the LCT window size. The correlation coefficient equals 0.8.
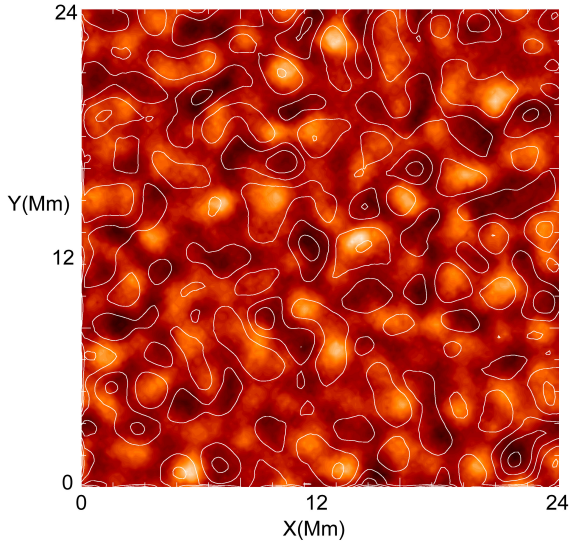
Figure 4.6: The LCT velocity divergence field overplotted with the contours of the divergence of the real velocity averaged spatially over the LCT window size.

4.2   Mesogranule tracking statistics

In this section we present mesogranule properties obtained from the HD simulation using the tracking method. Mesogranules are tracked in time in the same way as in the cellular model (see section 3.5.1). Figure. 4.7 shows the mesogranule properties for the averaging time $t_0 = 60$ min, while Fig. 4.8 shows the power law fits to the lifetime and area distributions. Like in case of the cellular models, all features smaller than 0.66 of the average granule area were removed from the mesogranular images (Fig. 4.3).   Similarly to the cellular model, the mesogranule lifetime and size histograms in the HD simulation obey a power law, with the exponents -1.21 and -2.43, respectively. Hence, the same conclusion can be drawn, that for a given averaging time t_0 mesogranulation present in the simulation has no characteristic scales. Comparing mesogranule properties in Figs. 4.7- 4.8 with those obtained from the cellular model (Fig. 3.39-3.44) it is difficult to distinguish between them, the characteristics are very similar.
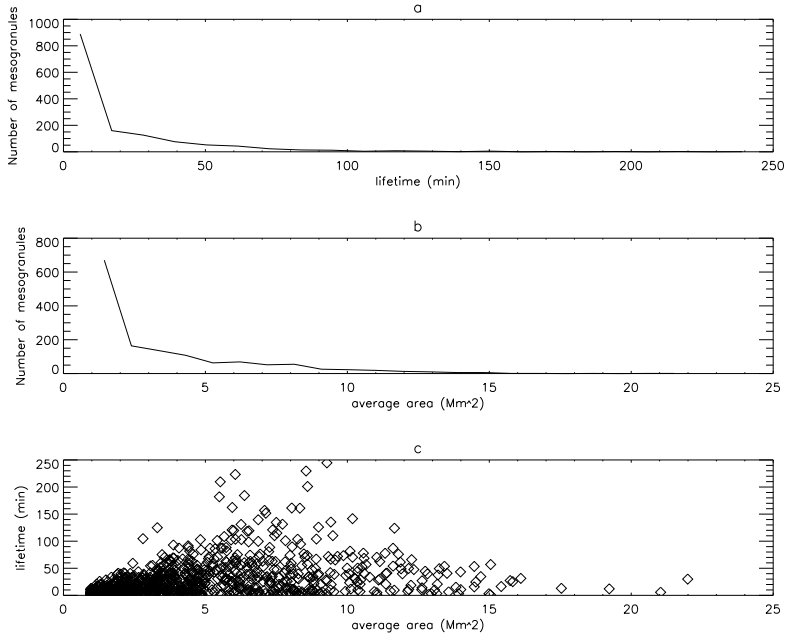
Figure 4.7: Mesogranule lifetime (a) and area (b) histograms, (c) is a scatter plot of size versus lifetime. The averaging time t_0 equals 60 min.
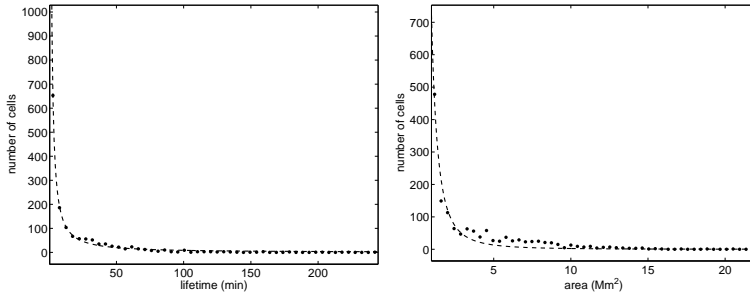
Figure 4.8: Mesogranule lifetime and size histograms from Fig. 4.7 (CV/AL model) with a power law fit. The power law exponents are -1.21 for lifetime and -2.43 for the area.

113

4.2.1   Dependence on the averaging time

The following Figures 4.9-4.10 present the dependence of mesogranule properties in the HD simulation on the averaging time t_0.
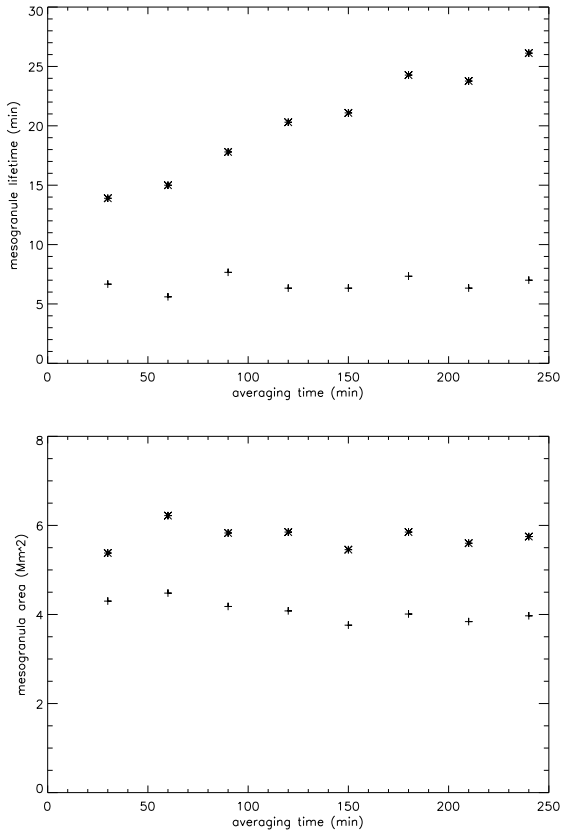
Figure 4.9: The dependence of the mean (asterisks) and median (crosses) mesogranule lifetime (top) and area (bottom) on the averaging time t_0.
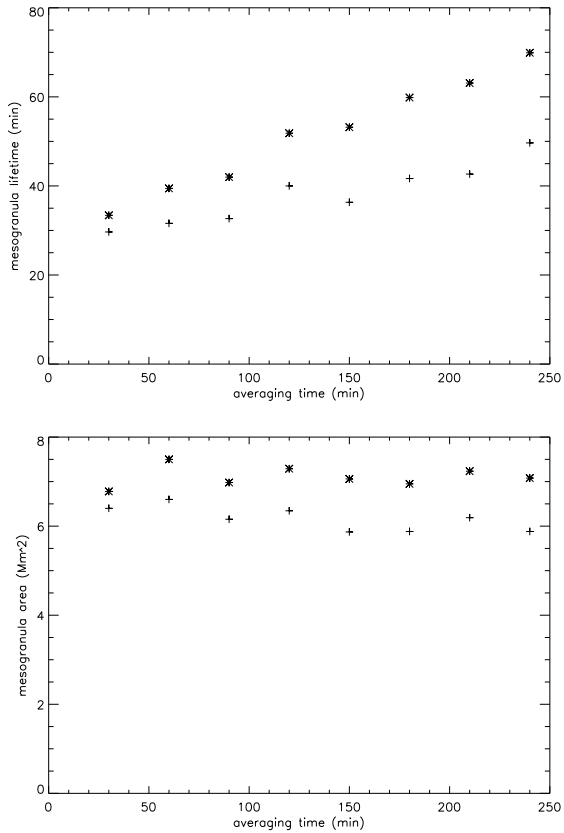
Figure 4.10: The dependence of the mean (asterisks) and median (crosses) mesogranule lifetime (top) and area (bottom) on the averaging time t_0. Only mesogranules larger than two mean granule areas and living longer than two average granule lifetimes are included.

Like in case of the cellular models (Fig. 3.45-3.52), the tracking analysis of mesogranulation dependence on the averaging time t_0 reveals no intrinsic scales of the phenomenon. The mean mesogranule lifetime increases linearly with t_0, while the mean size does not depend on the choice of t_0 (nevertheless, it depends on the choice of the threshold level value). The same is true when only mesogranules larger than two mean granule areas and living longer than two mean granule lifetimes are included in the analysis (Fig. 4.10). Similarly to the cellular model, this was done to check whether the short-lived small cells, produced occasionally by the tracking algorithm, influence the behavior.

4.3   Mesogranule snapshot statistics

Figure 4.11 presents mesogranulation area histogram obtained from the HD simulation using the snapshot method. The areas of mesogranules are extracted from each divergence map separately. Like in the cellular model snapshot statistics, the histogram is exponential. For an example and explanation of the processes leading to the exponential size distribution of the divergence areas see Section 3.5.2.1.
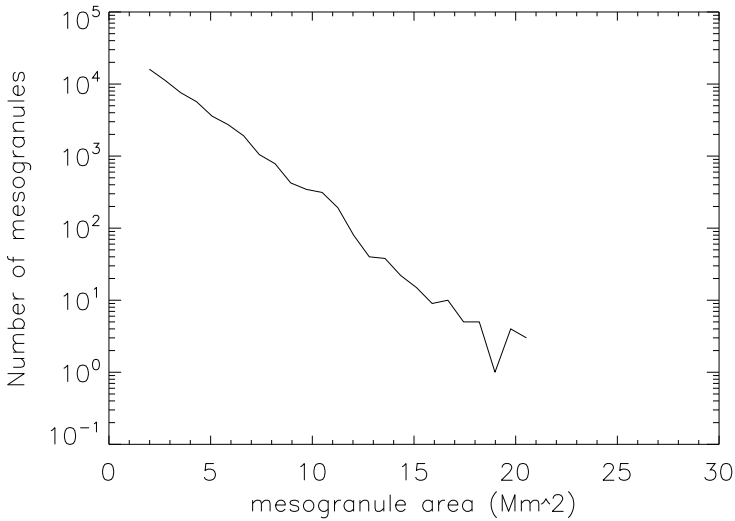
Figure 4.11: Mesogranule area histogram obtained with the snapshot method, the averaging time t_0 equals 60 min.

4.3.1   Dependence on the averaging time

Figures 4.12 presents the dependence of mesogranule properties obtained with the snapshot method on the averaging time t_0. The timescale of mesogranule persistence in the domain is given by the decay time of the cross-correlation coefficient (see section 3.5.2.2). The behavior of the curves in Fig. 4.12 is consistent with the result obtained with the track-
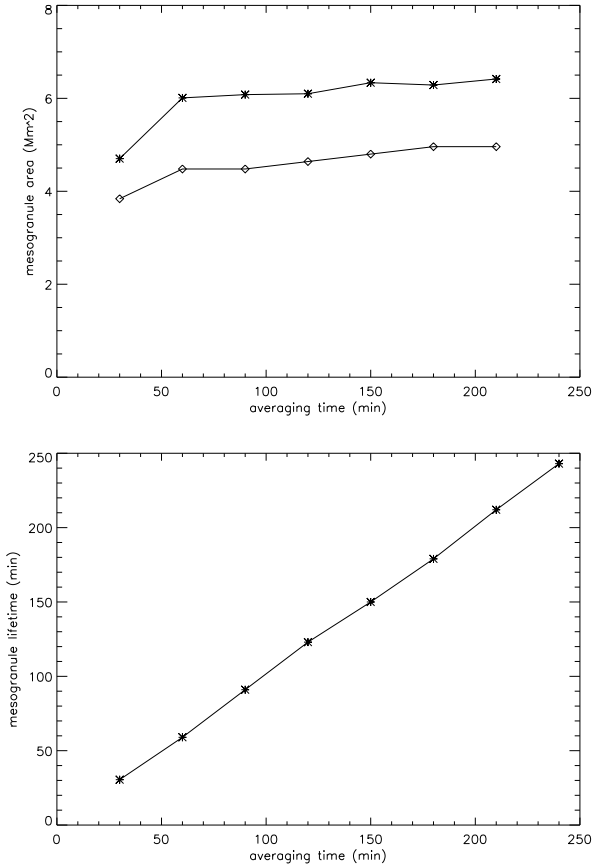
Figure 4.12: Top: the dependence of the mean (asterisks) and median (crosses) mesogranule snapshot area on the averaging time t_0. Bottom: The dependence of the cross-correlation decay time on the averaging time t_0.

ing method (Fig. 4.9-4.10) and with the corresponding results obtained from the cellular model (Fig. 3.54-3.57). The mean mesogranule size does not depend on the choice of the averaging time t_0, while the lifetime grows linearly with t_0.

4.4   Summary

We define mesogranules in the simulation as patches of positive velocity divergence, analogous to mesogranulation definition in the case of solar observations and one of the definitions assumed in the two-dimensional cellular model analysis presented in the previous chapter. The mesogranulation size and lifetime distributions obtained from the HD simulation with the tracking method obey a power law like those obtained from the cellular model. The snapshot statistics method gives exponential distribution of mesogranule areas, which was the case in the cellular model as well. Moreover, the dependence of mean mesogranule size and lifetime on the averaging time is the same in the HD simulation as it is in the cellular model. Using the same analysis methods we show that both in the HD simulation as in the cellular model the mean mesogranule lifetime increases linearly with the averaging time t_0, while the mean mesogranule area does not depend on the choice of t_0. This result is obtained with two methods of analyzing mesogranules, the tracking and the snapshot method. Hence, the properties of mesogranulation, defined as patches of positive horizontal velocity divergence, are the same in the toy model as they are in the realistic hydrodynamic simulation.

5 Spatial scale of mesogranulation

As seen in the previous chapters, the threshold method for analyzing the size of meso-granules defined as the LCT velocity divergence areas produces a mean mesogranule size that is independent of the averaging time t_0. This is true both for the two-dimensional cellular model as well as for the hydrodynamic simulation. Nevertheless, since the obtained average mesogranule size value depends on the threshold definition and value, it cannot be called intrinsic based on those results. In this chapter we present an alternative method of measuring mesogranular sizes that does not require arbitrary chosen parameters. Additionally, a more detailed analysis of the hydrodynamical simulation and the cellular model results allows for better understanding of the length scale of mesogranulation.

5.1 Autocorrelation of the velocity divergence maps

A convenient way to obtain a characteristic spatial scale of structures present in an image is to calculate the autocorrelation function of the image. Figure 5.1 shows a LCT-velocity divergence image from the hydrodynamic simulation for the averaging time $t_0 = 60$ minutes, while Fig. 5.2 shows a cut along the x and y axis of the mean autocorrelation function of the images like that in Fig. 5.1 (the function in Fig. 5.2 is an average over 600 autocorrelation functions calculated for the subsequent divergence maps in the dataset). The autocorrelation function drops from value of 1 at the center to a negative value of about -0.2. This anticorrelation can be interpreted as an indication of a regular structure present in the image: when the image is shifted by about half the spatial scale of the divergence structures, the dark convergence patches overlay the bright divergence areas, which produces the negative correlation. The distance between the minima on both sides of the correlation peak is interpreted as the typical scale of the pattern in the image. From Fig. 5.2 we conclude that the characteristic spatial scale of mesogranulation present in the 60-minute average of the LCT-velocity divergence in the hydrodynamic simulation is approximately 4 Mm. This value is the same for t_0 equal to 30, 120, 180 and 240 minutes, hence it is independent of the averaging time. This result confirms that obtained with the threshold method, that the LCT-based mesogranulation has a spatial scale independent of the averaging time. Since the autocorrelation method does not involve arbitrary values of parameters that determine the result, the obtained scale can in principle be called intrinsic. Nevertheless, in the next section we show that it is not the case, and that mesogranulation has no intrinsic scale.
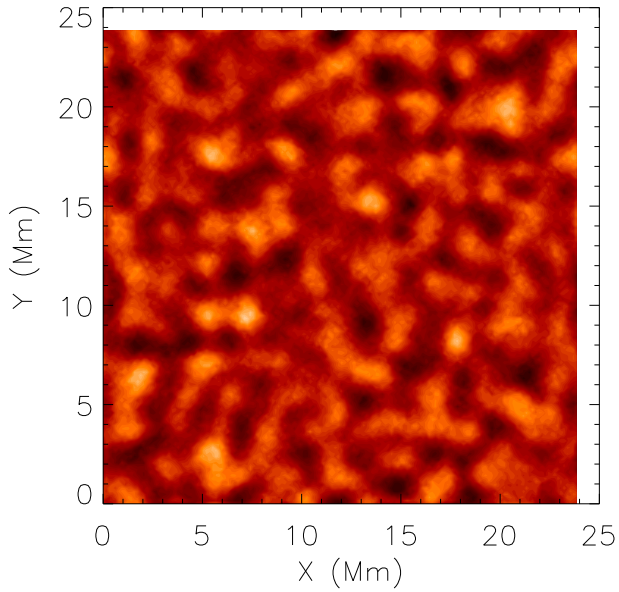
Figure 5.1: An LCT-velocity divergence image from the hydrodynamic simulation for the averaging time $t_0 = 60$ minutes
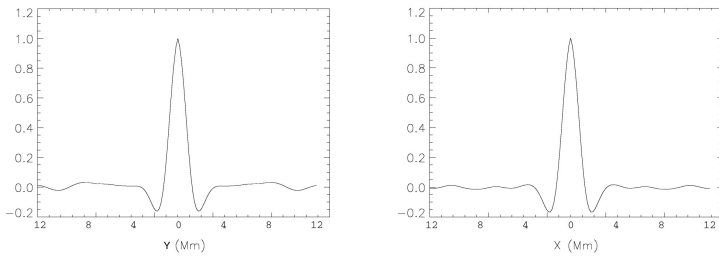
Figure 5.2: The cut along the x (left) and y (right) axis of the autocorrelation function of the image in Fig. 5.1.

5.2 The effect of spatial smoothing

The most common way of obtaining the horizontal velocities in solar observations is through the LCT algorithm. Due to its nature (tracking granule motions on the surface) the LCT method produces a spatially averaged velocity. In Section 4.1.1 we showed that the velocity field obtained with the LCT algorithm is equivalent to the actual plasma velocities smoothed spatially over the LCT tracking window. The choice of the LCT tracking window is constrained by the requirements of tracking individual granules: if the window is too small or too large the method does not work properly, producing no reliable velocity results. Nevertheless, in the hydrodynamical simulations one is free to use the real velocities and apply different spatial smoothing to see the effect it has on the mesogranulation scale. Figure 5.3 shows a 60 minute average of the actual horizontal velocity divergence (no spatial smoothing), while Fig. 5.4 shows the x-axis cut of the mean autocorrelation function of the images like that in Fig. 5.3 (an average over 600 autocorrelation functions of subsequent velocity divergence images in the timeseries). The spatial scale indicated by Fig. 5.4 is about 2 Mm. This is the granulation scale, the same as obtained from autocorrelation of intensity images (both instantaneous and time averaged). Hence, time averaging alone does not produce any length scales in the velocity divergence images other than the granular one.
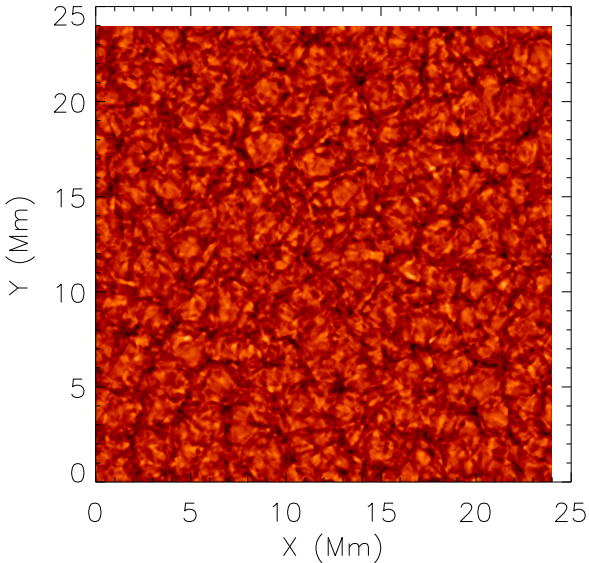
Figure 5.3: An actual plasma velocity divergence map from the hydrodynamic simulation for the averaging time $t_0 = 60$ minutes
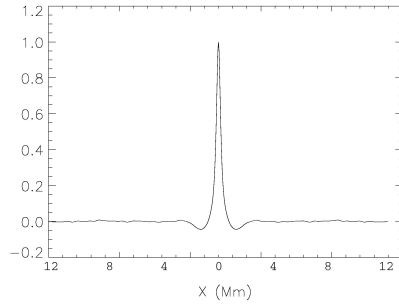
Figure 5.4: The cut along the *x* axis of the autocorrelation function of the image in Fig. 5.3.

Figures 5.5 and 5.6 show the actual plasma velocity divergence averaged over the LCT window size (a Gaussian with FWHM equal 1 Mm) and the corresponding average auto-correlation function, respectively. As expected, this produces the same mesogranulation scale of ∼ 4 Mm as present in the LCT data (Figures 5.1 and 5.2). Averaging the actual plasma velocities over larger windows produces larger mesogranular scales, as evident from Figs. 5.7 and 5.8 (window size is a Gaussian with FWHM equal 2 Mm, resulting mesogranular scale is ∼ 7 Mm) and Figs. 5.9 and 5.10 (window size is a Gaussian with FWHM equal 3 Mm, resulting mesogranular scale is ∼ 9 Mm). Hence, mesogranulation has no intrinsic spatial scale, its size depends on the spatial smoothing parameters.
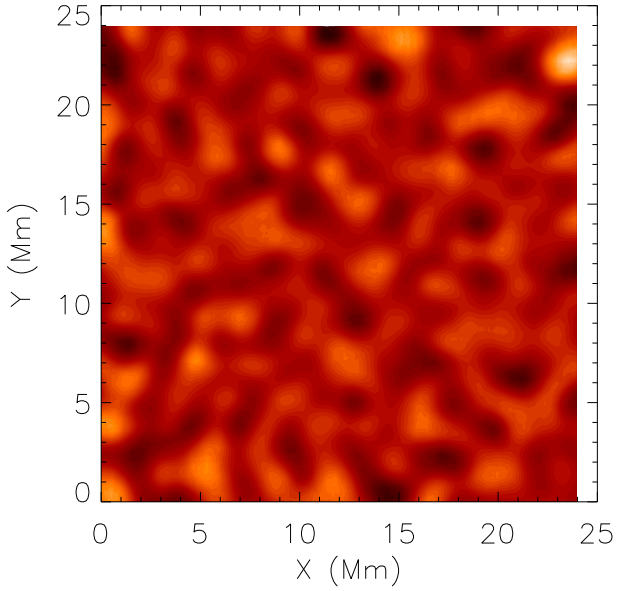
Figure 5.5: An actual plasma velocity divergence averaged over the LCT window size (1 Mm), from the hydrodynamic simulation for the averaging time $t_0 = 60$ minutes
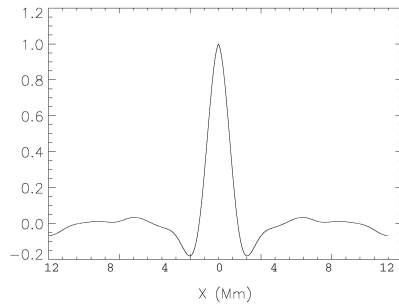
Figure 5.6: The cut along the x axis of the autocorrelation function of the image in Fig. 5.5.
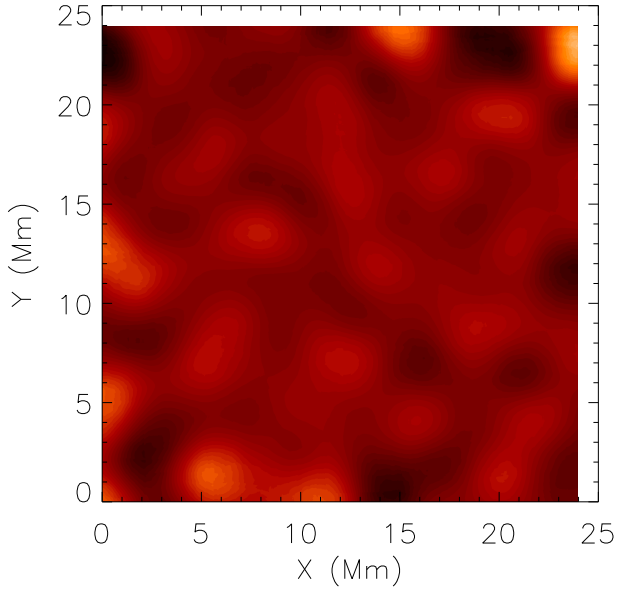
Figure 5.7: An actual plasma velocity divergence averaged over twice the LCT window size (2 Mm), from the hydrodynamic simulation for the averaging time $t_0 = 60$ minutes
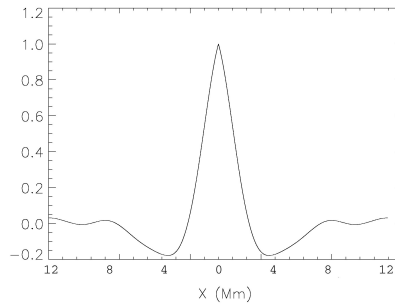
Figure 5.8: The cut along the x axis of the autocorrelation function of the image in Fig. 5.7.
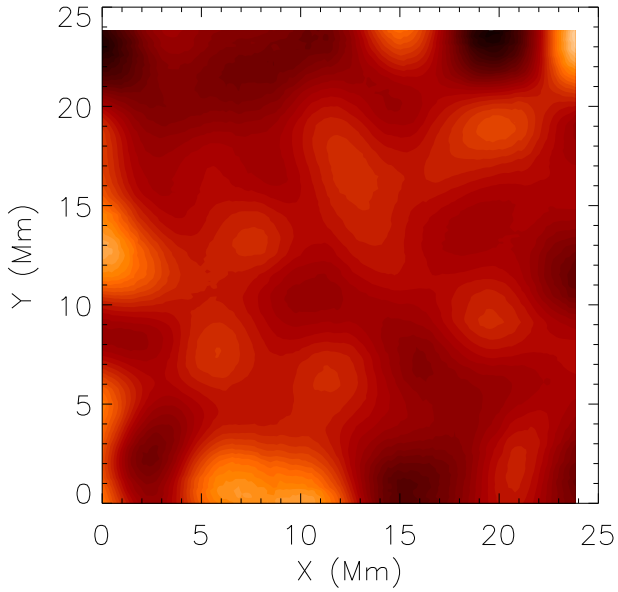
Figure 5.9: An actual plasma velocity divergence averaged over three times the LCT window size (3 Mm), from the hydrodynamic simulation for the averaging time $t_0 = 60$ minutes
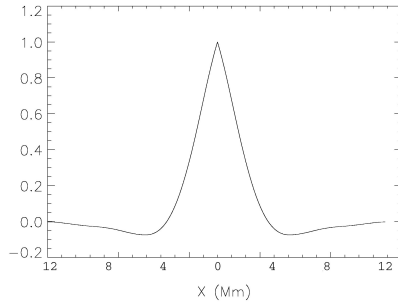
Figure 5.10: The cut along the x axis of the autocorrelation function of the image in Fig. 5.9.

125
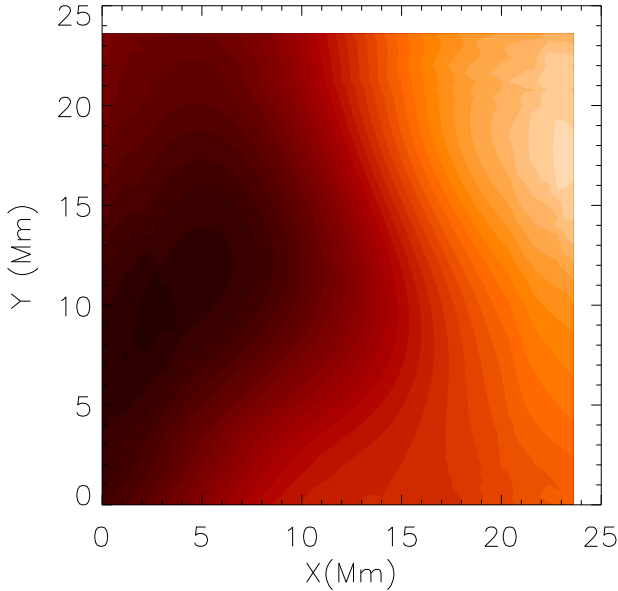
Figure 5.11: An actual plasma velocity divergence averaged over a 10 Mm window size, from the hydrodynamic simulation for the averaging time $t_0 = 60$ minutes

The dependence of the mean mesogranule area on the horizontal velocity smoothing window is not linear, as seen in Fig. 5.12. Nevertheless, if instead of the area one plots the dependence of the length scale on the smoothing window, the function is almost linear. Increasing the averaging window decreases the rms value of the divergence maps until they become almost uniform. At the same time the size of the divergence patches increases and their number decreases until for the smoothing window size of 10 Mm and more the divergence structures are of the size of the domain box (see Fig. 5.11).

In the previous chapters we have seen that for a given spatial smoothing window the mean mesogranule size is independent of the velocity averaging time t_0, which affects the mean mesogranule lifetime only. It is interesting to see if, for a given averaging time t_0, the mean mesogranule lifetime depends on the spatial smoothing window. This is indeed the case. Figure 5.13 shows how the mean mesogranule lifetime changes with the spatial smoothing window size. It has to be noted that increasing the smoothing window size decreases the number of mesogranules in the domain at almost an exponential rate, as seen in Fig. 5.14. The data used in the analysis of the dependence of the mean mesogranule area and lifetime on the smoothing window size (Figs. 5.13 and 5.12) is a timeseries of the LCT horizontal velocity divergence from the hydrodynamical simulation for $t_0 = 60$ minutes. The mesogranule properties were extracted using the same tracking statistics

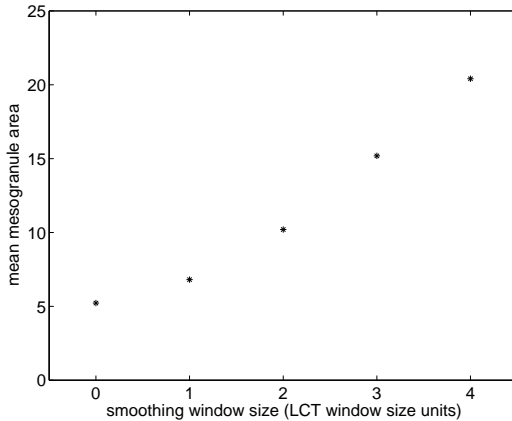method as described in Chapters 3 and 4.
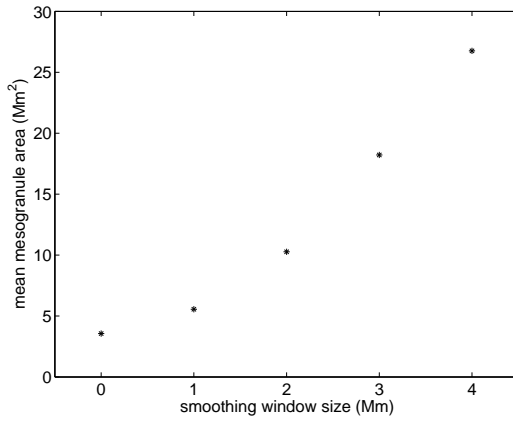
Figure 5.12: The dependence of the mean mesogranule area on the spatial smoothing window size in the HD simulation.
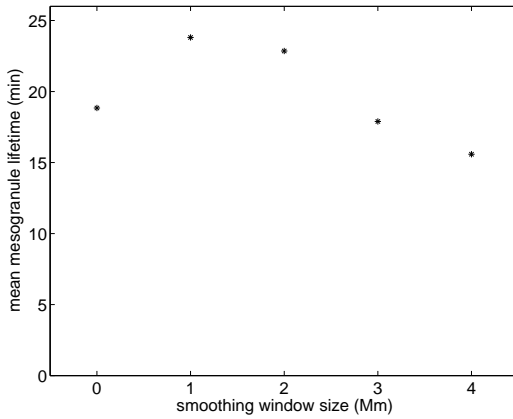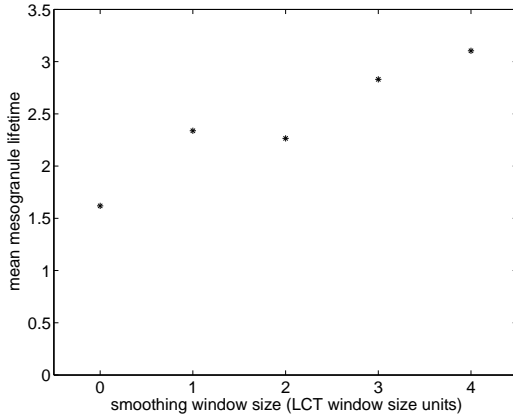

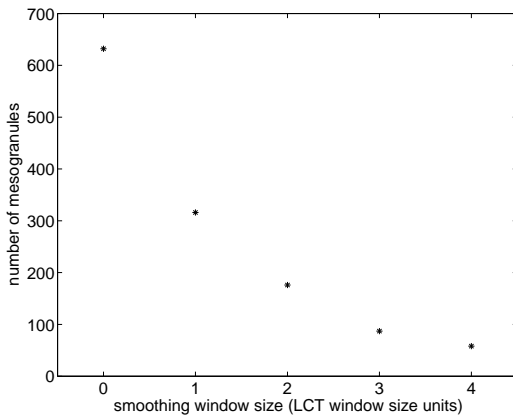Figure 5.13: The dependence of the mean mesogranule lifetime on the spatial smoothing window size in the HD simulation.
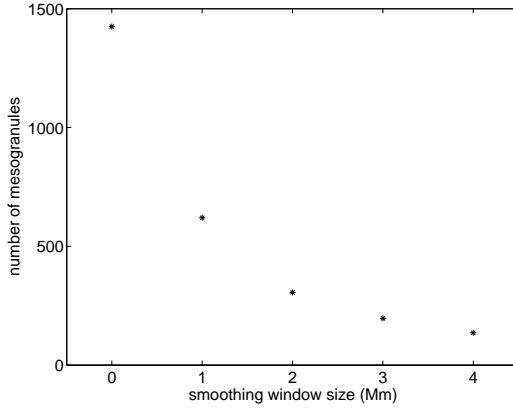
Figure 5.14: The decrease of the number of mesogranules with the spatial smoothing window size in the HD simulation.

Concluding, mesogranulation has a time scale which depends both on the velocity averaging time and spatial smoothing window, and a spatial scale that depends only on the spatial smoothing window.

5.3   Cellular model results

The autocorrelation method of determining the mesogranular spatial scale for mesogranulation defined as the velocity divergence patches is applicable also to the cellular model results. Figure 5.15 shows a LCT velocity divergence map for the averaging time $t_0 = 7.5 \cdot \tau_{av}$ (~1 hour) for the *CV/AL* model version, while Fig. 5.16 shows a cut along the x-axis of the corresponding average autocorrelation function. The scale of mesogranulation obtained from Fig. 5.16 is roughly four times the granular scale in the model. To see the effect of spatial smoothing on the mesogranular scale in the cellular model we further smooth the LCT velocity with a gaussian with a twice the LCT window size. Figures 5.17 and 5.18 show the resulting velocity divergence field and the corresponding cut of the autocorrelation function. The spatial scale in Fig. 5.18 is roughly twice that of Fig. 5.16. Hence, the mesogranular length scale in the cellular model depends on the spatial smoothing parameters, which agrees with the hydrodynamic simulation results from the previous section.
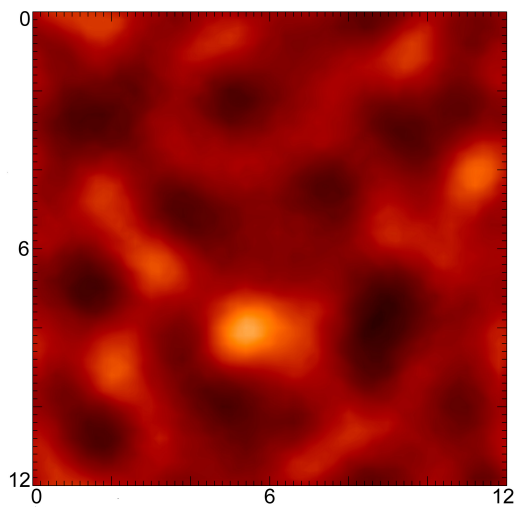
Figure 5.15: A LCT-velocity divergence map for the *CV/AL* model version, $t_0 = 7.5 \cdot \tau_{av}$ (~1 hour).
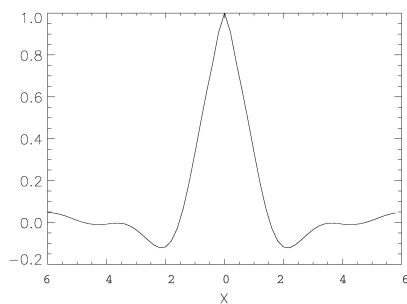
Figure 5.16: The cut along the *x* axis of the average autocorrelation function of the LCT-velocity divergence maps for the *CV/AL* model version (Fig. 5.15)
.

129
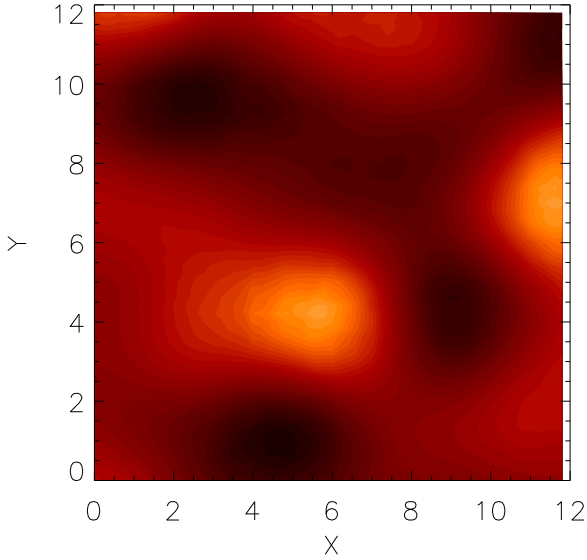
Figure 5.17: A spatially smoothed LCT-velocity divergence map for the *CV/AL* model version, $t_0 = 7.5 \cdot \tau_{av}$ (~1 hour).
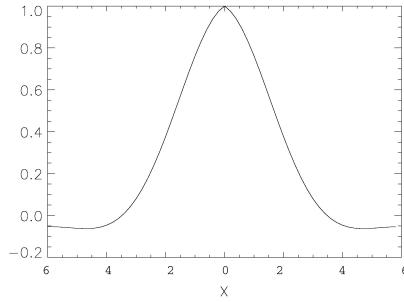
Figure 5.18: The cut along the *x* axis of the average autocorrelation function of the spatially smoothed LCT-velocity divergence maps for the *CV/AL* model version (Fig. 5.17)
.

The results presented in this section are similar for all the cellular model versions. The scale of mesogranulation in the cellular model for the LCT velocity is roughly two times the granular scale in those models, similar to the results from the hydrodynamic simulation.

The mesogranulation length scale extracted from the cellular model with the autocorrelation method does not depend on the averaging time t_0, which is in agreement with the result obtained with the threshold method and with the hydrodynamic simulation results. Figures 5.20 and 5.19 show the dependence of the mean mesogranule lifetime and area on the spatial smoothing window, extracted from the *CV/AL* model with the tracking statistics method described in Chapters 3 and 4 (the averaging time $t_0 = 7.5 \cdot \tau_{av} \approx 1$ hour). The mean mesogranule area increases with the smoothing window in a similar way as it does in the HD simulation (Fig. 5.12). The mean mesogranule lifetime also increases with the smoothing window, which differs from the HD result (Fig. 5.13). This can be caused by the fact that increasing the smoothing window dramatically decreases the number of mesogranules present in the simulation box (Fig. 5.14 for the HD simulation and Fig. 5.21 for the *CV/AL* model). Since the cell model domain size is roughly a quarter of the area of the HD simulation, the number of mesogranules for large smoothing box size is even smaller, therefore the statistics are less reliable. Hence, just like in the HD simulation, mesogranulation in the cellular model has no intrinsic scale: the time scale depends on the velocity averaging time and the spatial smoothing window size, and the spatial scale depends only on the spatial smoothing window.

Figure 5.19: The dependence of the mean mesogranule area on the spatial smoothing window size in the *CV/AL* model.

Figure 5.20: The dependence of the mean mesogranule lifetime on the spatial smoothing window size in the *CV/AL* model.

Figure 5.21: The decrease of the number of mesogranules with the spatial smoothing window size in the *CV/AL* model.

6 Comparison with observations

Leitzinger et al. (2005) analyzed a 2670-minute long dataset of 1h-averaged horizontal velocity divergence maps, applying a tracking algorithm to extract mesogranule lifetimes and lifetime-averaged areas. Only mesogranules larger than 5 Mm and living longer than 1 hour were included in the analysis. Both the lifetime and area distributions of the observed mesogranules can be approximated with an exponential. The scatter plots of mesogranular size versus lifetime are similar to those obtained from the models, with a large scatter and a slight tendency for the increase of size with the lifetime of mesogranules. The difference in the form of the area and lifetime distributions between the models and observations is most probably due to the different tracking algorithms used. The mesogranule area distributions obtained with the snapshot method (i.e, no tracking) from both the cellular model and the HD simulation are exponential. This does not imply that the tracking statistics should also be exponential. The important fact is that all the results for mesogranules defined as velocity divergence areas for a particular extraction method are the same in the cellular model and in the HD simulation. The tracking algorithm used by Leitzinger et al. (2005) differs from the one we used in the analysis and that may lead to a different form of the obtained distributions.

A feature of solar mesogranulation that is not pronounced in the cellular model is the drift of mesogranules. Apparently, mesogranules shift their spatial horizontal positions in time, and this property has been universally attributed to the advection by supergranulation (Muller et al. 1992, De Rosa & Toomre 1998), although the direction of the drift cannot always be reconciled with the supergranular flow (Leitzinger et al. 2005). The absence of supergranulation in the cellular and the HD models can explain the lack of mesogranular drift.

One of the proposed causes for the emergence of the mesogranular pattern are large long-lived downflows (Rast 2003). Nevertheless, the driving force behind such downflows and their spatial distribution remains unclear. We show that the occasional existence of long-lived downflows is the effect and not the cause of the mesogranular pattern. In the cellular model there are no downflows at all and the cells self-arrange themselves, producing patches of velocity divergence and convergence very similar to those seen in the HD simulation and solar observations. Due to the fact that those regions are spatially stable and long-lived compared to granular timescales and that the converging plasma has to sink back to the solar interior, it is very plausible that long-lived downflows form in the velocity convergence areas, fed by the mesogranular inflow. This is confirmed by the lane age method of defining mesogranulation in the cellular model: in this method mesogranules are defined as regions surrounded by long-lived cell vertices (representing downflows). Since a significant correlation exists between mesogranules defined by the two methods, one can conclude that long-lived structures (downflows) tend to exist in the

velocity convergence areas.

The role of the fragmenting granules, their spatial distribution on the surface, and their arrangement into the Trees of Fragmenting Granules (TFGs) have been the object of investigation in relation to mesogranulation (Rieutord et al. 2000, Roudier et al. 2003, Roudier et al. 2004). We have shown that mesogranulation appears without the need for the fragmenter events to be confined to particular parts of the surface. In the cellular models the fragmenter positions are distributed quite uniformly over the whole surface, with no preference of velocity divergence or convergence areas. Additionally, we show that in a cell system where the fragmentation is the main method of introducing new granules, the TFGs appear naturally and their identity depends only on the times at which the observation begins and ends. The lifetime histogram of the TFGs in the cellular model obeys a power-law distribution, similar to that reported in case of observations (Roudier et al. 2003, Roudier et al. 2004), thus confirming the conclusion of no intrinsic timescale of the TFGs.

7 Conclusions

Mesogranulation is a cellular pattern visible in the averaged velocity field of the granular flow. We have shown that mesogranulation is a property of the granular field, resulting from the self-arrangement of granules on the surface. The two-dimensional cellular automaton model, presented in Chapter 3, resembles the solar granulation properties in terms of the cell size and lifetime distributions, and the cells' mutual horizontal interaction. The cells appear, disappear, and translate on the surface much like the real granules do. We have shown that such a cell system is all that is necessary for the mesogranular pattern to appear, and no additional processes are needed.

Mesogranules on the Sun are defined as areas of the time-averaged and spatially smoothed horizontal velocity divergence. Applying the same definition in the cellular model, and extracting the velocity field in the same way as done in case of observations and hydrodynamical (HD) simulations (LCT velocities), we have shown that mesogranulation present in the cellular model has the same properties as that present in the realistic numerical simulation (Chapter 4). In both the cellular model and the simulation the size and lifetime histograms of mesogranules obtained with the tracking method for a given averaging time obey a power law. The mesogranule area distributions obtained with the snapshot method are exponential in both the simulation and the cellular model. The nature of the divergence areas and the probabilities of their disappearing lead to such exponential distributions (see Section 3.5.2.1 for simple model/explanation). Moreover, the dependence of the mean and median size and lifetime of the divergence areas (mesogranules) on the averaging time is the same in the cell model and in the HD simulation. This result is found with both the tracking and snapshot methods for obtaining the statistics. The mean lifetime of mesogranular patches increases linearly with the averaging time, suggesting no intrinsic timescale of the phenomenon. The average mesogranular size on the other hand remains constant, independent of the averaging time. In Chapter 5 we have shown that the mesogranulation length scale depends only on the spatial smoothing parameters, while the mesogranule lifetime depends on both the spatial and temporal averaging windows.

Mesogranulation emerges as a property of the granulation, only weakly depending on the detailed granule evolution rules. We tested different versions of the cellular model, with granule evolution depending on the size of the cell and its neighbors (the cell-competition scheme), or being determined by random motion of the cell's vertices. Additionally, four different cell splitting rules were tested along with the two cell interaction schemes. Mesogranulation appears in all of the resulting model versions, and has very similar properties in all versions in terms of the size and lifetime histograms and the dependence of the properties on the averaging time and spatial smoothing. The differences between the model versions can be seen in the shape of the velocity divergence patches,

with the cell-competition versions producing cellular pattern similar to that observed on the Sun and in the numerical simulations. Moreover, the dependence of the mean mesogranule size on the value of the threshold is also the same in the cell-competition cellular model and in the numerical HD simulation, additionally strengthening the similarities in the structure of the velocity divergence field in the two models. Since the cell-competition interaction rules were modelled to resemble what is assumed to be the interaction of real granules, with the pressure exerted on the intergranular lane being proportional to the cell size, this mesogranulation result indirectly confirms such granule interaction hypothesis. The difference between the shape of mesogranules emerging from the cell-competition and random models is due to the granule properties produced by the different cell interaction rules. The cell-competition models produce granulation with a well-defined 'mean' granule area: as opposed to the almost exponential-like distribution in the random versions, the area histograms in the cell-competition case peak around a certain value. Hence, a small granule in the cell-competition model is more probable to be surrounded by larger cells than it is in the random model. Accordingly, a large granule in the cell-competition models is more probable to be surrounded by smaller cells than it is in the random models. This leads in the cell-competition models to small cells diminishing and large cells spreading without as much horizontal translation of the cell as they are likely to experience in the random model versions. This in turn leads to a more stability and regularity in the resulting mesoscale pattern (which can also be verified ny the distribution of the mesovertices presented in Section 3.4.1). In particular, in the most randomized model (RV/R) there is no relation between granule size and its evolution and the resulting velocity divergence structures are least regularly shaped of all the models. Concluding, apart from the shape, all the other properties of mesogranulation emerging from granulation are consistent with noise present in such a cell system, where spatial and temporal averaging leads to emergence of larger and longer lived structures. The cell-competition rules for the granule interaction lead to the more regular shape of such structures.

Due to the fact that the interactions between the cells in the cellular model are local i.e., a cell interacts only with its direct neighbors, the model can be seen as a two-dimensional cellular automaton. Hence, mesogranulation can be interpreted as a cellular automaton effect. Granulation can be classified as a class one cellular automaton, always producing the same type of mesogranular pattern regardless of the initial configuration of granules. This is partially due to the granule splitting, which ensures that the mean granule size and lifetime remain constant in time.

A   Appendix: 2-D model results

A.1   Velocity divergence patches versus mesolanes: comparison

The following figures are equivalents of Fig. 3.18-3.20 for the *RV/AL*, *RV/A*, *CA/L* and *RV/R* versions of the model.
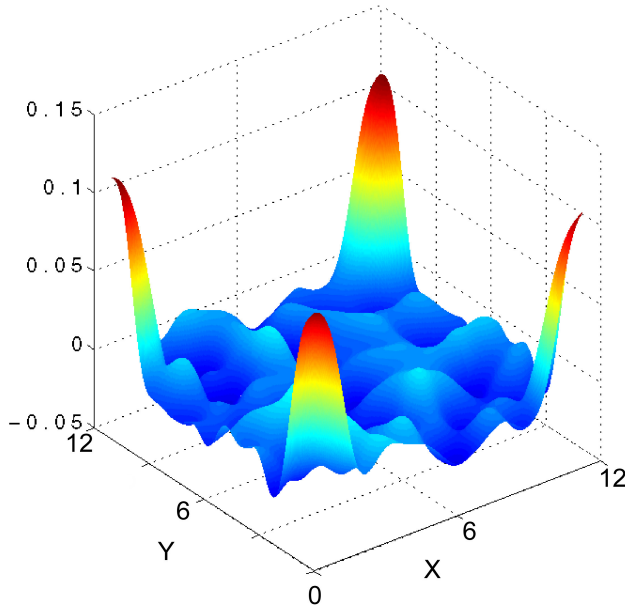
Figure A.1: Averaged cross correlation function between velocity divergence and mesofeatures for the *RV/AL* model, $t_0 = 7.5 \cdot \tau_{\mathrm{av}}$.
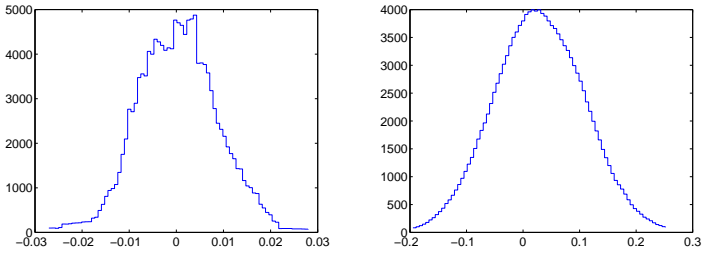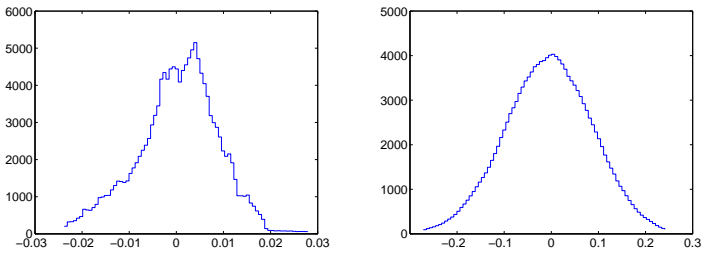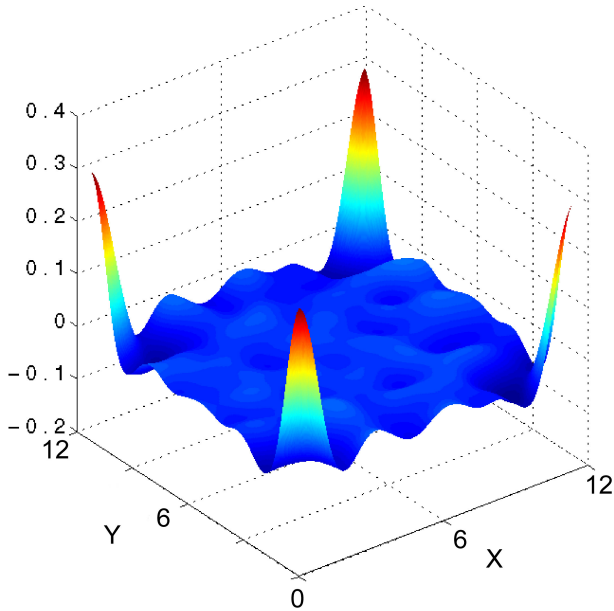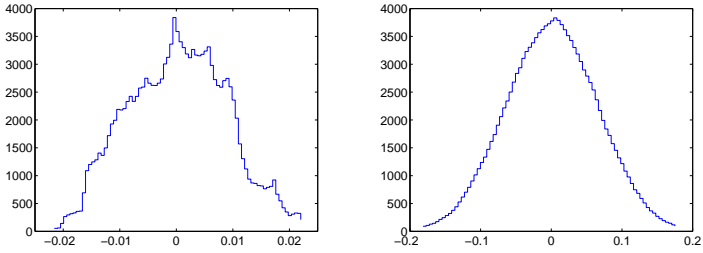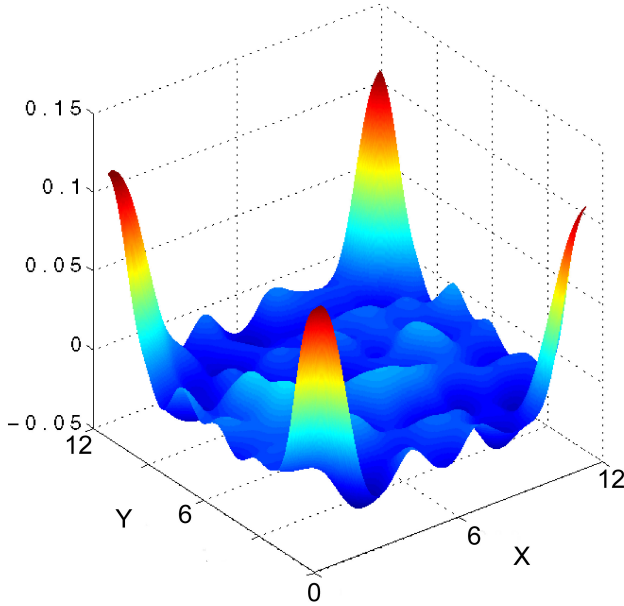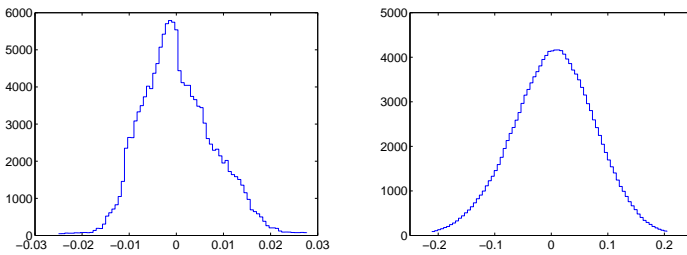
Figure A.2: (a) histogram of an average of the 63 correlation functions (b) histogram of an average of the 63 correlation function histograms, the *RV/AL* model (see text).
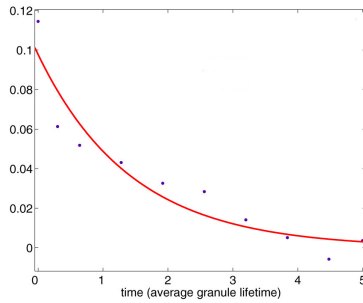
Figure A.3: Decrease of correlation between velocity divergence and mesolanes, with exponential fit. *RV/AL* model (see text). The e-folding time is $1.5 \cdot \tau_{av}$
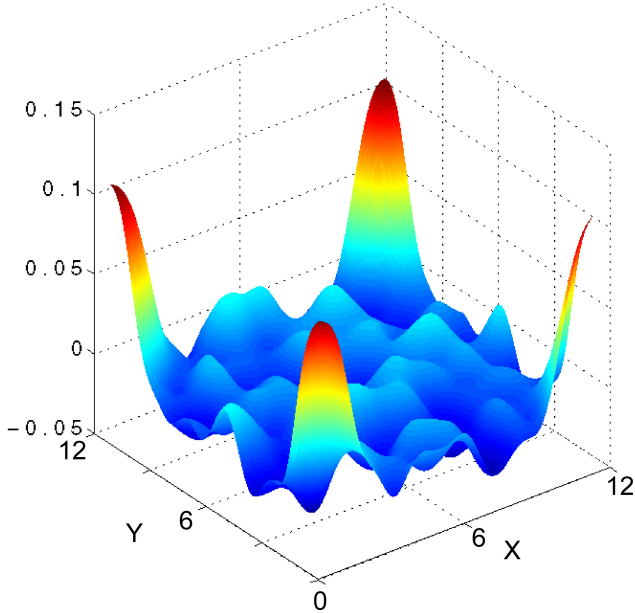
Figure A.4:   Averaged cross correlation function between velocity divergence and mesofeatures for the RV/A model, $t_0 = 7.5 \cdot \tau_{av}$.

Figure A.5: (a) histogram of an average of the 63 correlation functions (b) histogram of an average of the 63 correlation function histograms, the RV/A model (see text).
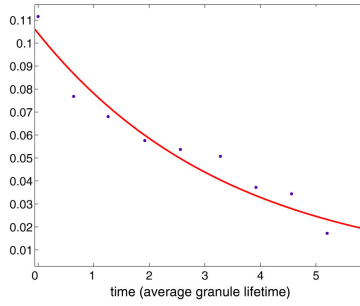
Figure A.6: Decrease of correlation between velocity divergence and mesolanes, with exponential fit. RV/A model (see text). The e-folding time is $3.6 \cdot \tau_{av}$

Figure A.7: Averaged cross correlation function between velocity divergence and mesofeatures for the CA/L model, $t_0 = 7.5 \cdot \tau_{av}$.

Figure A.8: (a) histogram of an average of the 63 correlation functions (b) histogram of an average of the 63 correlation function histograms, the CA/L model (see text).
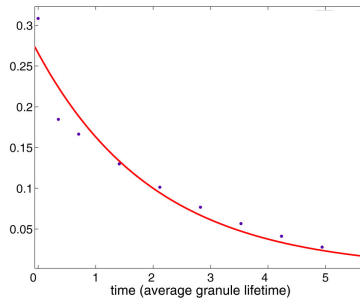
Figure A.9: Decrease of correlation between velocity divergence and mesolanes, with exponential fit. CA/L model (see text). The e-folding time is $2 \cdot \tau_{av}$

Figure A.10: Averaged cross correlation function between velocity divergence and mesofeatures for the RV/R model, $t_0 = 7.5 \cdot \tau_{\mathrm{av}}$.

Figure A.11: (a) histogram of an average of the 63 correlation functions (b) histogram of an average of the 63 correlation function histograms, the RV/R model (see text).
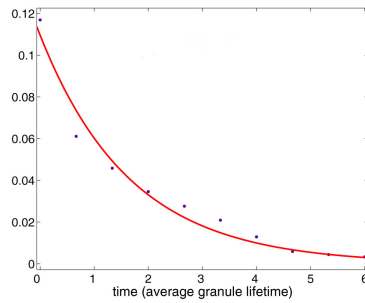
Figure A.12: Decrease of correlation between velocity divergence and mesolanes, with exponential fit. RV/R model (see text). The e-folding time is $1.6 \cdot \tau_{av}$.

A.2   Granule properties

The following figures are equivalents of Fig. 3.5-3.9 and show the granule properties for the other model versions.
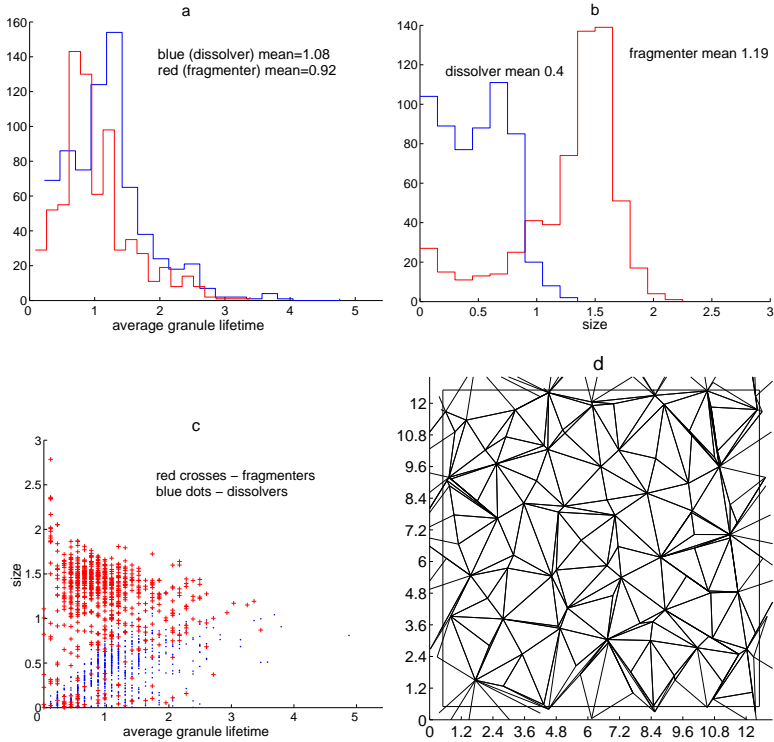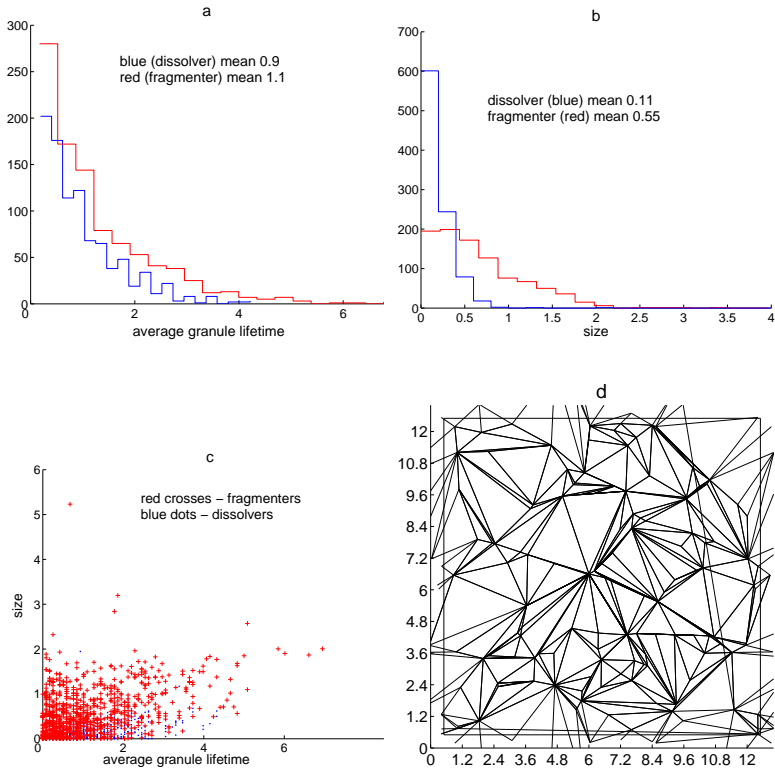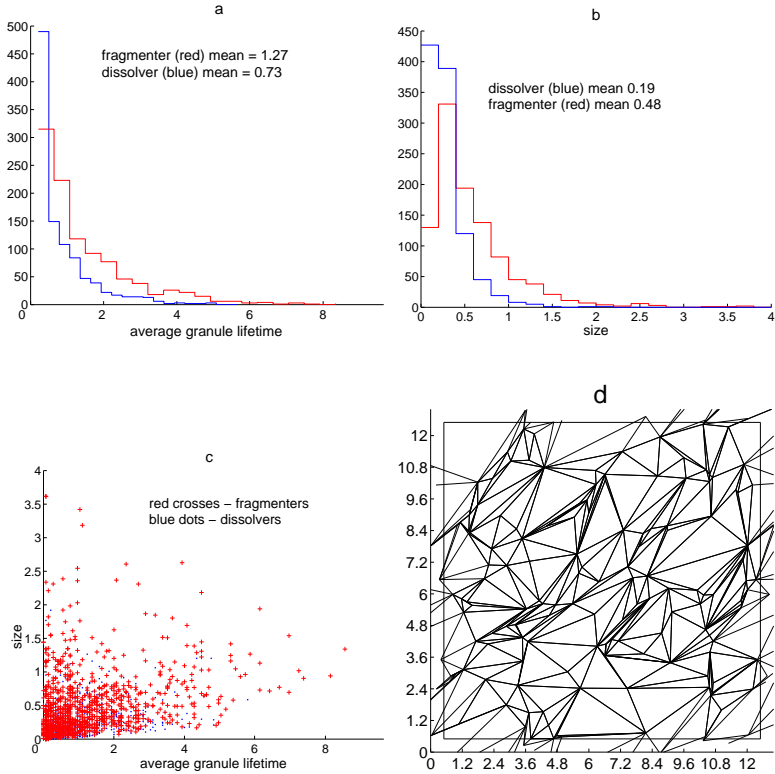

Figure A.13: (a) cell lifetime and (b) cell size distributions, (c) scatter plot of size versus lifetime and (d) domain snapshot; *CA/AL* version.
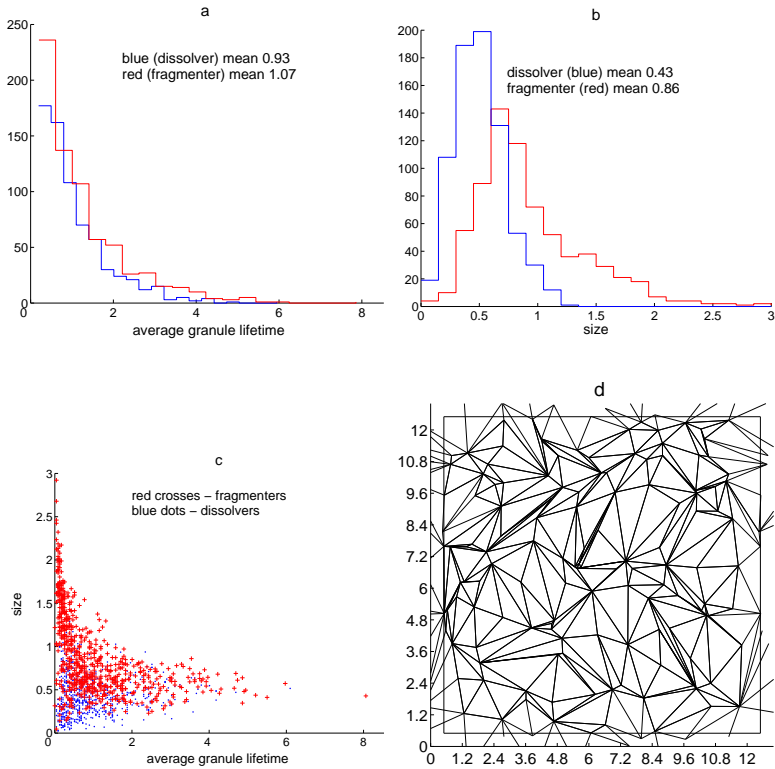
Figure A.14: (a) cell lifetime and (b) cell size distributions, (c) scatter plot of size versus lifetime and (d) domain snapshot; *RA/AL* version.
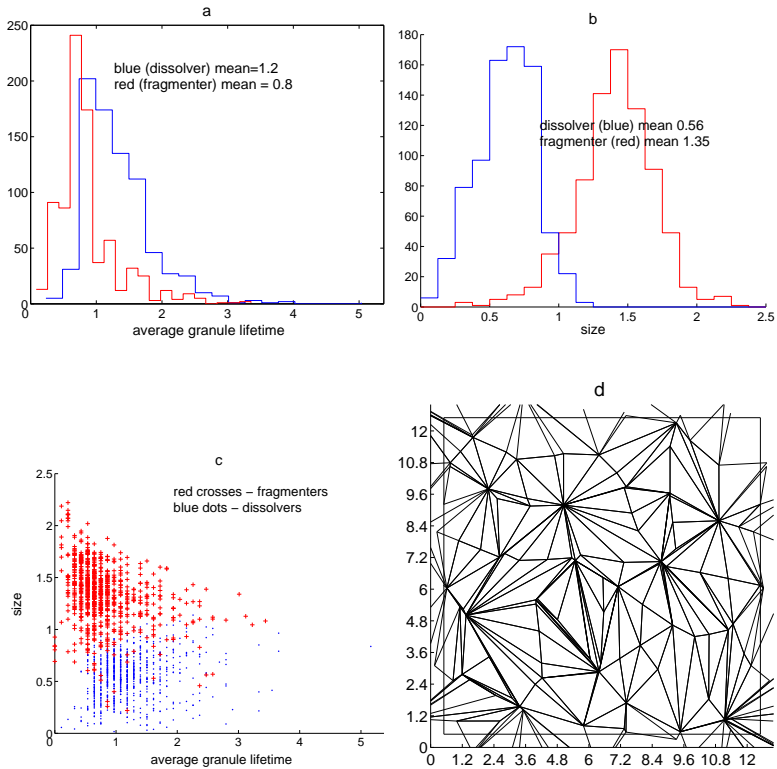
Figure A.15: (a) cell lifetime and (b) cell size distributions, (c) scatter plot of size versus lifetime and (d) domain snapshot; *CA/A* version.
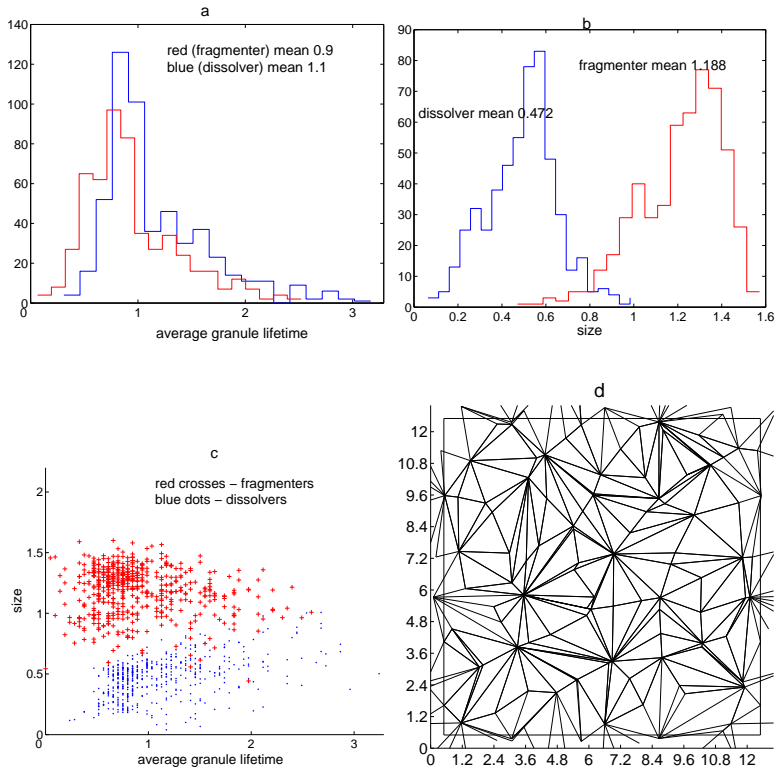
Figure A.16: (a) cell lifetime and (b) cell size distributions, (c) scatter plot of size versus lifetime and (d) domain snapshot; *CV/A* version.
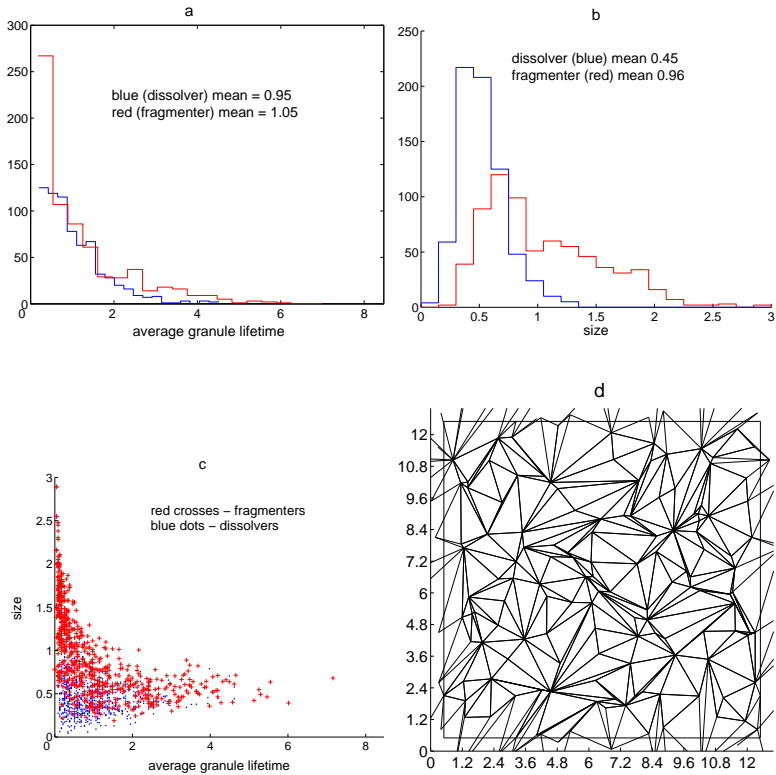
Figure A.17: (a) cell lifetime and (b) cell size distributions, (c) scatter plot of size versus lifetime and (d) domain snapshot; *RA/A* version.
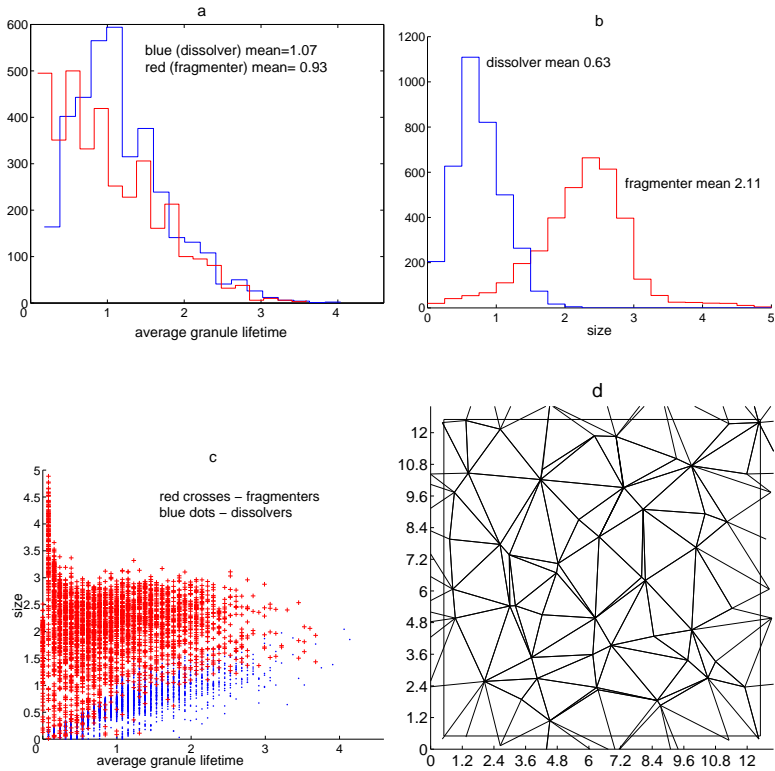
Figure A.18: (a) cell lifetime and (b) cell size distributions, (c) scatter plot of size versus lifetime and (d) domain snapshot; *CV/L* version.
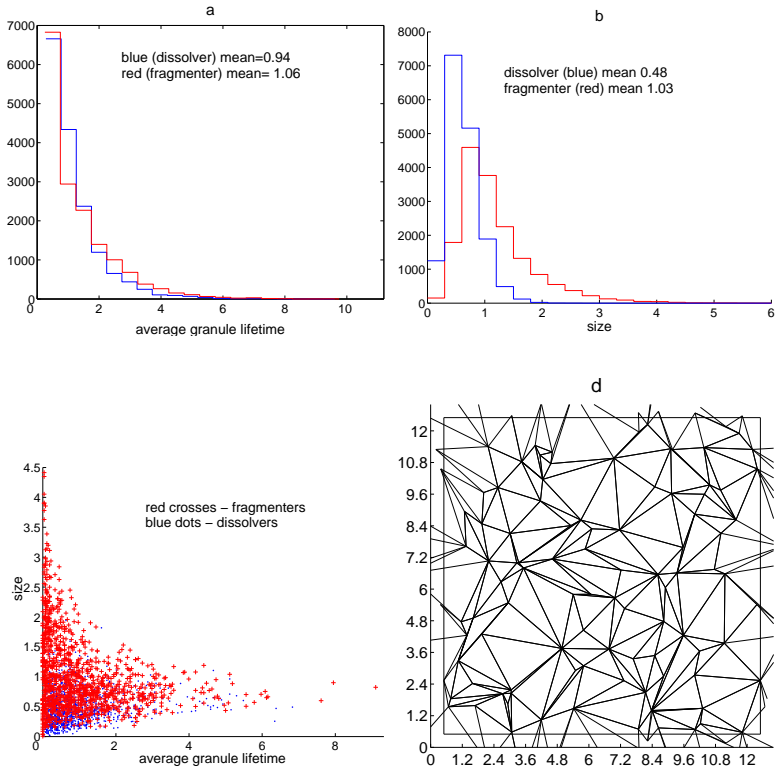
Figure A.19: (a) cell lifetime and (b) cell size distributions, (c) scatter plot of size versus lifetime and (d) domain snapshot; *RA/L* version.
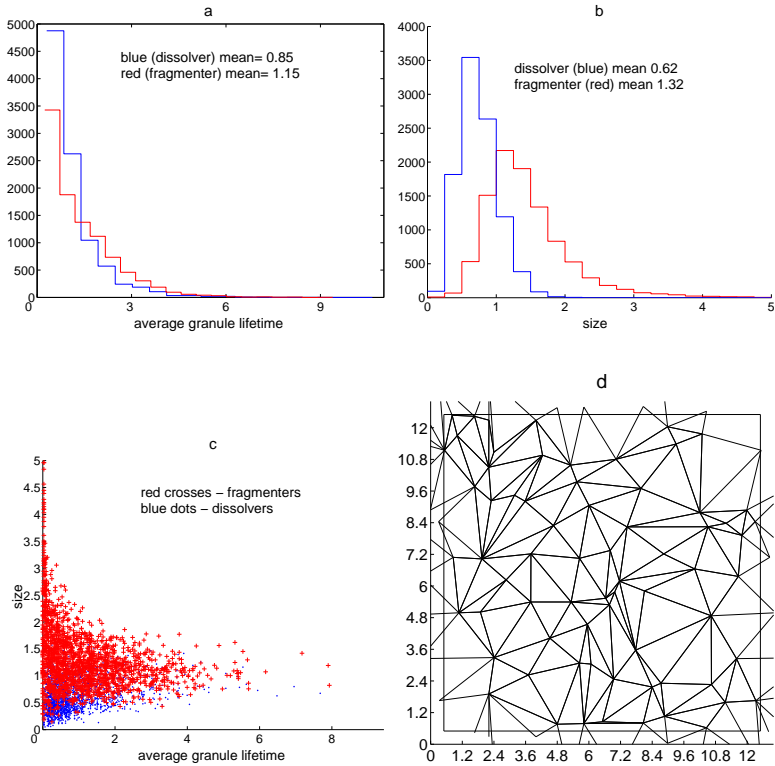
Figure A.20: (a) cell lifetime and (b) cell size distributions, (c) scatter plot of size versus lifetime and (d) domain snapshot; *RV/L* version.
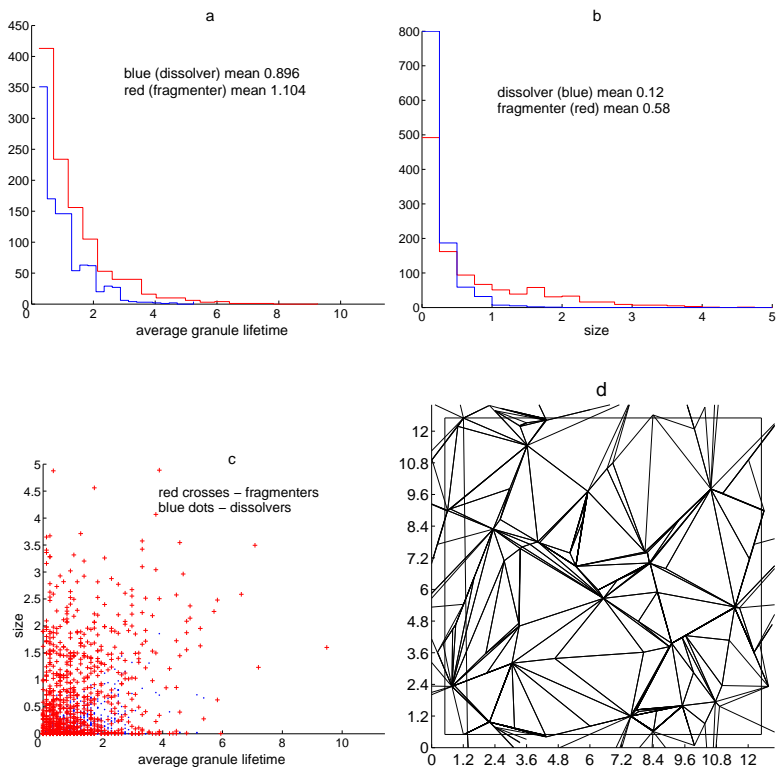
Figure A.21: (a) cell lifetime and (b) cell size distributions, (c) scatter plot of size versus lifetime and (d) domain snapshot; *CA/R* version.

Figure A.22: (a) cell lifetime and (b) cell size distributions, (c) scatter plot of size versus lifetime and (d) domain snapshot; *CV/R* version.

Figure A.23: (a) cell lifetime and (b) cell size distributions, (c) scatter plot of size versus lifetime and (d) domain snapshot; *RA/R* version.

A.3   Mesogranulation results: intergranular lane age method, S-splitting rule

Figures A.24 to A.33 show the S-splitting rule equivalents of Figures 3.26 to 3.35.
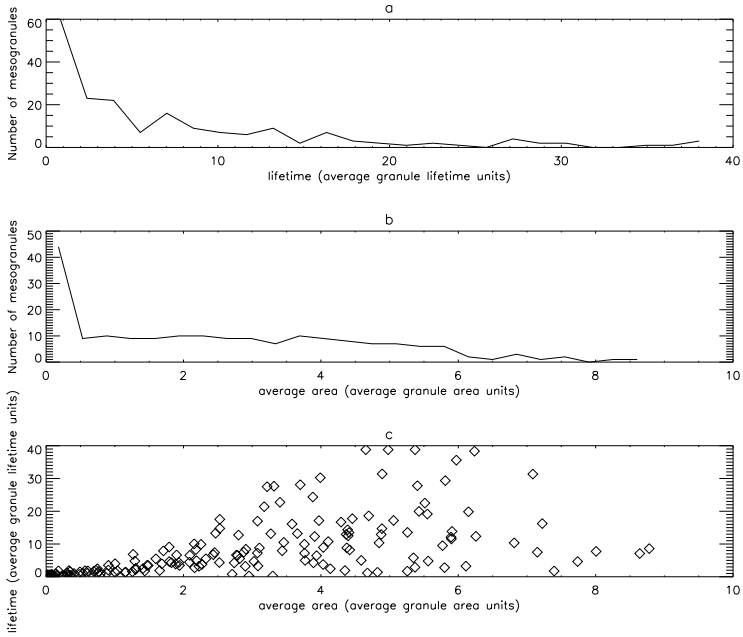
Figure A.24: Mesogranulation statistics: histograms of (a) lifetime and (b) average area, (c) is a scatter plot of size versus lifetime. *CV/AL* model, S-split.
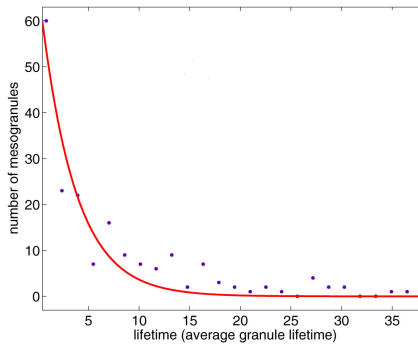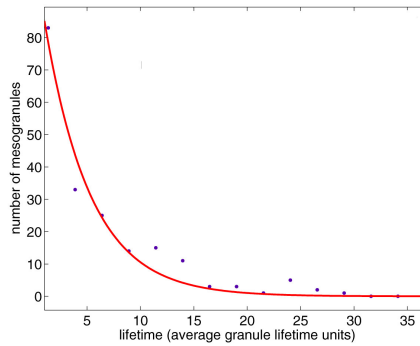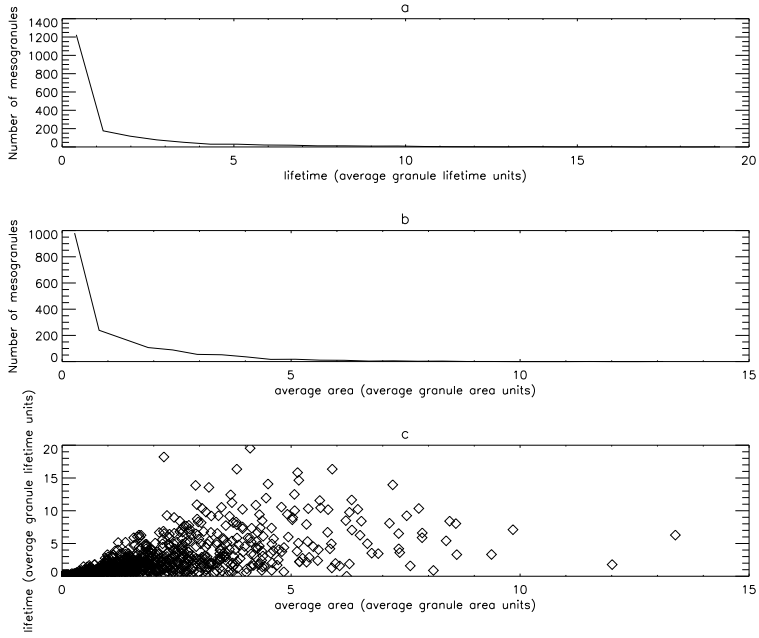

Figure A.25: Mesogranular lifetime histogram with an exponential fit. *CV/AL* model, S-split. The e-folding time equals $3.4 \cdot \tau_{\mathrm{av}}$.

155
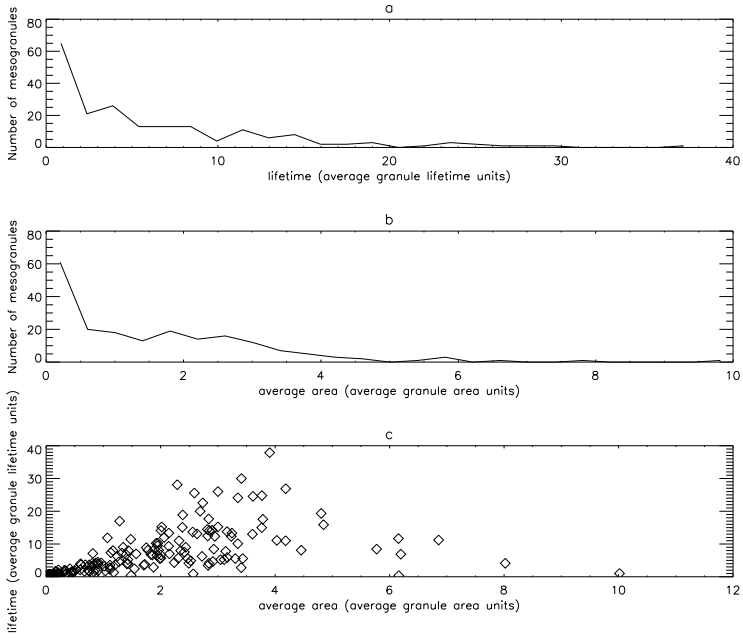
Figure A.26: Mesogranulation statistics: histograms of (a) lifetime and (b) average area, (c) is a scatter plot of size versus lifetime. CA/L model, S-split.
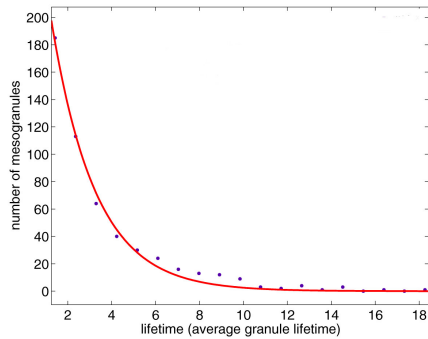

Figure A.27: Mesogranular lifetime histogram with an exponential fit. CA/L model, S-split. The e-folding time equals $4.3 \cdot \tau_{av}$.

Figure A.28: Mesogranulation statistics: histograms of (a) lifetime and (b) average area, (c) is a scatter plot of size versus lifetime. *RV/AL* model, S-split.

Figure A.29: Mesogranular lifetime histogram with an exponential fit. *RV/AL* model, S-split. The e-folding time equals $2 \cdot \tau_{av}$.
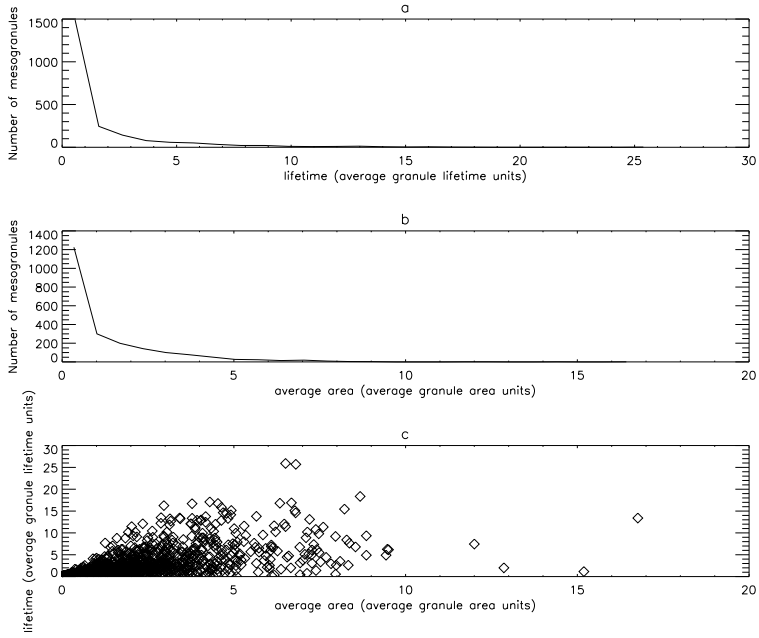
157

Figure A.30: Mesogranulation statistics: histograms of (a) lifetime and (b) average area, (c) is a scatter plot of size versus lifetime. *RV/R* model, S-split.
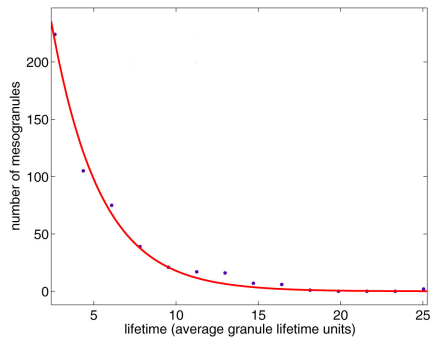

Figure A.31: Mesogranular lifetime histogram with an exponential fit. *RV/R* model, S-split. The e-folding time equals $2.9 \cdot \tau_{av}$.
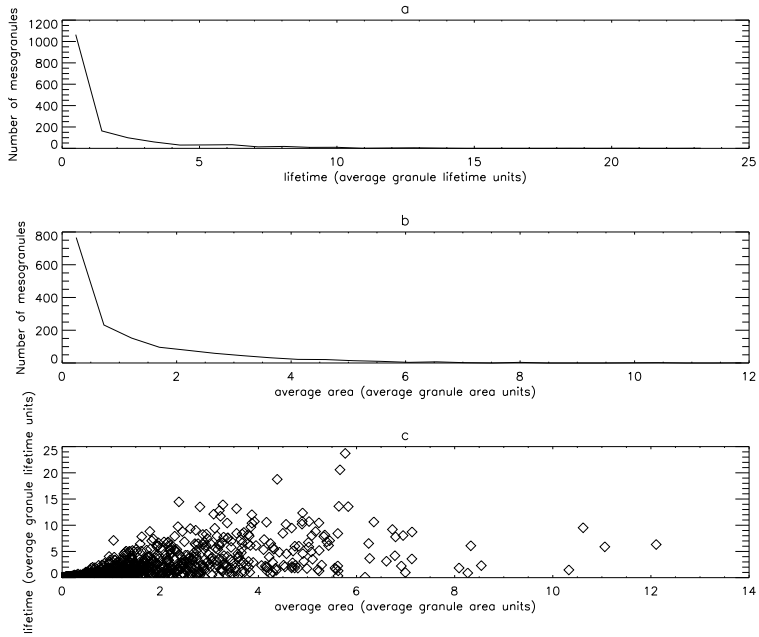
Figure A.32: Mesogranulation statistics: histograms of (a) lifetime and (b) average area, (c) is a scatter plot of size versus lifetime. *RV/A* model, S-split.
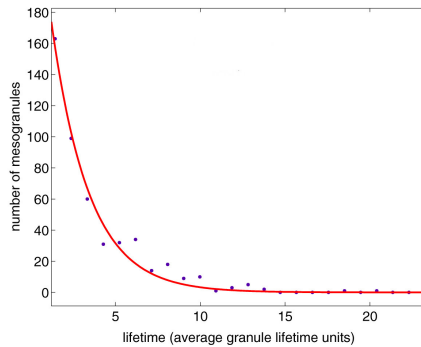

Figure A.33: Mesogranular lifetime histogram with an exponential fit. *RV/A* model, S-split. The e-folding time equals $2.2 \cdot \tau_{\mathrm{av}}$.

A.4   Mesogranulation properties: intergranular lane age method, dependence on the threshold time t_0

The following figures present the dependence of mesogranule mean (and median) size and lifetime on the threshold time t_0 obtained with the S-splitting method for the RA/R and CV/AL model versions. The "ns" means that only cells larger than $2 \cdot \text{Area}_{av}$ and living longer than $2 \cdot \tau_{av}$ were included.
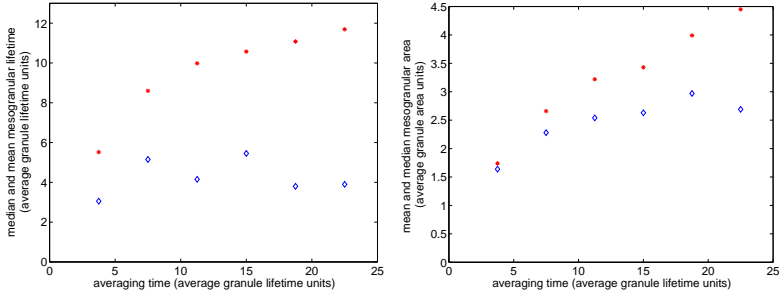

Figure A.34: Dependence of mesogranular median (diamonds) and mean (asterisks) lifetime (left) and size (right) on the threshold time. $CV/AL - S$ model.

Figure A.35: Dependence of mesogranular median (diamonds) and mean (asterisks) lifetime (left) and size (right) on the threshold time. $CV/AL - S$ ns model.

Figure A.36: Dependence of mesogranular median (diamonds) and mean (asterisks) lifetime (left) and size (right) on the threshold time. $RV/R - S$ model.
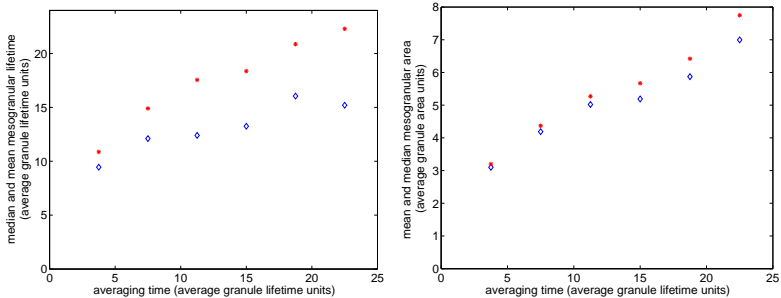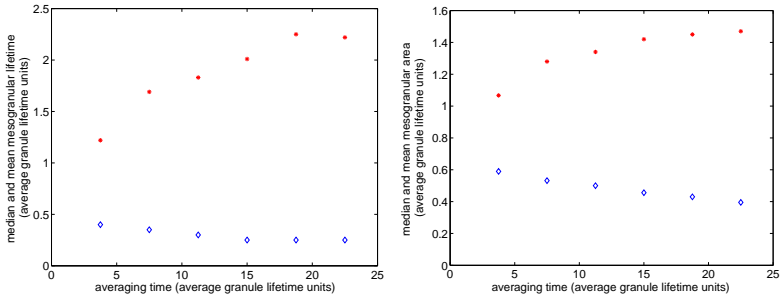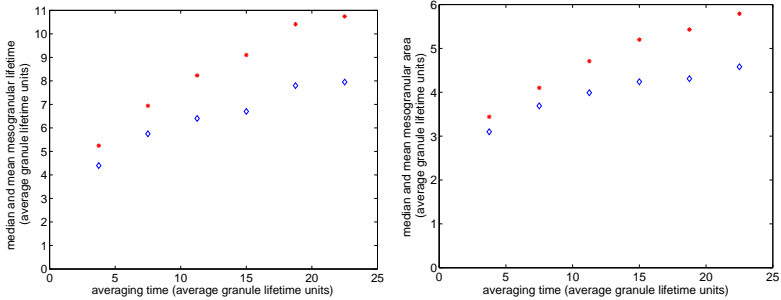

Figure A.37: Dependence of mesogranular median (diamonds) and mean (asterisks) lifetime (left) and size (right) on the threshold time. $RV/R - S$ ns model.

Bibliography

[1] Alves, S. G., Oliveira Neto, N. M., Martins, M. L., 2002, Electoral Surveys' Influence on the Voting Processes: A Cellular Automaton Model. *Physica A*, 316:601-614

[2] Berger, T. E., Löfdahl, M. G., Shine, R. A., Title, A. M., 1998, Measurements of Solar Magnetic Element Dispersal. *The Astrophysical Journal*, 506:439-449

[3] Berlekamp, E. R., Conway, J. H., Guy, R. K., 1982, *Winning Ways for Your Mathematical Plays*.

[4] Bogart, R. S., Gierasch, P. J., MacAuslan, J. M., 1980, Linear Modes of Convection in the Solar Envelope. *The Astrophysical Journal*, 236:285-293

[5] Bordogna, C. M., Albano, E. V., 2006, Phase Transitions in a Social Impact Model for Opinion Formation. *International Journal of Modern Physics*, 17:409-418

[6] Brandt, P. N., Ferguson, S., Scharmer, G. B., Shine, R. A., Tarbell, T. D., Title, A. M., Topka, K., 1991, Variations of Grnaulation Properties on a Mesogranular Scale. *Astronomy and Astrophysics*, 241:219-226

[7] Cattaneo, F., Dawn, L., Weiss, N., 2001, On the Origin of the Solar Mesogranulation. *The Astrophysical Journal*, 563:L91-L94

[8] Chandrasekhar, S., 1943, Stochastic Problems in Physics and Astronomy. *Reviews of Modern Physics*, 15:1-89

[9] Chou, D.-Y., Labonte, B. J., Braun, D. C., Duvall, T. L., Jr., 1991, Power Spectra of Solar Convection. *The Astrophysical Journal*, 372:314-320.

[10] Cloutman, L. D., 1979, The Supergranulation - Solar Rip Currents. *Astronomy and Astrophysics*, 74:L1-L3

[11] de Rosa, M. L., Toomre, J., 1998, Correlation Tracking of Mesogranules from SOI-MDI Doppler Images to Reveal Supergranular Flow Fields. *Structure and Dynamics of the Interior of the Sun and Sun-like Stars SOHO 6/GONG 98 Workshop Abstract*, p.738.

[12] Deubner, F.-L., 1971, Some Properties of Velocity Fields in the Solar Photosphere. III. Oscillatory and Supergranular Motions as a Function of Height. *Solar Physics*, 17:6-20

[13] Deubner, F.-L., 1989, Mesogranulation: a Convective Phenomenon. *Astronomy and Astrophysics*, 216:259-264

[14] de Wijn, R. J., Rutten, R. J., Haverkamp E. M. W. P., Sütterlin, P., 2005, DOT Tomography of the Solar Atmosphere. IV. Magnetic Patches in Internetwork Areas. *Astronomy and Astrophysics*, 441:1183-1190

[15] Domínguez Cardeña, I., 2003, Evidence of Mesogranulation from Magnetograms of the Sun. *Astronomy and Astrophysics*, 412:L65-L68

[16] Duvall, T. L., Jr., 1980, The Equatorial Rotation Rate of the Supergranules. *Solar Physics*, 66:213-221

[17] Foukal, P., 1977, Supergranulation and the Dynamics of Gas and Magnetic Field Below the Solar Photosphere. *The Astrophysical Journal*, 218:539-546

[18] Frazier, E. N., 1970, Multi-Channel Magnetograph Observations. II. Supergranulation. *Solar Physics*, 14:89-111

[19] Furtado, L. S., Copelli, M., 2006, Response of Electrically Coupled Spiking Neurons: A Cellular Automaton Approach. *Physical Review E*, 73

[20] Gardner, M., 1970, Mathematica Games: The Fantastic Combinations of John Conway's New Solitaire Game "Life". *Scientific American*, 223:120-123

[21] Georgobiani, D., Zhao, J., Kosovichev, A. G., Benson, D., Stein, R. F., Nordlund, Å., 2007, Local Helioseismology and Correlation Tracking Analysis of Surface Structures in Realistic Simulations of Solar Convection. *The Astrophysical Journal*, 657:1157-1161

[22] Gierasch, P. J., 1985, On the Energetics of the Solar Supergranulation. *The Astrophysical Journal*, 288:795-800

[23] Ginet, G. P., Simon, G. W., 1992, On the Evidence for Mesogranulation in Solar Power Spectra. *The Astrophysical Journal*, 386:359-363

[24] Gizon, L., Duvall, T. L., Schou, J., 2003, Wave-like Properties of Solar Supergranulation. *Nature*, 421:43-44

[25] Greenberg, J. M., Hassard, B. D., Hastings, S. P., 1978, Pattern Formation and Periodic Structures in Systems Modelled by Reaction-Diffusion Equations. *Bulletin of the American Mathematical Society*, 84:1296

[26] Hart, A. B., 1956, Motions in the Sun at the Photospheric Level. VI. Large-scale Motions in the Equatorial Region. *Monthly Notices of the Royal Astronomical Society*, 116:38-55

[27] Harvey, J. A., Kolb, E. W., Reiss, D. B., Wolfram, S., 1982, Calculation of Cosmological Baryon Asymmetry in Grand Unified Gauge Models. *Nuclear Physics*, 201:16-100

[28] Hathaway, D. H., Beck, J. G., Han, S., Raymond, J., 2002, Radial Flows in Super-granules, *Solar Physics*, 205:25-38

[29] Hirzberger, J.,Vázquez, M.,Bonet, J. A., Hanslmeier, A., Sobotka, M., 1997, Time Series of Solar Granulation Images. I. Differences Between Small and Large Granules in Quiet Regions. *The Astrophysical Journal*, 480:406-419

[30] Hirzberger, M.,Bonet, J. A., Hanslmeier, J.,Vázquez, A., Sobotka, M., 1996, Time Evolution of Solar Granulation Phenomena. *Astronomische Gesellschaft Abstract Series*, 12:160

[31] Hirzberger, J.,Bonet, J. A.,Vázquez, M., Hanslmeier, A., 1999, Time Series of Solar Granulation Images. II. Evolution of Individual Granules. *The Astrophysical Journal*, 515:441-454

[32] Hirzberger, J.,Bonet, J. A.,Vázquez, M., Hanslmeier, A., 1999, Time Series of Solar Granulation Images. III. Dynamics of Exploding Granules and Related Phenomena. *The Astrophysical Journal*, 527:405-414

[33] Hurlburt, N., Toomre, J., 1982, The Lateral Deflection of Large-Scale Convective Flows by Scale Height Effects below the Solar Surface. *Bulletin of the American Astronomical Society*, 14:938

[34] Kitagawa, T., 1974, Cell Space Approaches in Biomathematics. *Mathematical Biosciences*, 19:27

[35] Khomenko, E. V., Collados, M., Solanki, S. K., Lagg, A., Trujillo Bueno, J., 2003, Quiet-Sun Inter-Network Magnetic Fields Observed in the Infrared. *Astronomy and Astrophysics*, 408:1115-1135

[36] Lawrence, J. K., Cadavid, A. C., Ruzmaikin, A., 2001, Mesogranulation and Turbulence in Photospheric Flows. *Solar Physics*, 202:27-39

[37] Leighton, R. B., Noyes, R. W., Simon, G. W., 1962, Velocity Fields in the Solar Atmosphere. I. Preliminary Report. *The Astrophysical Journal*, 135:474-493

[38] Leitzinger, M., Brandt, P. N., Hanslmeier, A., Pötzi, W., Hirzberger, J., 2005, Dynamics of Solar Mesogranulation. *Astronomy and Astrophysics*, 444:245-255

[39] Lin, H., Rimmele, T., 1999, The Granular Magnetic Fields on the Quiet Sun. *The Astrophysical Journal*, 514:448-455

[40] Lindenmayer, A., 1968, Mathematical Models for Cellular Interactions in Development. *Journal of Theoretical Biology*, 18:280

[41] Lindzen, R. S., Tung, K. K., 1978, Wave Overreflection and Shear Instability. *Journal of the Atmospheric Sciences*, 35:1626-1632

[42] Martin, O., Odlyzko, A., Wolfram, S., 1984, Algebraic Properties of Cellular Automata. *Communications in Mathematical Physics*, 93:219-258

[44] Muller, R., Auffret, H., Roudier, T., Vigneau, J., Simon, G. W., Frank, Z., Shine, R. A., Title, A. M., 1992, Evolution and Advection of Solar Mesogranulation. *Nature*, 356:322-325

[44] Müller, D. A. N., Steiner, O., Schlichenmaier, R., Brandt, P. N., 2001, Time-slice Diagrams of Solar Granulation, *Solar Physics*, 203:211-232

[45] November, L. J., Toomre, J., Gebbie, K. B., Simon, G. W., 1981, The Detection of Mesogranulation on the Sun. *The Astrophysical Journal*, 245:L123-L126

[46] November, L. J., Simon, G. W., 1988, Precise Proper-Motion Measurement of Solar Granulation. *The Astrophysical Journal*, 333:427-442

[47] Oda, N., 1984, Morphological Study of the Solar Granulation. III - The Mesogranulation. *Solar Physics*, 93:243-255

[48] Packard, N., Wolfram, S., 1985, Two-Dimensional Cellular Automata. *Journal of Statistical Physics*, 38:901

[49] Ploner, S. R. O., Solanki, S. K., Gadun, A. S., 2000, Is Solar Mesogranulation a Surface Phenomenon?. *Astronomy and Astrophysics*, 356:1050-1054

[50] Ploner, S. R. O., 1998, *Dynamics of the Solar Convection Zone and Atmosphere*, PhD Thesis.

[51] Rast, M. P., 2003, The Scales of Granulation, Mesogranulation, and Supergranulation. *The Astrophysical Journal*, 597:1200-1210

[52] Rast, M. P., 1991, High Wavenumber Thermal Convection Enhanced in Regions of Partial Ionization. *Challenges to Theories of the Structure of Moderate-Mass Stars, Conference Proceedings*, 388:179

[53] Rast, M. P., Toomre, J., 1993, Compressible Convection WithIonization. I. Stability, Flow Assymetries, and Energy Transport. *The Astrophysical Journal*, 419:224-239

[54] Rast, M. P., Toomre, J., 1993, Compressible Convection WithIonization. II. Thermal Boundary-Layer Instability. *The Astrophysical Journal*, 419:240-254

[55] Rieutord, M., Roudier, T., Malherbe, J. M., Rincon, F., 2000, On Mesogranulation, Network Formation and Supergranulation. *Astronomy and Astrophysics*, 357:1063-1072

[56] Rosen, R., 1981, Pattern Generation in Networks. *Progress of Theoretical Biology*, 6:161

[57] Rösch, J., 1960, Observations from the Pic du Midi. *Aerodynamic Phenomena in Stellar Atmospheres, Proceedings of the International Astronomical Union Symposium no. 12 on Cosmical Gas Dynamics*, 313-319

[58] Roudier, Th., Lignières, F., Rieutord, M., Brandt, P. N., Malherbe, J. M., 2003, Families of Fragmenting Granules and Their Relation to Meso- and Supergranular Flow Fields. *Astronomy & Astrophysics*, 409:299-308

[59] Roudier, Th., Muller, R., 2004, Relation Between Families of Granules, Mesogranules, and Photoshperic Network. *Astronomy & Astrophysics*, 419:757-762

[60] Selvam, A. M., A Cell Dynamical System Model for Thundercloud Electrification. *Proceedings of the International Conference on Lightning and Static Electricity*.

[61] Simon, G. W., Weiss, N. O., 1968, Supergranules and the Hydrogen Convection Zone. *Zeitschrift für Astrophysik*, 69:435-450

[62] Simon, G. W., Leighton, R. B., 1964, Velocity Fields in the Solar Atmosphere. III. Large-Scale Motions, the Chromospheric Network, and Magnetic Fields. *The Astrophysical Journal*, 140:1120

[63] Simon, G. W., Title, A. M., Weiss, N. O., 1991, Modeling Mesogranules and Exploders on the Solar Surface. *The Astrophysical Journal*, 375:775-788

[64] Skumanich, A., Smythe, C., Frazier, E. N., 1975, On the Statistical Description of Inhomogeneities in the Quiet Solar Atmosphere. I - Linear Regression Analysis and Absolute Calibration of Multichannel Observations of the Ca/+/ Emission Network. *The Astrophysical Journal*, 200:747-764

[65] Snodgrass, H. B., Ulrich, R. K. , 1990, Rotation of Doppler Features in the Solar Photosphere. *The Astrophysical Journal*, 351:309-316

[66] Spruit, H. C., Nordlund, Å., Title, A. M., 1990, Solar convection. *Annual review of astronomy and astrophysics*, 28:263-301

[67] Stein , R. F., Nordlund, Å., 1998, Simulations of solar granulation. I. General properties. *The Astrophysical Journal*, 499:914-933

[69] Stein, R. F., Benson, D., Georgobiani, D., Nordlund, Å., 2006, Supergranule Scale Convection Simulations. *Proceedings of SOHO 18/GONG 2006/HELAS I, Beyond the Spherical Sun*, 624:79.S

[69] Stein,R. F., Bercik, D. J., Brandenburg, A., Georgobiani, D., Nordlund, Å., 1998, Solar Magneto-Convection. *Bulletin of the American Astronomical Society*, 29:1326

[70] Steiner, O., 2003, Large-Scale Flow in Two-Dimensional Simulation of Solar Convection. *Modelling of Stellar Atmospheres, Proceedings of the 210th Symposium of the International Astronomical Union*, C11

[71] Stevens, P. S., 1974, *Patterns in Nature*.

[72] Straus, T., Deubner, F.-L., Fleck, B., 1992, Is Mesogranulation a Distinct Regime of Convection?. *Astronomy and Astrophysics*, 256:652-659

[73] Straus, T., Bonaccini, D., 1997, Dynamics of the Solar Photosphere. I. Two-Dimensional Spectroscopy of Mesoscale Phenomena. *Astronomy and Astrophysics*, 324:704-712

[74] Title, A. M., Tarbell, T. D., Topka, K. P., Ferguson, S. H., Shine, R. A., 1989, Statistical Properties of Solar Granulation Derived From the Soup Instrument on Spacelab 2. *The Astrophysical Journal*, 336:475-494

[75] Thompson, D'A. W., 1961, *On Growth and Form*.

[76] Ulam, S., 1952, Random Processes and Transformations. *Proceedings of the International Congress on Mathematics*, 2:264-275

[77] Ulam, S., 1972, Some Ideas and Prospects in Biomathematics. *Annual Review of Biophysics and Bioengineering*, 1:277-292

[78] Vickers, G. T., 1971, On the Formation of Giant Cells and Supergranules. *The Astrophysical Journal*, 163:363-374

[79] Vögler, A., Shelyag, S., Schüssler, M., Cattaneo, F., Emonet, T., Linde,T., 2005, Simulations of Magneto-Convection in the Solar Photosphere. Equations, Methods, and Results of the MURaM code. *Astronomy and Astrophysics*, 429:335-351

[80] Vögler, A., 2003, Three-Dimensional Simulations of Magneto-Convection in the Solar Photosphere. *PhD Thesis*.

[81] von Neumann, J., 1963, The General and Logical Theory of Automata. *Collected works*, 5:288

[82] von Neumann, J., 1966, *Theory of Self-Reproducing Automata*.

[83] Wang, H., 1989, Do Mesograules Exist?. *Solar Physics*, 123:21-32

[84] Welsch, B. T., Fisher, G. H., Abbett, W. P., 2004, ILCT: Recovering Photospheric Velocities from Magnetograms by Combining the Induction Equation with Local Correlation Tracking. *The Astrophysical Journal*, 610:1148-1156

[85] Wolfram, S., 1983, Statistical Mechanics of Celullar Automata. *Reviews of Modern Physics*, 55:601

[86] Wolfram, S., 1984, Cellular Automata as Models for Complexity. *Nature*, 311:419

[87] Wolfram, S., 1984, Universality and Complexity in Cellular Automata. *Physica*, 10D:1

[88] Wolfram, S., 1984, Computation Theory of Cellular Automata. *Communications in Mathematical Physics*, 96:15

[89] Wolff, C., 1995, Oscillation-convection Coupling: Cause of Supergranulation. *The Astrophysical Journal*, 443:423-433

[90] Quan-Xing, L., Zhen, J., Mao-Xing, L., 2006, Spatial Organization and Evolution Period of the Epidemic Model Using Cellular Automata. *Physical Review E*, 74

Publications

Contributed papers in conference proceedings

Matloch, R. Cameron, D. Schmitt, M Schüssler, "Solar mesogranulation as a cellular automaton effect", Modern Solar Facilities - Advanced Solar Science Workshop, Universitätsverlag Göttingen 2007, p. 339-342

Acknowledgements

Lebenslauf

Name: Łukasz Maciej Matloch

Geburt: 09.05.1976 in Olsztyn, Polen

Eltern: Marian Matloch
Alicja Matloch

Staatsbürgerschaft: Polnisch

Schulbildung: 1983-1991 Grundschule

1991-1995 Gymnasium

Studium: 1995-1998 Physikstudium an der Physikalisches Fakultät
der Warschau Universität, Polen

1998-2000 Laserphysik, Free University of
Amsterdam, Holland

2000-2003 Atmosphärenphysik,
Geophysische Fakultät
der Warschau Universität, Polen

2004-2008 Doktorarbeit
Während dieser Zeit Tätigkeit als
wissenschaftlicher Mitarbaiter am
Max-Planck-Institut für Sonnesysytemforschung
in Katlenburg-Lindau